Phil. Trans. R. Soc. Lond. A **319**, 219–247 (1986) [219]
Printed in Great Britain

A MICROSTRUCTURAL STUDY OF THE OXIDATION OF Fe–Ni–Cr ALLOYS
II. 'NON-PROTECTIVE' OXIDE GROWTH

BY W. M. STOBBS[1], S. B. NEWCOMB[1] AND E. METCALFE[2]

[1] *Department of Metallurgy and Materials Science, University of Cambridge, Pembroke Street, Cambridge CB2 3QZ, U.K.*

[2] *Central Electricity Research Laboratories, Technology Planning and Research Division, Central Electricity Generating Board, Kelvin Avenue, Leatherhead, Surrey KT22 7SE, U.K.*

(*Communicated by R. W. K. Honeycombe, F.R.S. – Received 5 February* 1985)

[Plates 1–24]

CONTENTS

The scaling characteristics of a range of laboratory prepared Fe–10Cr–Ni alloys and a commercial Fe–9Cr–1Mo steel when oxidized in air and in 1 %† CO–CO_2 at 600 °C for periods up to 1500 h are described. The results are compared with similar data obtained for the Fe–20Cr–Ni alloys discussed previously in I. The microstructure and microchemistry of the 'non-protective' scales formed on the 'low' chromium alloys were investigated by 'edge-on' transmission electron microscopy although data obtained by standard investigative techniques are also given.

The simultaneous outward *and* inward growth of chemically and structurally different oxides was shown to occur in both oxidation environments but in a number of different ways and occasionally with both lateral and temporal instability. For example, in air, an inward growing fine grained spinel was found to be important in determining the oxidation behaviour in more than one manner: it could migrate bodily inward by ion exchange allowing further epitaxial oxidation above it, or alternatively it could inhibit further inward oxidation beneath it apparently increasingly as its chromium content rose. Evidence is also presented for the different ways in which either inward oxidation or carburization can occur in CO–CO_2, this apparently requiring CO_2 to pass through pore-free outward and inward growing scales.

1. Introduction

In this paper we describe the scaling behaviour of a range of Fe–10Cr–Ni alloys as well as Fe–9Cr–1Mo as oxidized at 600 °C in both air and in 1 % CO–CO_2. Under these conditions these alloys characteristically form 'non-protective' scales on the phenomenological basis for the term as given in paper I (Newcomb *et al.* 1986). There we defined such oxidation behaviour as exhibiting not only *outward* growth of a scale relative to the original metal surface, but also the formation of oxides beneath this involving the diffusion of anions *inwards* through the scale and subscale alloy. At first sight it is difficult to differentiate morphologically between situations in which the inward development of a scale occurs by cationic exchange from those in which inward anion movement dominates the reaction. We will in fact find that there *are* situations in which such a differentiation can be made, but cationic exchange can itself play an important role in 'non-protective' oxidation as we define it. Here it is demonstrated that inward growing oxides can form with an epitaxial relation with the local alloy structure (whether transformed or not). We define this type of inward grown scale as 'orientated inward' oxide (OI). Equally, inward oxidation can of course proceed with no clearly developed orientation relationship between the oxide and the metal matrix and in this case the oxide is described as 'random inward' (RI).

Just as in paper I where we described the 'protective' oxidation behaviour of a related range of Fe–20Cr–Ni alloys, we follow an essentially phenomenological approach to the description of the scales. This is firstly because many of the results we describe on the form of the scales produced cannot be understood on the basis of currently established models for the oxidation of such alloys (given that oxidation models have largely been developed on the basis of low resolution microprobe and SEM data) and secondly because such a classification is both well suited to the high resolution microstructural information obtained and facilitates the characterization of potentially model sensitive observations. The main technique we have used is the transmission electron microscopy (TEM) of 'edge-on' oxidized samples, allowing the microstructural and microchemical description in a single foil of an essentially historical section through the scale and subscale alloy. The results obtained in this manner are described for the

† Unless otherwise indicated all percentage compositions are by mass.

air oxidized alloys in §3(*a*), and for oxidation in the 1% CO–CO_2 atmosphere in §3(*b*). Information obtained by more conventional techniques such as gravimetry, X-ray diffractometry and optical and scanning electron microscopy (SEM) is given in §2. All the techniques used, as well as the specimen pre-oxidation treatments employed, are detailed in paper I.

The alloys chosen for examination have some relevance industrially and allow a simple comparison to be made of the relative effect of Cr and Ni as well as that of the alloy structure, as discussed in paper I. All the alloys are shown superposed on a Schaeffler diagram in figure 1 of paper I, and chemical composition data for the specific alloys described in this paper are given in table 1. Their microstructures, after a pre-oxidation heat treatment, may be compared by examination of figure 1, plate 1, and table 2. It should be noted that both the industrial 9Cr–1Mo alloy and the 10Cr–10Ni alloy are ferritic while the higher nickel content materials are austenitic.

TABLE 1. CHEMICAL COMPOSITIONS OF THE ALLOYS (PERCENTAGES BY MASS)

alloy	Fe	Cr	Ni	Mo	Mn	Si	C	S	P
Fe–9Cr–1Mo(α)	balance	9.00	—	0.95	0.46	0.40	0.11	0.015	0.01
Fe–10Cr–10Ni(α)	balance	10.00	10.37	—	—	—	0.002	—	—
Fe–10Cr–20Ni(γ)	balance	10.24	19.70	—	—	—	0.003	—	—
Fe–10Cr–34Ni(γ)	balance	9.90	33.90	—	—	—	0.002	—	—

TABLE 2. SUMMARY OF THE MICROSTRUCTURAL DATA FOR THE Fe–9Cr AND Fe–10Cr–Ni ALLOYS BEFORE OXIDATION

(These data are included to allow a comparison with the changes of subscale that can occur for the ferritic alloys as a function of the oxidation treatment (see tables 5 and 6).)

	structure		lattice parameter/nm	
alloy	TEM	XRD	±0.001	grain size/μm
Fe–9Cr–1Mo	α	α	0.288	5
Fe–10Cr–10Ni	α	α	0.288	5
Fe–10Cr–20Ni	γ	γ	0.358	20
Fe–10Cr–34Ni	γ	γ	0.359	15

2. RESULTS OBTAINED BY CONVENTIONAL TECHNIQUES

In this section we give the data, for the alloys examined, as obtained by gravimetry (§2*a*), X-ray diffractometry (§2*b*), SEM of the upper scale surface (§2*c*) and optical microscopy of cross sections through the scale and subscale alloy (§2*d*). Results, from the use of these techniques, were obtained after 60, 125, 500, 1000 and in some cases 1500 h exposure to each of the oxidizing atmospheres with the intention both of characterizing the general temporal development of the scaling behaviour and of ensuring that any historical inferences made from the microstructural examination of the TEM 'edge-on' specimens could be justified.

(*a*) *Oxidation kinetics*

The mass gain data are shown graphically on logarithmic plots for exposure to air and to 1% CO–CO_2 in figure 2*a* and *b* respectively, while the rate constants, $k_n/(\mathrm{g\ cm^{-2}})^n\ \mathrm{s^{-1}}$, for the observed power laws, (n), as well as mass gain results for 1000 h oxidation are given in table 3. In air the 10Cr–20Ni and 10Cr–34Ni alloys follow approximately parabolic kinetics but Fe–10Cr–10Ni has $n = 0.75$ so that although mass gains for this material at 60 h were well

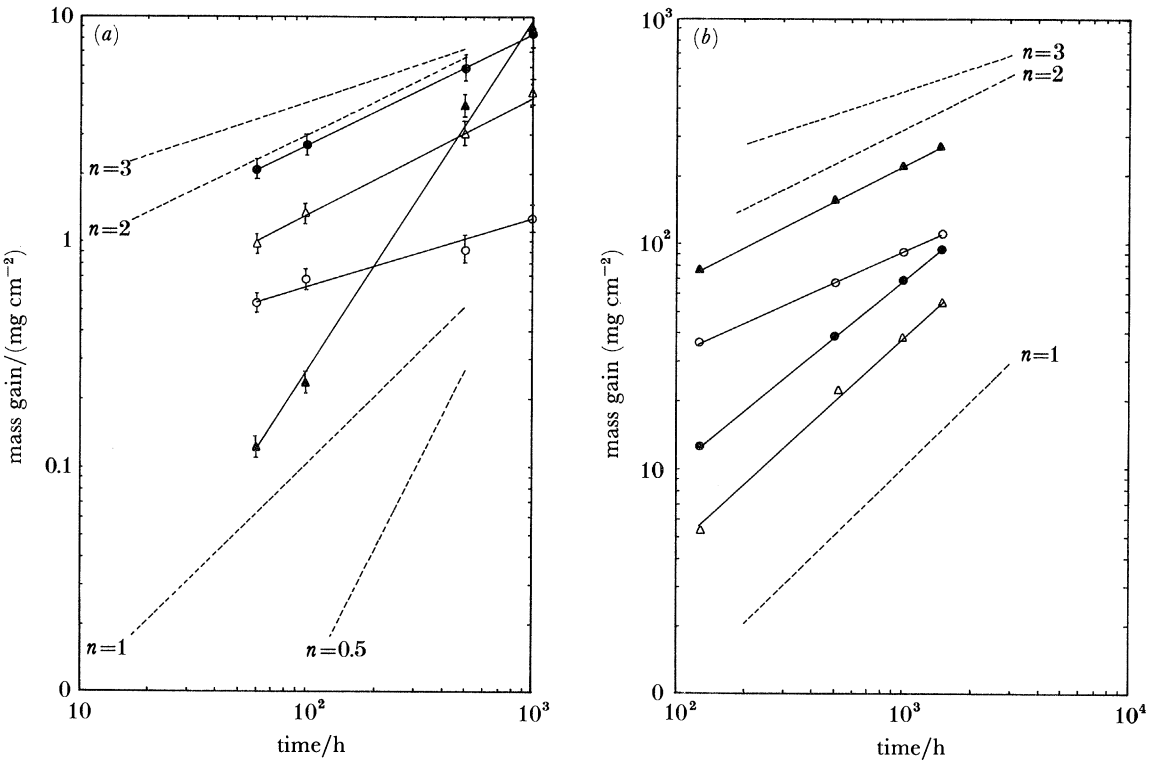

FIGURE 2. The temporal mass gain behaviour of the Fe–9Cr and Fe–10Cr–10Ni alloys as oxidized at 600 °C in: (*a*) air and (*b*) 1% CO–CO_2.
○, Fe–9Cr–1Mo; ▲, Fe–10Cr–10Ni; ●, Fe–10Cr–20Ni; △, Fe–10Cr–34Ni.

TABLE 3. MASS GAINS AND OXIDATION RATE CONSTANTS FOR THE Fe–Ni–Cr ALLOYS OXIDIZED IN AIR AND IN 1% CO–CO_2 AT 600 °C

alloy	mass gain in 125 h/(mg cm^{-2})	mass gain in 1000 h/(mg cm^{-2})	n	k_p / g^2 cm^{-4} s^{-1}	k_n / (g cm^{-2})^n s^{-1}
		(*a*) 1% CO–CO_2			
Fe–9Cr–1Mo	33.92	83.15	2.14	1.92×10^{-9}	1.36×10^{-9}
Fe–10Cr–10Ni	69.06	200.42	1.92	1.12×10^{-8}	1.27×10^{-8}
Fe–10Cr–20Ni	11.68	63.16	1.15	1.11×10^{-9}	1.16×10^{-8}
Fe–10Cr–34Ni	4.79	36.28	1.06	3.65×10^{-10}	8.26×10^{-9}
		(*b*) *air*			
Fe–9Cr–1Mo		1.25	3.25	4.34×10^{-13}	1.02×10^{-16}
Fe–10Cr–10Ni		9.50	0.75	2.51×10^{-11}	8.45×10^{-9}
Fe–10Cr–20Ni		7.65	2.00	1.63×10^{-11}	1.63×10^{-11}
Fe–10Cr–34Ni		4.90	1.92	6.67×10^{-12}	9.03×10^{-11}

below those of the higher nickel alloys, by 1000 h it exhibited the highest weight gain. In air the industrial alloy, Fe–9Cr–1Mo, showed both the least mass gains and an approximately cubic power law ($n = 3.25$), a behaviour similar to that exhibited by the 20Cr–Ni alloys, which form 'protective' scales in air, except that the rate constant in this instance is considerably larger than those generally obtained for the 'higher' chrome alloys (see paper I). (Note that the artificial k_p values shown in table 3 are retained for comparison with the data in table 3 of paper I.) All the mass gain data should be treated with caution, and in particular those for

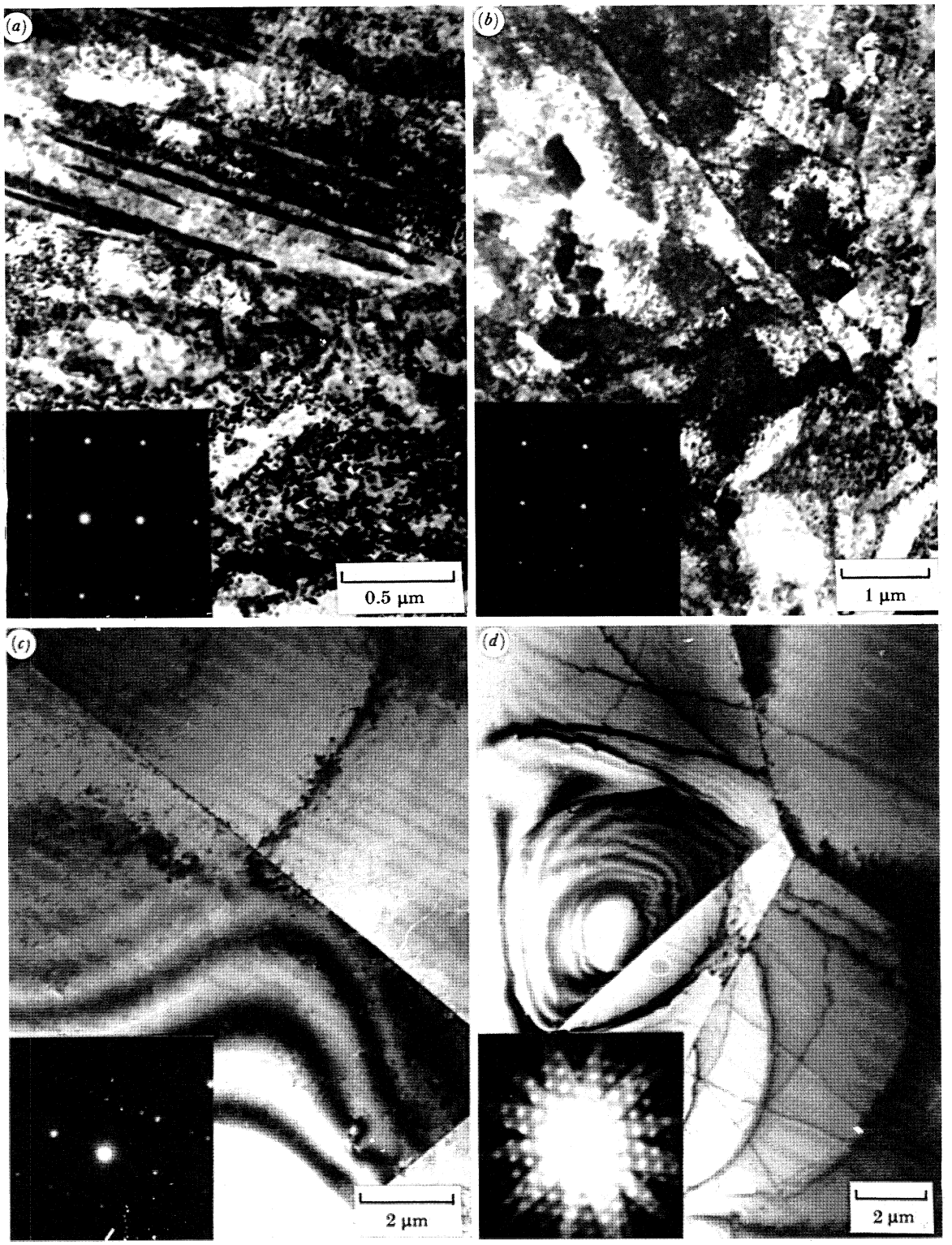

FIGURE 1. Microstructures of the alloys prior to oxidation. Bright field TEM. Diffraction patterns for each alloy are shown in the insets. (*a*) Fe–9Cr–1Mo: diffraction plane: $(011)_\alpha$; (*b*) Fe–10Cr–10Ni: diffraction plane: $(001)_\alpha$; (*c*) Fe–10Cr– 20Ni: diffraction plane: $(011)_\gamma$; (*d*) Fe–10Cr–34Ni: diffraction plane: $(011)_\gamma$.

(*Facing p.* 222)

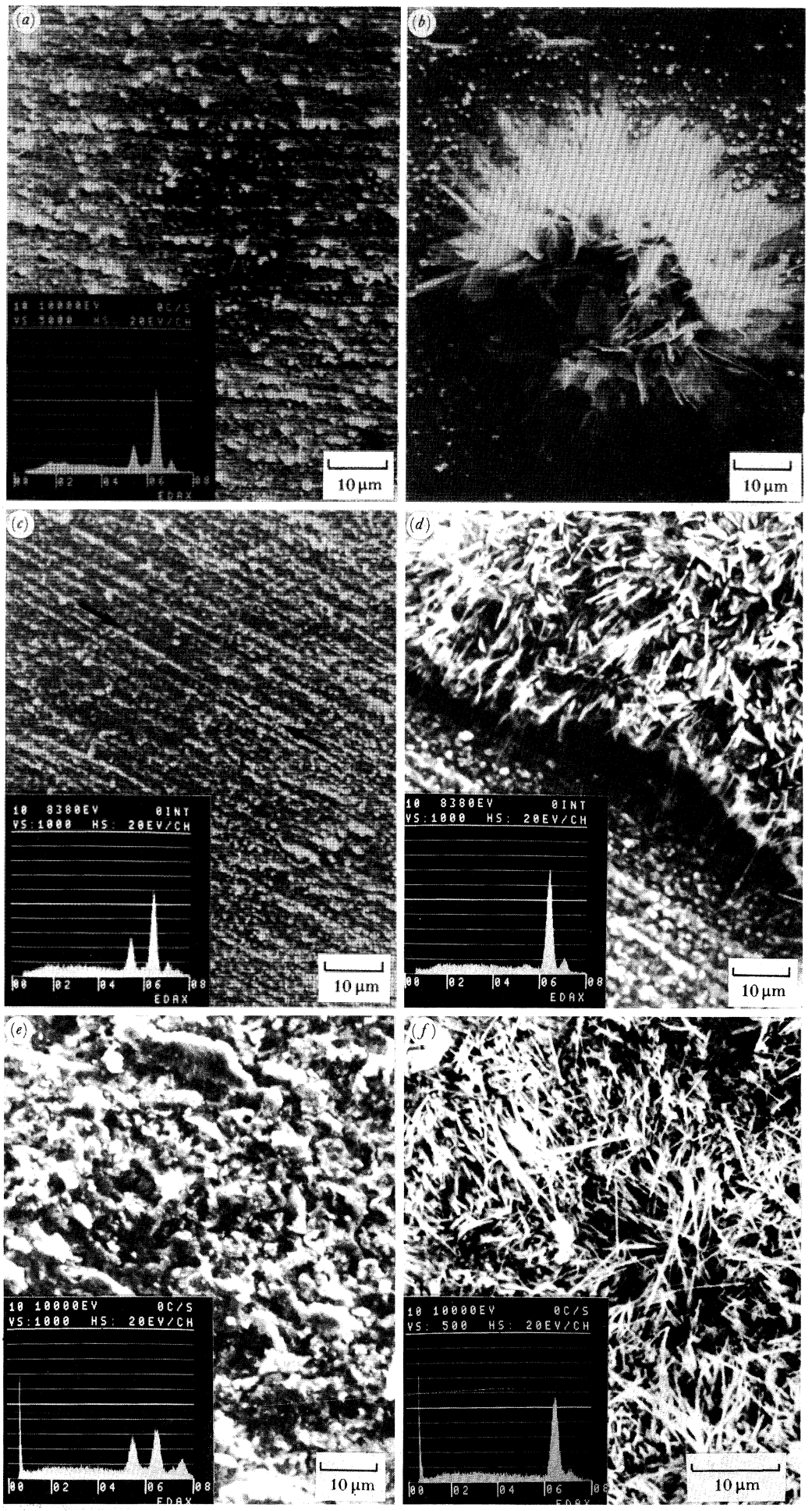
(a)
10 10000EV 0C/S
VS 5000 HS: 20EV/CH
EDAX
10 μm
(b)
10 μm
(c)
10 8380EV 0INT
VS:1000 HS: 20EV/CH
EDAX
10 μm
(d)
10 8380EV 0INT
VS:1000 HS: 20EV/CH
EDAX
10 μm
(e)
10 10000EV 0C/S
VS:1000 HS: 20EV/CH
EDAX
10 μm
(f)
10 10000EV 0C/S
VS: 500 HS: 20EV/CH
10 μm

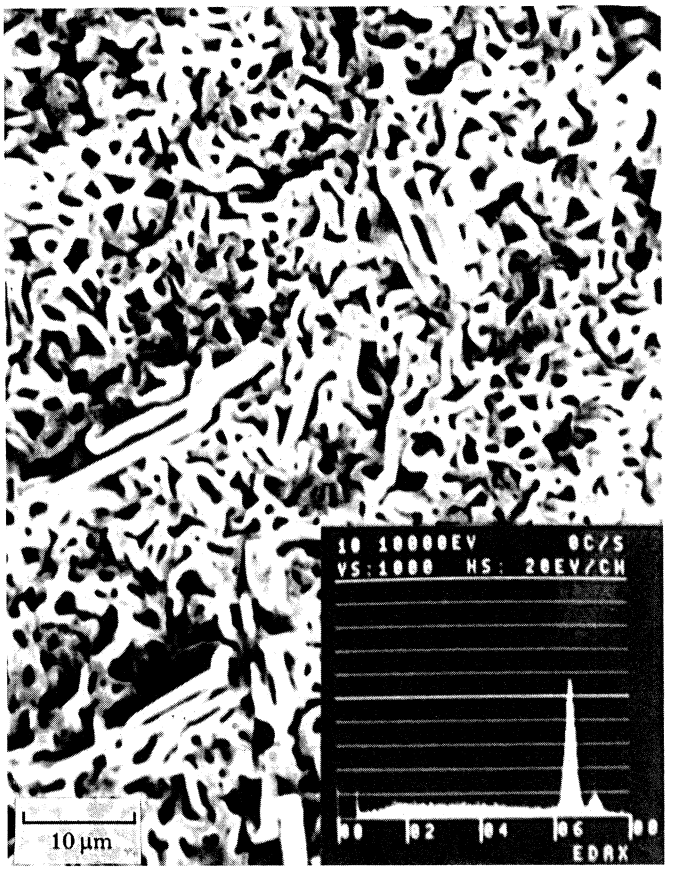

FIGURE 4. Scanning electron micrograph and 20 kV EDS analysis (Fe:6.398 keV) of the surface of the scale formed on Fe–10Cr–10Ni in 1 % CO–CO_2 after 1000 h at 600 °C.

DESCRIPTION OF PLATE 2

FIGURE 3. Scanning electron micrographs and 20 kV EDS analyses (Cr:5.411, Fe:6.398, Ni:7.41 keV) of the surfaces of the oxides formed in air after 1000 h oxidation at 600 °C. (*a*) Fe–9Cr–1Mo: 'protective' scale; (*b*) Fe–9Cr–1Mo: 'non-protective' nodule; (*c*) Fe–10Cr–10Ni: 'protective' scale; scratches on the surface of the alloy are arrowed; (*d*) Fe–10Cr–10Ni: 'non-protective' region adjacent to a 'protective' scale; (*e*) Fe–10Cr–20Ni: original M_3O_4–Fe_3O_4 interface, the upper oxides having spalled; (*f*) Fe–10Cr–34Ni: outermost haematite scale.

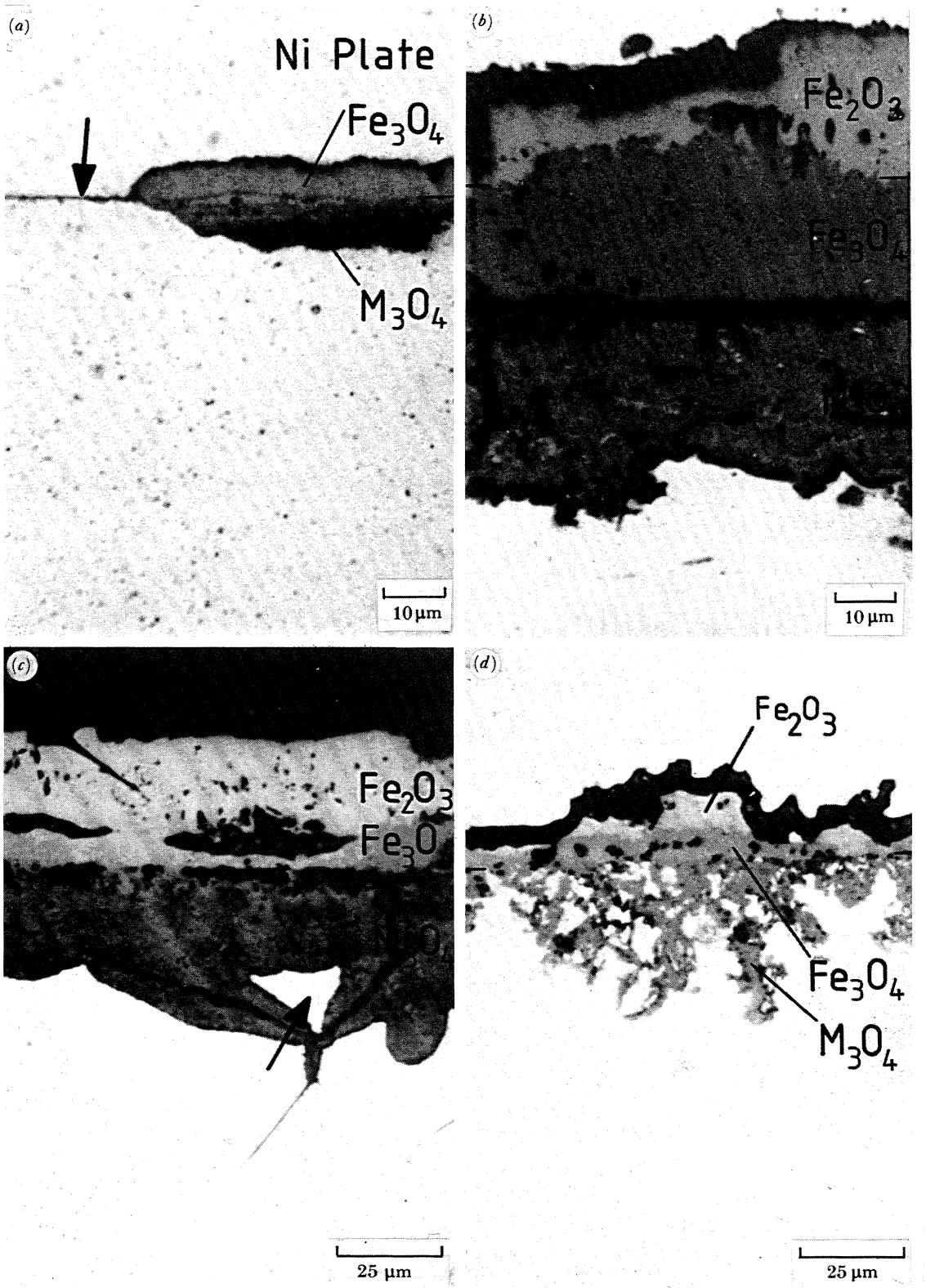

FIGURE 5. Optical micrographs of the scales formed on the Fe–9Cr and Fe–10Cr–Ni alloys after 1000 h oxidation in air at 600 °C. (*a*) Fe–9Cr–1Mo: a thin layer of 'protective' oxide, lying adjacent to a multilayered scale is arrowed; (*b*) Fe–10Cr–10Ni: note the separation of the scale at the Fe_3O_4–M_3O_4 interface; (*c*) Fe–10Cr–20Ni: unoxidized alloy situated in the inward grown M_3O_4 scale is arrowed; (*d*) Fe–10Cr–34Ni: note the inhomogeneity in the thicknesses of the scale.

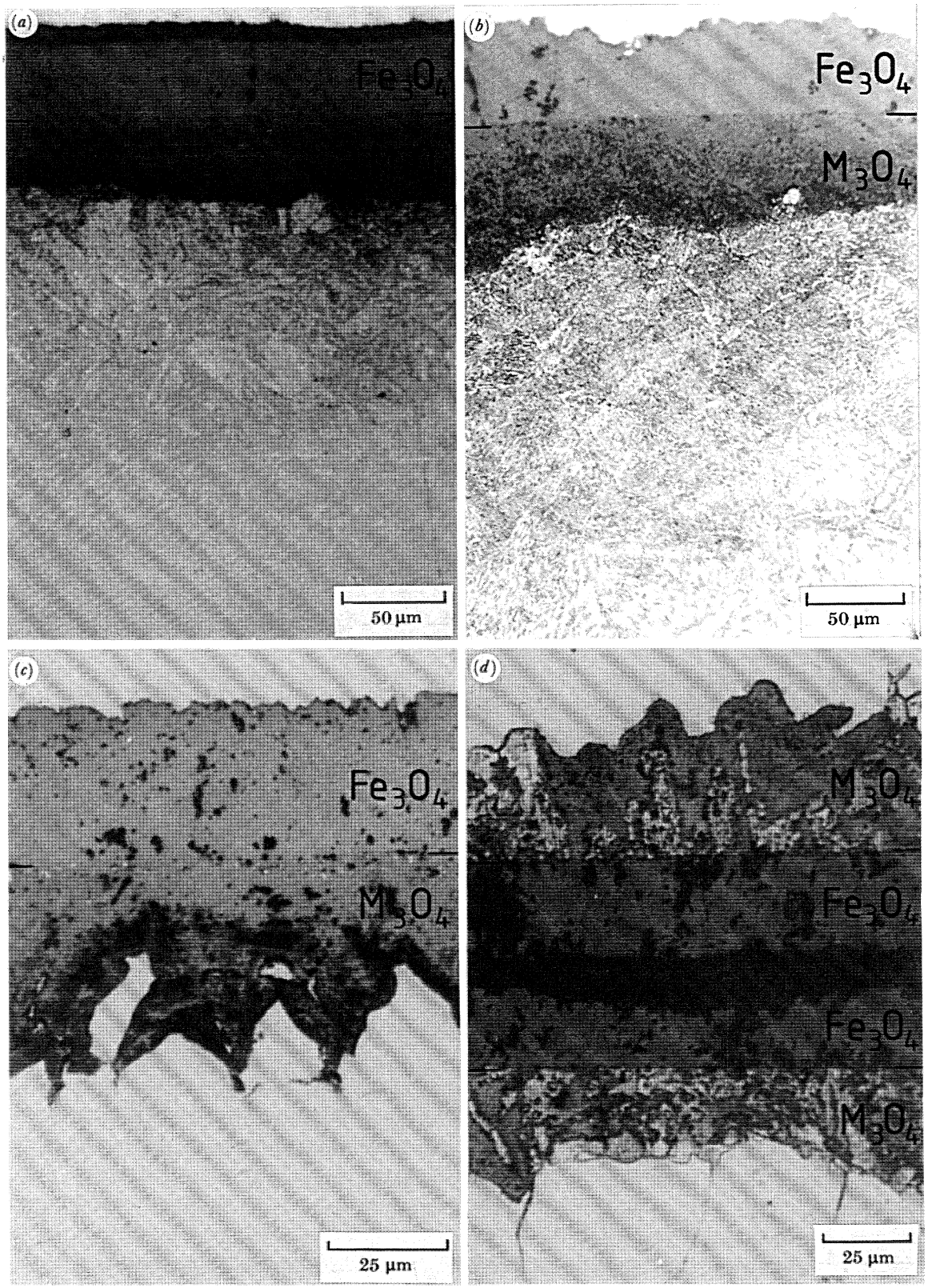

FIGURE 6. Optical micrographs of the scales formed on the Fe–9Cr and Fe–10Cr–Ni alloys after 1000 h oxidation in 1 % CO–CO_2 at 600 °C. (*a*) Fe–9Cr–1Mo; (*b*) Fe–10Cr–10Ni; (*c*) Fe–10Cr–20Ni; (*d*) Fe–10Cr–34Ni; (note that this is a micrograph of two scales lying face to face). It should be noted that carbide precipitation has occurred in both the 9Cr–1Mo and 10Cr–10Ni alloys to a depth of *ca.* 100–150 μm beneath the scales by comparison with the austenitic 10Cr–20Ni and 10Cr–34Ni alloys where precipitation is not observed.

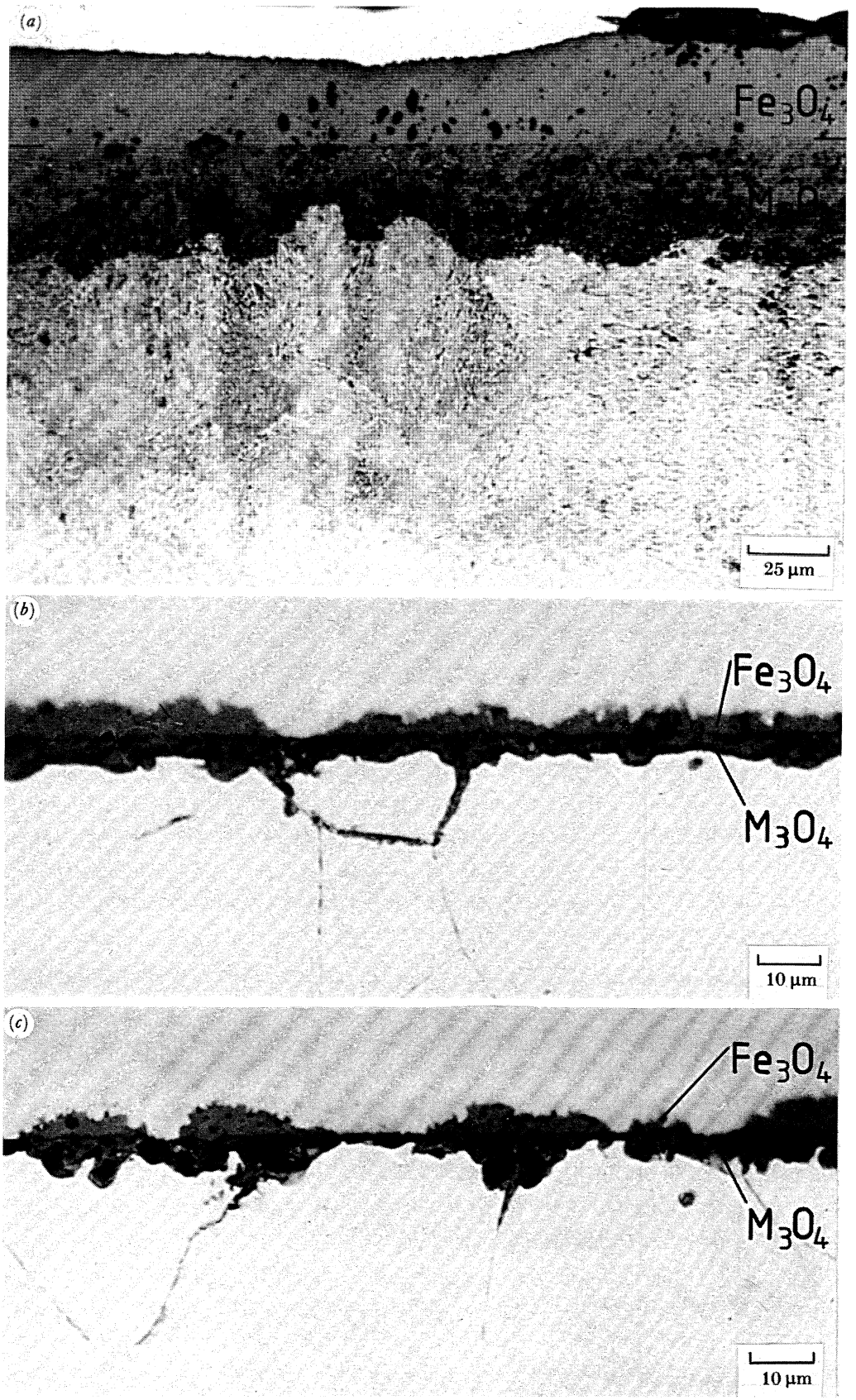

FIGURE 7. Optical micrographs of the scales formed on the Fe–10Cr–Ni alloys after 125 h oxidation in 1% CO–CO_2 at 600 °C. (*a*) Fe–10Cr–10Ni; (*b*) Fe–10Cr–20Ni; (*c*) Fe–10Cr–34Ni.

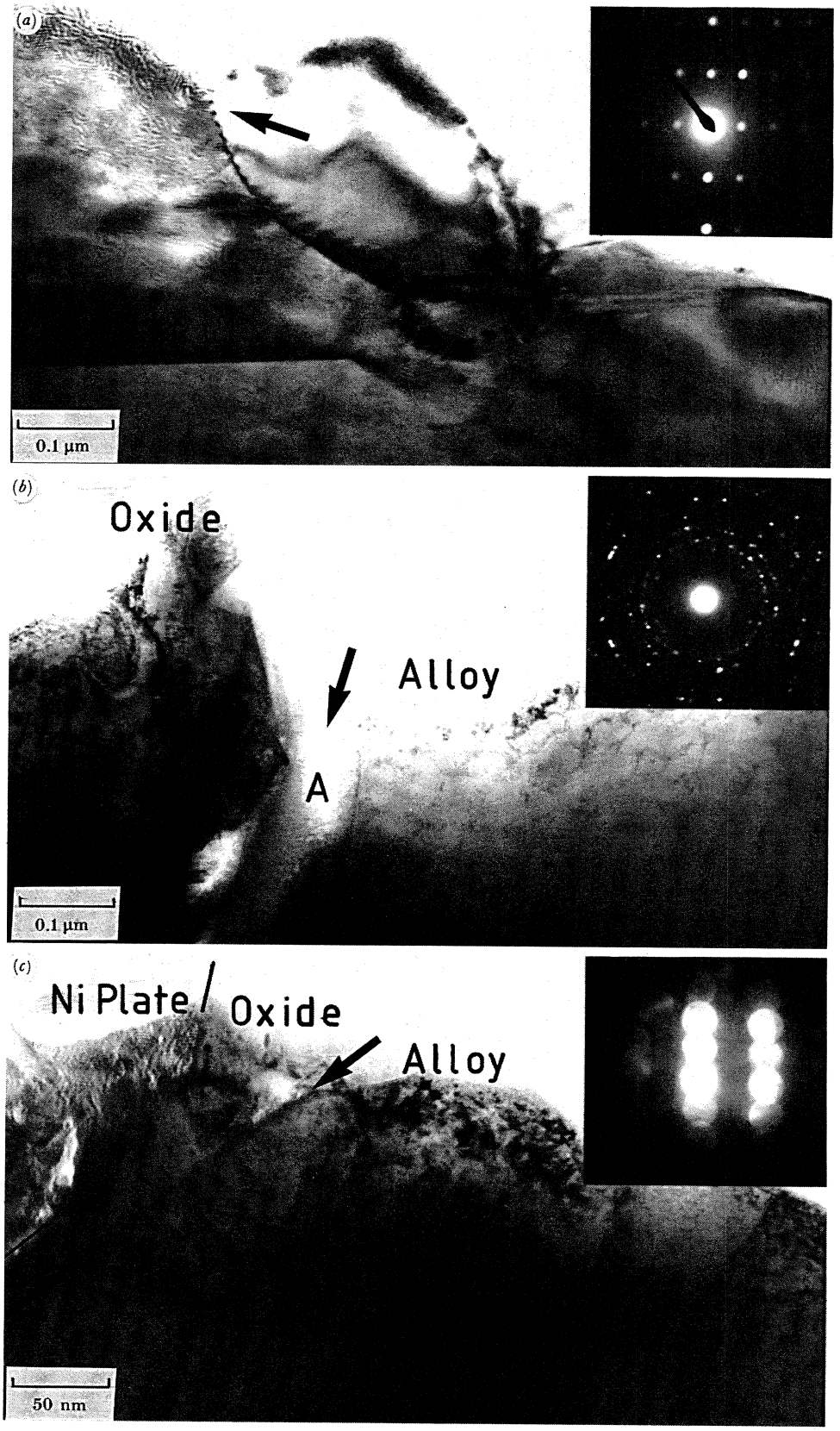

FIGURE 8. Bright field 'edge on' TEM micrographs showing the microstructures of the 'non-protective' and 'protective' scales formed on Fe–9Cr–1Mo in air at 600 °C after 1000 h. (*a*) Columnar grained and outward growing magnetite and inset $(112)_{Fe_3O_4}$ diffraction pattern. The arrow is normal to and approximately 1.5 μm from the Fe_3O_4–Fe_2O_3 interface. (*b*) The metal–oxide interface in the 'non-protective' scale, where the inward grown M_3O_4 is fine grained and non-equiaxed (see inset diffraction pattern). Partial separation of the two phases has occurred at the alloy–oxide interface, as at A, a region which has been infilled with sputter contamination. (*c*) Thin 'protective' M_2O_3 overlying ferrite. Note the flat alloy–oxide interface (arrowed). The inset diffraction pattern is a $(1211)_{M_2O_3}$ normal.

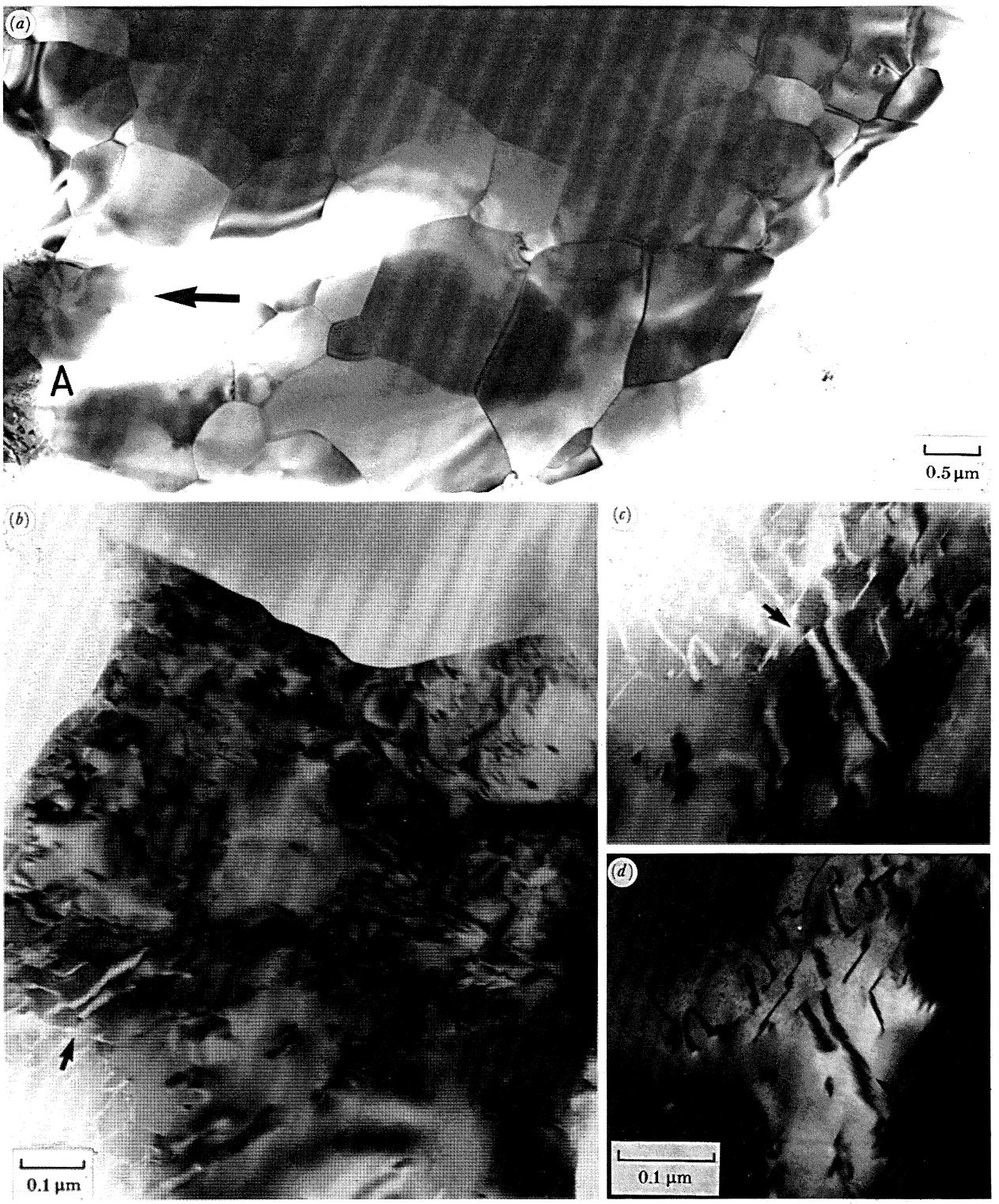

FIGURE 10. Microstructure of the magnetite formed on Fe–10Cr–10Ni in air after 1000 h at 600 °C showing the coarse grained morphology. (*a*) Approximately 10 μm from the original metal surface. The arrow gives the direction of the outer layer of haematite, bright-field. (*b*) A region from A in (*a*) approximately 5 μm from the Fe_3O_4–Fe_2O_3 interface, where defects may be observed, as arrowed, bright-field. (*c*) Bright-field and (*d*) dark-field images showing the defects in the magnetite at a higher magnification.

the 10Cr–10Ni alloy because of spalling. The 'higher than linear' kinetics exhibited by this alloy are thus associated with the fresh exposure of subscale regions of depleted chromium content (see §3*a*). Comparing the kinetics of the 20 and 34Ni alloys with those exhibited at a chromium content of 20% (paper I), we see that n has decreased from *ca.* 2.5 to closer to 2 while the relative mass gains have reversed, a behaviour exemplified by the 20Cr alloys of these nickel contents in CO–CO_2. This aspect of the kinetics is discussed in paper I in relation to the potential onset of chemical instabilities in the formation of 'protective' outward growing scales.

Considering the mass gain results for exposure to CO–CO_2 the n for all the alloys, except Fe–10Cr–10Ni, have decreased, both the 20 and 34Ni alloys exhibiting approximately linear kinetics while Fe–9Cr–1Mo now oxidizes roughly parabolically. Equally we see a common trend to smaller mass gains as the nickel content is increased, a characteristic of the 20Cr alloys (Newcomb *et al.* 1986) which also showed the general tendency to both smaller n and markedly larger mass gains in CO–CO_2 than in air. The 10Cr–10Ni alloy did not spall in CO–CO_2 so it is apparent that its behaviour in air is more characteristic of 'breakaway' (Holmes *et al.* 1974) than of 'non-protective' behaviour as defined here. We will examine further corroborative evidence for this distinction in the microstructural observations in §3.

The near cube law kinetics for the 9Cr–1Mo alloy, as well as its variable ranking with the 10Cr–Ni alloys as a function of oxidizing atmosphere, are particularly interesting given that X-ray diffractometry indicated that α-M_2O_3 is formed in air and this, as we saw in paper I, is an essentially 'protective' oxide. The characteristic observation on this material of duplex scales in 'edge-on' TEM samples must therefore be correlated carefully with the more coarse scale data obtained by optical microscopy of sections of the alloy which indicate that in different regions either 'protective' or 'non-protective' scales can form.

(*b*) *X-ray diffractometry data*

Whereas the temporal development of different chemical species in 'protective' scales can be followed relatively easily by diffractometry when 'non-protective' scales form, as on the alloys investigated here, useful information is only obtained when the general geometry of the processes involved is understood by the optical examination of sections. Thus although the raw X-ray data obtained is tabulated elsewhere (Newcomb 1983) only the results obtained after 1000 h oxidation in air are summarized in table 4.

TABLE 4. LATTICE PARAMETERS OF THE Fe–9Cr AND Fe–10Cr–Ni ALLOYS AND SCALES FORMED IN AIR AFTER 1000 h OXIDATION AT 600 °C

(More complete data including results obtained as a function of time have been presented previously (Newcomb 1983).)

	lattice parameter/nm				
	α	γ	M_3O_4	α–M_2O_3	
alloy	$a_0(\pm 0.001)$	$a_0(\pm 0.001)$	$a_0(\pm 0.001)$	a_H[a](± 0.01)	c_H[a](± 0.02)
Fe–9Cr–1Mo	0.286	—	0.838	0.50	1.32
Fe–10Cr–10Ni	0.286	0.357	—	0.50	1.36
Fe–10Cr–20Ni	0.287	0.356	0.825 ± 0.005	ND	ND
Fe–10Cr–34Ni	—	0.357	0.825	0.50	1.35

[a] Indexing based on equivalent hexagonal unit cell.
ND, no determination.

Considering the data for the alloys oxidized in air, it was found, for example, that the majority of the scale formed on Fe–9Cr–1Mo was α-M_2O_3 while M_3O_4 was only identified after 500 h. This was not, however, indicative of a temporal general change in behaviour but rather of localized chemical instability as was more clearly identified in the examination of sections of the oxidized material. Furthermore, the lattice parameters for the α-M_2O_3 seen after 1000 h are characteristic of a fairly high chromium content and more suggestive of a 'protective' scale than of the nearly pure haematite which is normally the upper oxidation product on an outward growing 'non-protective' multilayered scale. In fact, certain of the M_2O_3 lines appeared to be duplicated from the early stages of oxidation, suggesting regions of different chromium content in different parts of the thin protective scale. Equally, however, *all* the M_2O_3 lines decreased in lattice spacing together indicating a common temporal trend (Newcomb 1983). The M_3O_4, as formed locally on the alloy, exhibited a lattice parameter appropriate to an Fe–Cr_2O_4 spinel. It should be emphasized that the lateral coexistence of difference phases coupled with vertical gradations in the chemical composition can lead to peak broadening to a degree which makes such data of only marginal application.

The X-ray data obtained for the 10Cr–10Ni alloy oxidized in air is anomalous in that it would appear that an α-M_2O_3 scale of almost 90% chromium content was the exclusive oxidation product after 1000 h. Such a result is not explained by the spalling observed for this alloy and is inconsistent with weight gains and 'edge-on' TEM observations, all of which indicated multicomponent 'non-protective; scale formation. The only explanation we have is that the particular specimen used for X-ray observations did not oxidize in the same unstable way as the smaller specimens used for TEM sectional observation. If this is so then it simply re-emphasizes the generally chemical unstable behaviour of this alloy, observed for the Fe–9Cr–1Mo alloy. The data obtained for the 10Cr–20Ni and 10Cr–34Ni alloys was generally consistent with that obtained by other techniques. In particular, the M_2O_3 formed on 10Cr–34Ni exhibited lattice parameter changes as a function of time (Newcomb 1983) which were characteristically interpretable in terms of a progressive temporal increase in chromium content and thus presumably associated with some regions of 'protective' oxide formation. Equally a larger lattice parameter was observed for the M_3O_4 at earlier oxidation times, implying a generally lower chromium content. This is simply indicative of the small volume fraction of the inward growing M_3O_4 present at short oxidation times and does not, when viewed in conjunction with 'edge-on' TEM analysis, imply any strong temporal trend in the composition of the main outward growing scale of nearly pure Fe_3O_4 (superposed by Fe_2O_3).

The rapid development of thick layers of near pure magnetite as the outer scale on all the alloys when they were oxidized in 1% CO–CO_2 precluded any useful data being obtained on the inward forming M_3O_4 scales, though the peak broadening generally observed as consistent with the presence of M_3O_4 from the earliest stages of oxidation.

(*c*) *Scanning electron microscopy*

Considering firstly the air oxidized samples, the surface of a typically thin 'protective' and unspalled region of the scale formed on the industrial Fe–9Cr alloy is shown in figure 3*a*, plate 2. The EDS analysis (see inset) indicates an Fe:Cr ratio of 3:1, but its accuracy is limited by contributions from the subscale alloy (see paper I). A typical region of nodular growth in the same specimen is shown in figure 3*b*. Here the outer layer of the scale has a 'whisker and blade'-like morphology, consistent with the oxide being haematite (Fe_2O_3) (Tallman &

Gulbransen 1968), though EDS analysis, whose acuracy is in this case limited by the presence of the surrounding chromium rich 'protective' scale gave both iron and chromium peaks.

Surprisingly, given all other data than that obtained by X-ray diffractometry, some unspalled regions of 'protective' oxide were also identified on the air oxidized 10Cr–10Ni alloy, as shown in figure 3*c*. Other areas of the alloy surface were covered with rather thicker oxide, consisting of an outer layer of haematite (figure 3*d*), typical of the growth of a multiphase scale (Metcalfe 1979). EDS analysis of this region gave only an iron peak (inset figure 3*d*), consistent with the growth of Fe_2O_3.

SEM examination of the surface of the scale formed on Fe–10Cr–20Ni showed that oxide spalling had taken place from most of the surface of this alloy and optical microscopy indicated that scale separation takes place at the Fe_3O_3–M_3O_4 interface (see, for example, figure 5*b*). A micrograph of the spalled surface is shown in figure 3*e* and the rough surface of the M_3O_4 is characteristically different from the topography of the 'protective' scales seen in figures 3*a* and *c*, as formed on localized regions of the 9Cr–1Mo and 10Cr–10Ni alloys. (The 'protective' M_2O_3 scales on Fe–9Cr–10Mo may also be compared with those seen for the Fe–20Cr–Ni alloys (Newcomb *et al.* 1986)). In fact, our 'edge-on' electron microscopy of the region of the scale formed on Fe–10Cr–20Ni (see §3.1) demonstrated that the layer in figure 3*e* is made up of both M_3O_4 and austenite containing a relatively large percentage of nickel as is consistent with the EDS analysis shown. The few unspalled regions of the specimen examined showed a typical haematite layer, the EDS analysis of which gave only an iron peak.

The outer scale formed on the austenitic Fe–10Cr–34Ni is shown in figure 3*f* and is again haematite with both a whisker and a blade morphology typical of this type of oxide growth on an iron based aloy. We have previously described the transmission electron microscopy of this outer scale, as scraped from the alloy surface, and confirmed its structure as that of α-Fe_2O_3 (Newcomb *et al.* 1983).

The outer scales seen on all the alloys when oxidized in 1% CO–CO_2 were adherent and essentially indistinguishable from one another. A typical region of the outer scale formed on Fe–10Cr–10Ni is shown in figure 4, plate 3 and its characteristic 'hopper-like' morphology should be noted. Oxides with a similar open and uniform structure have been observed on both austenitic (Allan *et al.* 1974) and ferritic (Harrison 1976) steels oxidized in CO_2. The surfaces of these scales, whose EDS analysis indicated that they are magnetite (Fe_3O_4), are also similar to the nodular and locally 'non-protective' regions of oxide growth identified on the Fe–20Cr–2Ni and Fe–20Cr–20Ni alloys (see I).

(*d*) *Optical microscopy*

While the optical microscopy of the thin 'protective' scales formed on Fe–20Cr–Ni yielded little useful information (Newcomb *et al.* 1986), the optical examination of sections of the alloys described here was particularly helpful both in clarifying the lateral inhomogeneity of the oxide development and the relatively irregular inward oxidation and carburization of the different materials.

Typical regions of the multilayered oxides, formed after 1000 h oxidation in air, are shown in figure 5, plate 4. The micrographs show that oxide growth has taken place both into and away from the original metal surface. Figure 5*a*, for example, shows a region of thin 'protective' oxide formed on 9Cr–1Mo, as arrowed, and an area where a multiphase oxide, approximately 10 μm in thickness, has been formed. The thin layer of oxide acts as a marker for the position

TABLE 5. SUMMARY OF THE OXIDATION CHARACTERISTICS OF THE Fe–9Cr–1Mo AND Fe–10Cr–Ni ALLOYS OXIDIZED IN AIR AT 600 °C

(The data refer to the oxides formed after 1000 h.)

alloy	Fe–9Cr–1Mo	Fe–10Cr–10Ni	Fe–10Cr–20Ni	Fe–10Cr–34Ni
alloy microstructure				
pre-oxidation				
XRD	α	α	γ	γ
TEM	α	α	γ	γ
post-oxidation				
XRD	α	α+γ	α+γ	γ
TEM	α	α	γ	γ
X-ray diffraction				
lattice parameters/nm				
M_3O_4 a_o	0.838	—	0.825	0.825
a_H[a]	0.50	0.50	ND	0.50
α–M_2O_3 c_H[a]	1.32	1.36	ND	1.35
oxidation kinetics				
mass gain/mg cm^{-2}	1.25	9.50	7.65	4.90
n	3.25	0.75	2.00	1.92
$10^{12}\,k_p/(g^2\,cm^{-4}\,s^{-1})$	0.434	25.1	16.3	6.67
$k_n/(g\,cm^{-2})^n\,s^{-1}$	1.02×10^{-16}	8.45×10^{-9}	1.63×10^{-11}	9.03×10^{-11}
optical metallography				
scale thickness/μm	0.5–10	55–90	50–80	0.5–40
scanning electron microscopy				
surface morphology	crystallite (Cr_2O_3) and nodules (Fe_2O_3)	crystallite (Cr_2O_3)	spall and whisker (M_3O_4) (Fe_2O_3)	whisker (Fe_2O_3)
transmission electron microscopy				
oxide identification	α | M_2O_3 || α | M_3O_4 | Fe_3O_4	α | M_3O_4 | γ+ M_3O_4 | Fe_3O_4	γ | M_3O_4 | γ+ M_3O_4 | Fe_3O_4	γ | M_2O_3 || γ | M_3O_4 | Fe_3O_4 || γ | M_3O_4 | γ+ M_3O_4 | Fe_3O_4
alloy[b]–oxide Fe:Cr:Ni composition (% by mass)				
Fe	90 | 54 || 90 | 19.5 | 79 | 95.5		69 | 88 | 63[c] | 95 | 56	58 || 57.5 | 8.3 | 71.1 | 96 || 54.7 | 78.2 |
Cr	7 | 37 || 7.5 | 78.5 | 17 | 2.5		10 | 2 | 23[c] | 2 | 7	37 || 7.5 | 86.1 | 19.6 | 2 || 10.1 | 5.9 |
Ni	— | — || — | — | — | —		20 | 10 | 12[c] | 2 | 34	2 || 34.2 | 5.1 | 8.8 | 1.5 || 34.7 | 15.3 |
oxide thickness/μm	0.2 || 3 | 7.5	25 | 25	20 | 15	0.07 || 2 | 2 || 15 | 8
oxide grain size/μm	0.25 || 0.1 | 2–3	0.075 | 1–2.5	0.05–0.2 | 1–2	0.1 || 0.05 | 1 || 0.05–0.1 | 1.2

[a] Indexing based on equivalent hexagonal unit cell.

[b] Data refers to the alloy composition 50 nm from the metal–oxide interface.

[c] Data refers to the composition of M_3O_4.

The broken lines refer to the position of the metal surface before oxidation, the solid lines refer to the positions of inner oxide interfaces, the double lines separate different behaviours.

ND, no determination.

of the metal surface prior to oxidation, and indicates unequivocally that growth of the inner oxide, in the *ca.* 10 μm multiphase scale, has taken place *into* the alloy.

The 65 μm oxide layer seen in figure 5*b*, as formed on Fe–10Cr–10Ni was thicker than that found on the other 'low' chromium alloys, and although this correlates with the mass gain results, it remains inconsistent with the X-ray data described earlier (see §2*b*). The typically three layered oxide consists of haematite, magnetite and an iron chromium spinel, the latter having grown into the alloy, as was confirmed by 'edge-on' TEM.

Multiphase scales were also identified on both the austenitic alloys Fe–10Cr–20Ni (figure 5*c*) and Fe–10Cr–34Ni (figure 5*d*). The thickness of the scale seen here on Fe–10Cr–20Ni was *ca.* 55 μm compared with up to 25 μm observed for the Fe–10Cr–34Ni. Although this difference is consistent with the mass gain data (table 3) it should be noted that the scaling observed on the Fe–10Cr–34Ni alloy was particularly heterogeneous with local scale thickness variations of at least a factor of ten. While the outer layer of haematite formed on the 'non-protective' scale regions was prone to separation at the Fe_3O_4 interface during the preparation of the section, the impression gained from figure 5*d* that this alloy could be oxidized locally in a number of different ways was confirmed by TEM (see §3*a*). Preferential growth of M_3O_4 spinel into the metal occurred in the 20 and 34Ni materials via the alloy grain boundaries as has been previously reported for Ni–Cr steels (Wood & Hodgekiess 1966). In a number of areas this can lead to the parent alloy becoming completely surrounded by oxide as shown arrowed for the Fe–10Cr–20Ni alloy in figure 5*c*.

Similar types of inward oxidation were observed on both the 10Cr–20Ni and 10Cr–34Ni alloys when they were oxidized in CO–CO_2 (figure 6*c*, *d*, plate 5) though in neither case did etching in 5% nital reveal any carburization. Also typical regions of the thick oxides formed on the Fe–9Cr and Fe–10Cr–10Ni alloys after 1000 h oxidation in 1% CO–CO_2 are shown in figure 6*a* and *b* respectively. All the CO–CO_2 scales were shown to consist of two oxide layers of similar thicknesses with the double layers formed on the ferritic alloys being thicker than those formed on the austenitic materials, as is consistent with the mass gain data (§2*a*). All the specimens shown in figure 6 were etched in 5% nital and it can be seen that carburization has occurred for the 9Cr–1Mo and 10Cr–10Ni alloys to a depth of between 150 and 200 μm from the metal–oxide interface. It will be remembered that when 'protective' scaling occurs in CO–CO_2 on the 20Cr alloys with the same nickel content it is the 'high' nickel austenitic alloys which carburize (see paper I). Now in the 10Cr austenitic materials we find a change in behaviour in which inward *oxidation* of a characteristically 'non-protective' type replaces the inward diffusion of carbon.

Optical micrographs of the three 10Cr–Ni alloys after 125 h exposure to 1% CO–CO_2 are shown in figure 7, plate 6. Comparison of the scales formed after this period with those shown in figure 6 demonstrates unequivocally that the inward and outward growth of oxides occurs progressively and simultaneously. This is a characteristic of 'non-protective' scaling behaviour in the way we have defined it, and is distinct from the typically intermittent surges of oxidation associated with mechanical scale breakdown in 'breakaway' (Holmes *et al.* 1974).

3. Transmission electron microscopy

The bulk of the detailed microstructural and microchemical data obtained on the oxidation behaviour of the alloys discussed here has been obtained by the examination of 'edge-on'

specimens prepared as described both in paper I and in more detail elsewhere (Newcomb 1983). We will describe the results for the air oxidized specimens in §3*a* and those for the 1% CO–CO_2 oxidized specimens in §3*b*.

(*a*) *Oxidation in air*

We have already seen (§2) that the outermost scale formed in air on all the 10Cr–Ni alloys was α-Fe_2O_3 but it did not prove to be possible to retain this part of the scale in general on specimens prepared for 'edge-on' examination in the TEM. No detailed information can thus be given on the specific interface region between the haematite and the outward growing magnetite beneath it, although preliminary observations of this interface are reported elsewhere (Newcomb & Stobbs 1985). Typical examples of this very open part of the upper scale were, however, examined by TEM, as scraped from oxidized samples, and the general structure and whisker morphology of the Fe_2O_3 thus confirmed (Newcomb *et al.* 1983). The results obtained by the 'edge-on' technique for each of the alloys, as discussed below, were obtained for specimens oxidized for 1000 h.

(i) Fe–9Cr–1Mo(α)

As has already been demonstrated (§2) Fe–9Cr–1Mo can exhibit both 'protective' and 'non-protective' scaling behaviours (figure 5*a*). Use of the 'protective' oxide as a marker for the surface of the metal before oxidation gives very clear evidence of the fraction of the 'non-protective' scale which grows into the metal. Here we concentrate on the appearance of the 'non-protective' scale as formed under nodules such as that shown in figure 3*b*. The microstructure of the retained outward growing oxide, which was *ca.* 7.5 μm in thickness, is shown in figure 8*a*, plate 7. The oxide structure here was that of an FCC spinel (the inset diffraction pattern shows a (112) normal) and the columnar morphology, with a grain size of *ca.* 2–3 μm, is typical of the growth of favourably oriented magnetite grains. EDS analysis of such regions indicated a uniform cationic percentage of chromium of only about 2.5% contrasting with the steady increase in chromium content towards the subscale alloy in the inward growing fine grained (*ca.* 100 nm) M_3O_4, which extended for about 3 μm beneath the original metal surface. The microstructure of this inward growing scale in the region of the metal–oxide interface is shown in figure 8*b*, while a cationic concentration profile across the entire scale and underlying alloy is shown in figure 9. It may be seen from this that the chromium content of the alloy beneath the scale was depleted, over a depth of approximately 3 μm, and to about 7.5% at the metal–oxide interface. The appearance of the allow in this region (figure 8*b*), although ferritic, no longer exhibits the more martensitic structure observed prior to oxidation (see figure 1*a*).

A region of the 'protective' scale is shown in figure 8*c*. As observed in this area, it was only *ca.* 0.2 μm in thickness and had an extremely *flat* interface with the subscale alloy as well as a fairly large grain size (by comparison with that of the inward growing M_3O_4). It is interesting to compare the oxidation behaviour of such an alloy where it is behaving 'non-protectively', and yet in terms of the overall mass gain with a power law of $n \approx 3$, with that of an essentially 'protective' scale as formed on Fe–20Cr–2Ni (see paper I). It was argued in paper I that such an alloy exhibits at least some inward development of a scale which is of α-M_2O_3 structure and fairly large inner chromium content, as well as a marked depletion in alloy chromium levels to a value very similar to that seen beneath the well developed inward growing scale on 9Cr–1Mo. For both alloys it can be argued that the essentially cube law kinetics are associated with a

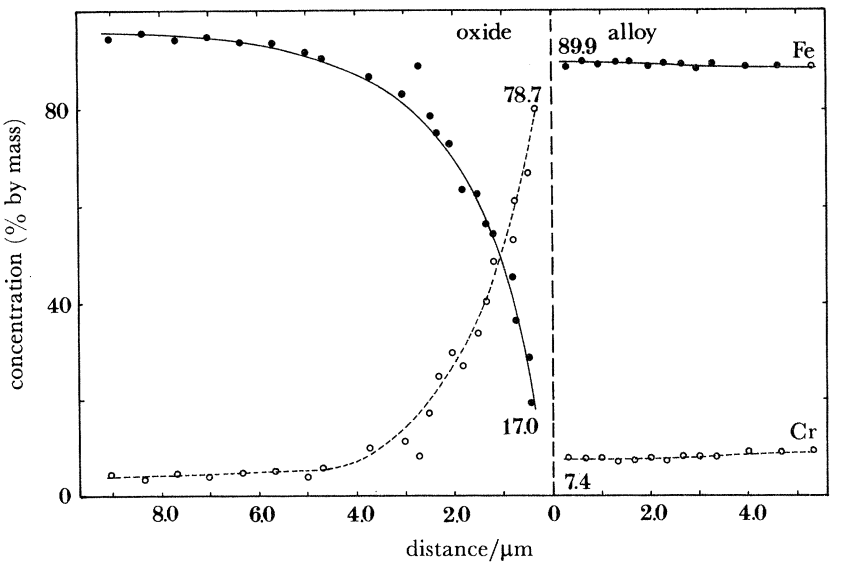

FIGURE 9. Composition profiles for the Fe–9Cr–1Mo and the M_3O_4–Fe_3O_4 scale formed after 1000 h in air at 600 °C.

progressive temporal reduction in chromium level beneath the scale, while the larger mass gains of the 'non-protective' 'lower' chromium alloy are presumably associated with the larger cation diffusion rates in both the Fe_3O_4 and M_3O_4 scales by comparison with those to be expected for M_2O_3 (Kofstad 1966).

(ii) Fe–10Cr–10Ni(α)

The 'non-protective' scale microstructure observed after 1000 h on this alloy was complex. The 'protective' scale implied by X-ray diffraction and found in small localized regions by SEM was not characterized but would be expected to be similar to that described for Fe–9Cr–1Mo. Considering firstly the outward growing magnetite in the 'non-protective' scale, shown near to the original metal surface in figure 10*a*, plate 8, where it may be seen that the grains, of size 1–2 μm, are largely defect free. The defect density in the magnetite grains increases, however, towards the outer regions of this part of the scale, and an area nearer to the Fe_3O_4–Fe_2O_3 interface is shown in figure 10*b–d*. The contrast exhibited by the defects of the type arrowed, which was sensitive to deviation parameter, is not inconsistent with their being cracks. It will be remembered that the oxidation kinetics exhibited by this alloy were extremely rapid suggesting both ready ingress of oxygen and a progressive break-up of the oxidizing surfaces.

A low magnification image of the generally homogeneously fine grained (*ca.* 50 nm) inward growing oxide is shown in figure 11*a*, plate 9. This 'orientated inward' (OI) oxide (shown at higher magnification in figure 11*b*) proved to be an M_3O_4 spinel, as imaged in dark field in figure 11*c*, in close association and epitaxial orientation with transformed unoxidized alloy of austenitic structure (figure 11*d*). This austenite was also identified by the X-ray diffractometry of the originally ferritic specimens and the transformation is indicative of the enrichment of the alloy with nickel rejected from the M_3O_4 grains as they form. Such an alloy enrichment in nickel was demonstrated for the originally austenitic Fe–10Cr–20Ni alloy which exhibited a similar morphology of inward growing oxides with retained regions of unoxidized austenite. While the epitaxial orientation of the transformed alloy and associated OI oxide is demonstrated

in figure 11*e*, *f* showing respectively (011) and (112) γ-M_3O_4 diffraction patterns, a few larger 'random inward' (RI) spinel grains of size between 250 and 750 nm were identified lower in this region, as shown in figure 12*a*, plate 10, and these were *not* oriented in any specific manner with the oxide.

That these RI oxides are formed in the originally ferritic matrix prior to the OI oxidation and transformation of the alloy is demonstrated by the examination of regions beneath those described above. A low magnification image of a region near the diffuse metal–oxide interface is shown in figure 12*b*. Here the local alloy is already austenitic indicating that the infilling fine grained M_3O_4 forms epitaxially in this alloy structure rather than in ferrite with simultaneous alloy transformation. Such an inference is equally consistent with the originally non-epitaxial orientation of the larger RI oxide grains found only in these low regions of the scale.

The alloy also oxidized preferentially at grain boundaries, although not to the extent that this occurs in the higher nickel content alloys. A region of such grain boundary enhanced oxide growth is shown in figure 12*e*, as arrowed, where the surrounding alloy matrix is still ferritic and of approximately (011) orientation. It should also be noted that the inset SADP (figure 12*f*) shows that an M_3O_4 spinel, orientated $(011)\alpha//(111)M_3O_4$, was formed on the surface of the alloy during thin foil specimen preparation. The same orientation relationship has been observed for the initial stages of the growth of magnetite on pure iron (Boggs *et al.* 1967). Convergent beam electron diffraction indicated that the inward grown oxide as seen here, deepest within the specimen at the grain boundary, was an M_3O_4-type spinel; a (233) microdiffraction pattern is shown in figure 12*g*. No specific orientation relationship was however found in these regions between the oxide and ferritic alloy which, as may be seen from figure 12*f* is of a more recovered structure than before oxidation (see figure 1*b*).

(iii) Fe–10Cr–20Ni(γ)

The optical microscopy of the 10Cr–20Ni specimen (figure 5*c*) indicated that this austenitic alloy formed a 50–80 μm scale of similar morphology of that of the 'non-protective' regions on the Fe–10Cr–10Ni specimens.

The 'outer' oxide formed was again magnetite (Fe_3O_4) and a typical region of the spinel is shown in figure 13*a*, plate 11, where the grain size of the oxide was approximately 1–2 μm. The coarse grained oxide was characteristically defect-free while EDS demonstrated its high iron content, the cationic composition being 95% Fe, 2% Cr, 2% Ni.

The oxide beneath the layer of coarse grained magnetite was found to be in-grown and to consist of cube–cube orientated spinel and austenite. A typical region of this part of the scale as formed beneath the unoxidized metal surface is shown in figure 13*b*. EDS was used to differentiate between the composition of the two phases but was of limited accuracy, given beam spreading, since the metal and oxide were both of fine (50–200 nm) grain size. The austenitic compositions obtained, typically 25% Fe, 7% Cr and 67% Ni, demonstrated the strong rejection of nickel from the fine grained 'orientated inward' oxide which was of cationic composition 63% Fe, 23% Cr and 12% Ni. It should however be noted that the average nickel content is *larger* than for the bulk alloy. The similar oxidation behaviour in this region, to that seen in Fe–10Cr–10Ni (once the ferrite has been transformed to austenite after the first oxides form with the associated rejection of nickel into the matrix) is demonstrated by figure 13*c*, *d*, which shows dark-field micrographs of the austenite and spinel in the 'random inward' scale respectively.

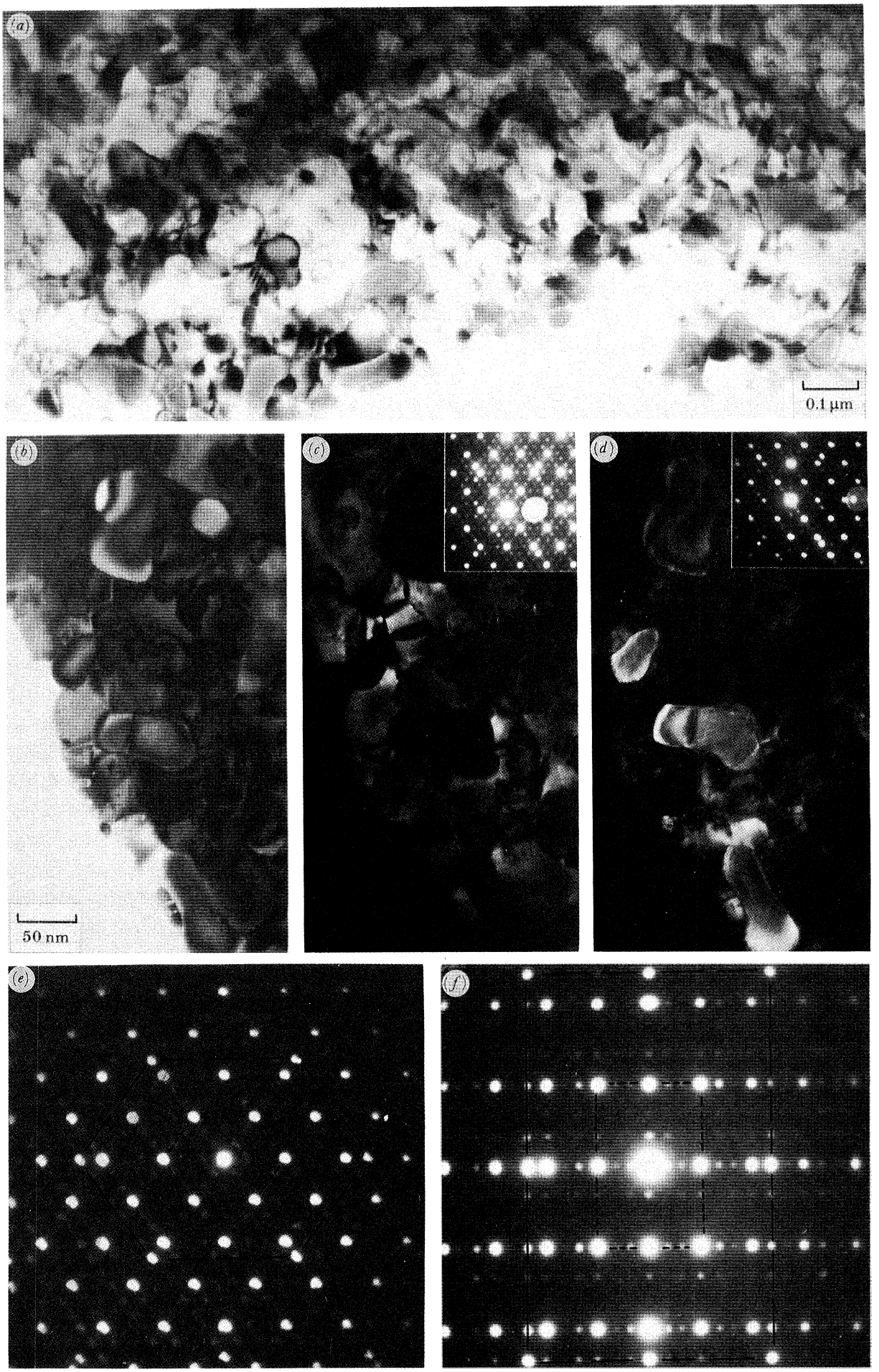

FIGURE 11. For description see plate 12.

(*Facing p.* 230)

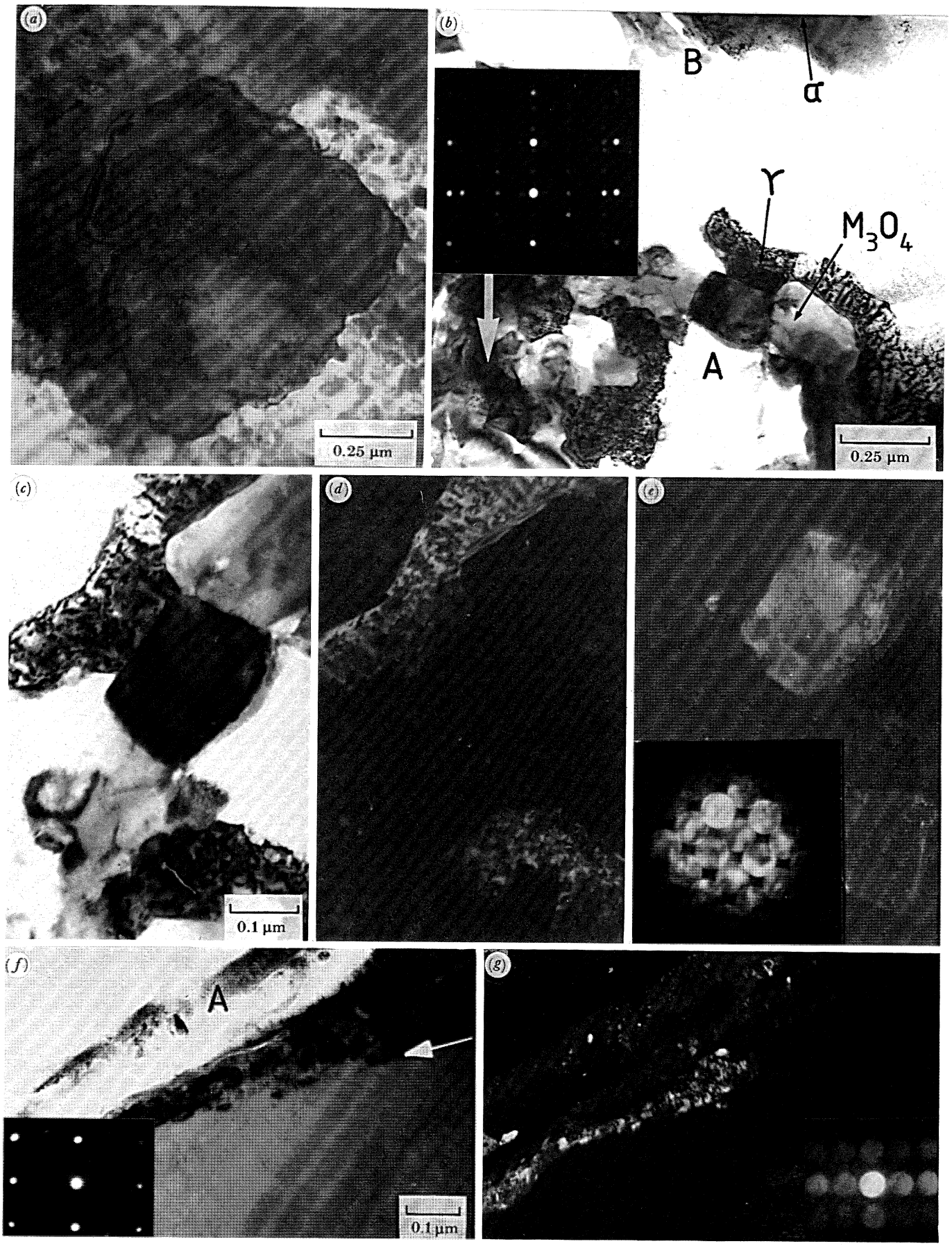

FIGURE 12. For description see plate 12.

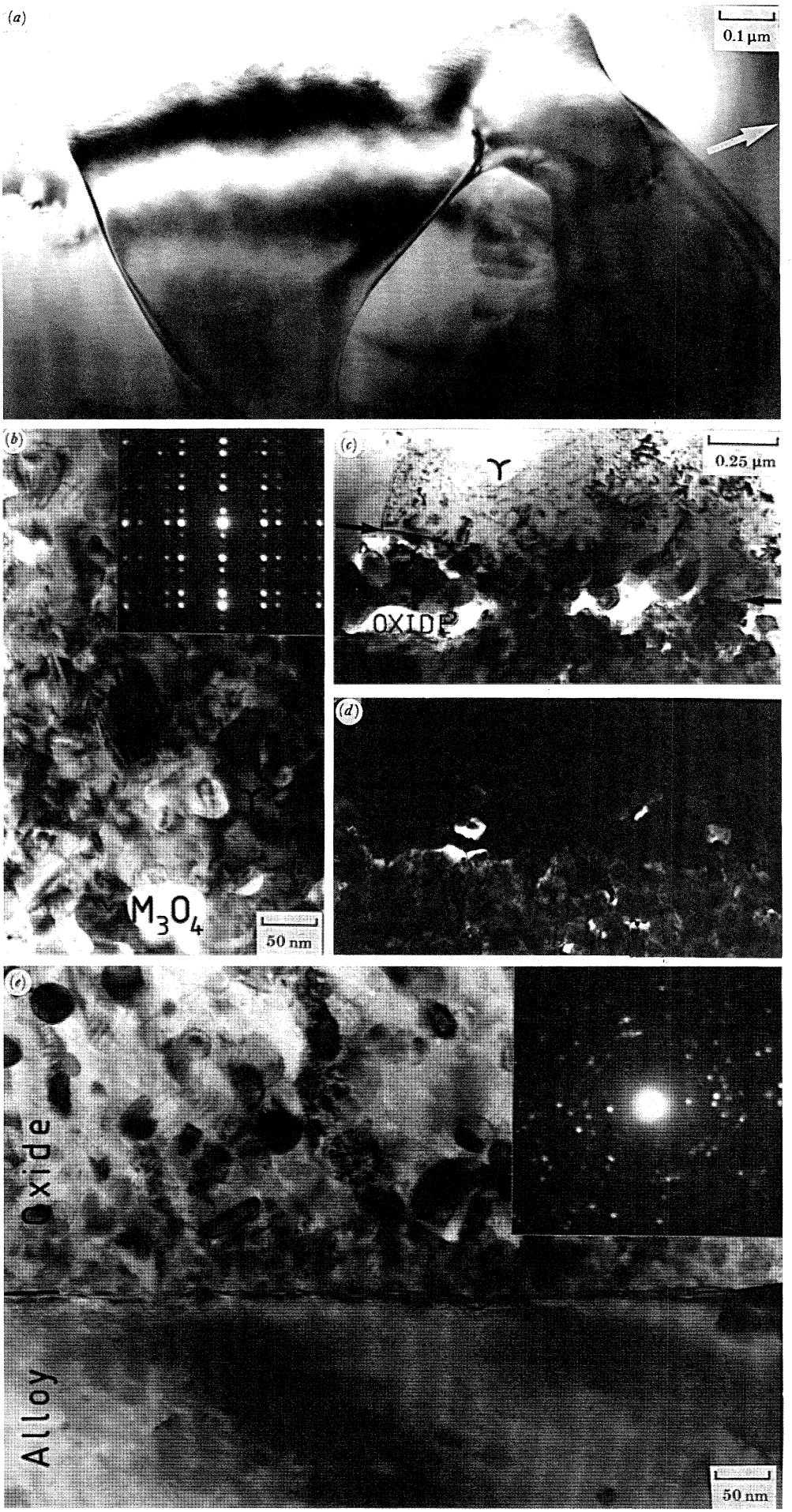
(a)
0.1 μm
(b)
M_3O_4
50 nm
(c)
0.25 μm
OXIDE
(d)
(e)
oxide
Alloy
50 nm

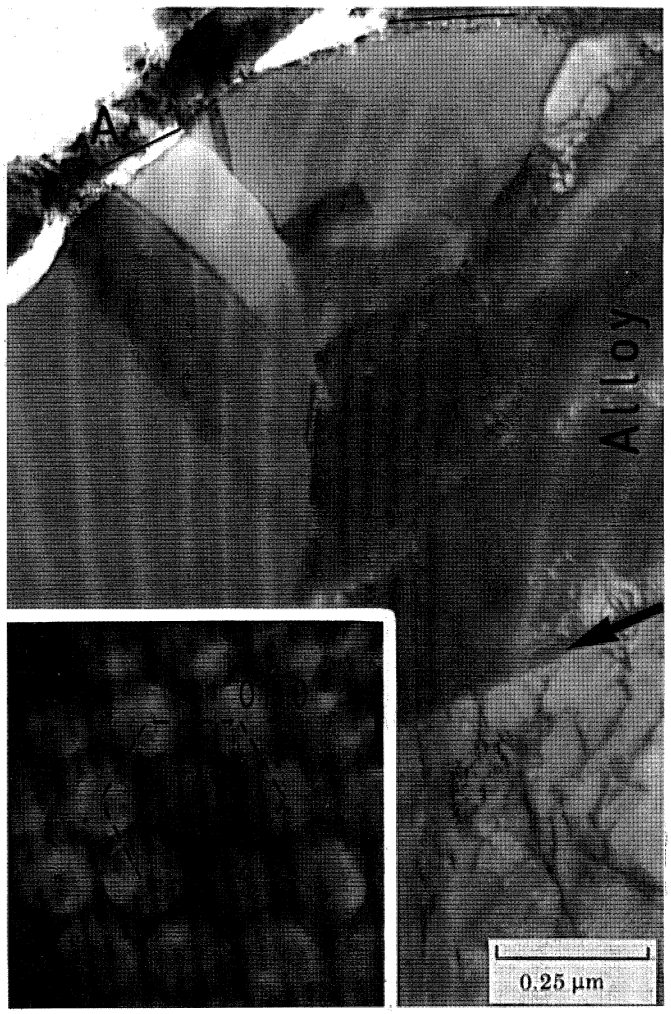

FIGURE 14. Fe–10Cr–34Ni oxidized in air for 1000 h at 600 °C showing a thin layer of 'protective' oxide sandwiched between the alloy and supportive nickel plate, as at A. Note that the alloy shows partial recrystallization to a depth approximately 1 μm beneath the scale, as arrowed.

DESCRIPTION OF PLATE 9

FIGURE 11. Microstructure of the 'internal' scale formed on Fe–10Cr–10Ni in air at 600 °C after 1000 h. (*a*) Low magnification bright field image of an area approximately 15 μm from the metal–oxide interface, (*b*) higher magnification bright-field, (*c*) dark-field (imaged with a (200) spinel reflection), (*d*) dark-field (imaged with a (200) austenite reflection). Diffraction patterns demonstrating the epitaxial relationship between austenite and the larger lattice parameter oxide are shown in (*e*) $(011)_\gamma//(011)_{M_3O_4}$ and (*f*) $(112)_\gamma//(112)_{M_3O_4}$.

DESCRIPTION OF PLATE 10

FIGURE 12. Fe–10Cr–10Ni oxidized in air for 1000 h at 600 °C in air showing the scale microstructure in the metal–oxide interface region, 'edge-on' TEM. (*a*) Coarse grained RI M_3O_4 surrounded by epitaxial, and finer grained, $\gamma//M_3O_4$ scale, situated approximately 2.5 μm from the alloy–oxide interface and approximately 10 μm beneath the region shown in figure 11. (*b*) Low magnification bright-field micrograph of the diffuse alloy–oxide interface. A region of OI oxide is arrowed (see inset diffraction pattern) which is approximately 1 μm beneath the alloy–oxide interface, while the ferritic alloy is also marked as at B. A region of RI oxide and transformed alloy as at A is shown enlarged in (*c*), (*d*) and (*e*). (*c*) Bright-field micrograph from A in (*b*), (*d*) dark-field, imaged with an austenite reflection, and (*e*) dark-field, imaged with a spinel reflection. The inset shows a $(233)_{M_3O_4}$ diffraction pattern. (*f*) Grain boundary oxide formation (arrowed) in the ferritic 10Cr–10Ni alloy, as at B in (*b*). Note the microcrystalline sputter contamination at A, some of which is imaged in (*g*) and the surface oxide formation in the ferrite (see inset diffraction pattern). (*g*) Dark-field, imaged with a spinel reflection. The inset shows a $(100)_{M_3O_4}$ diffraction pattern.

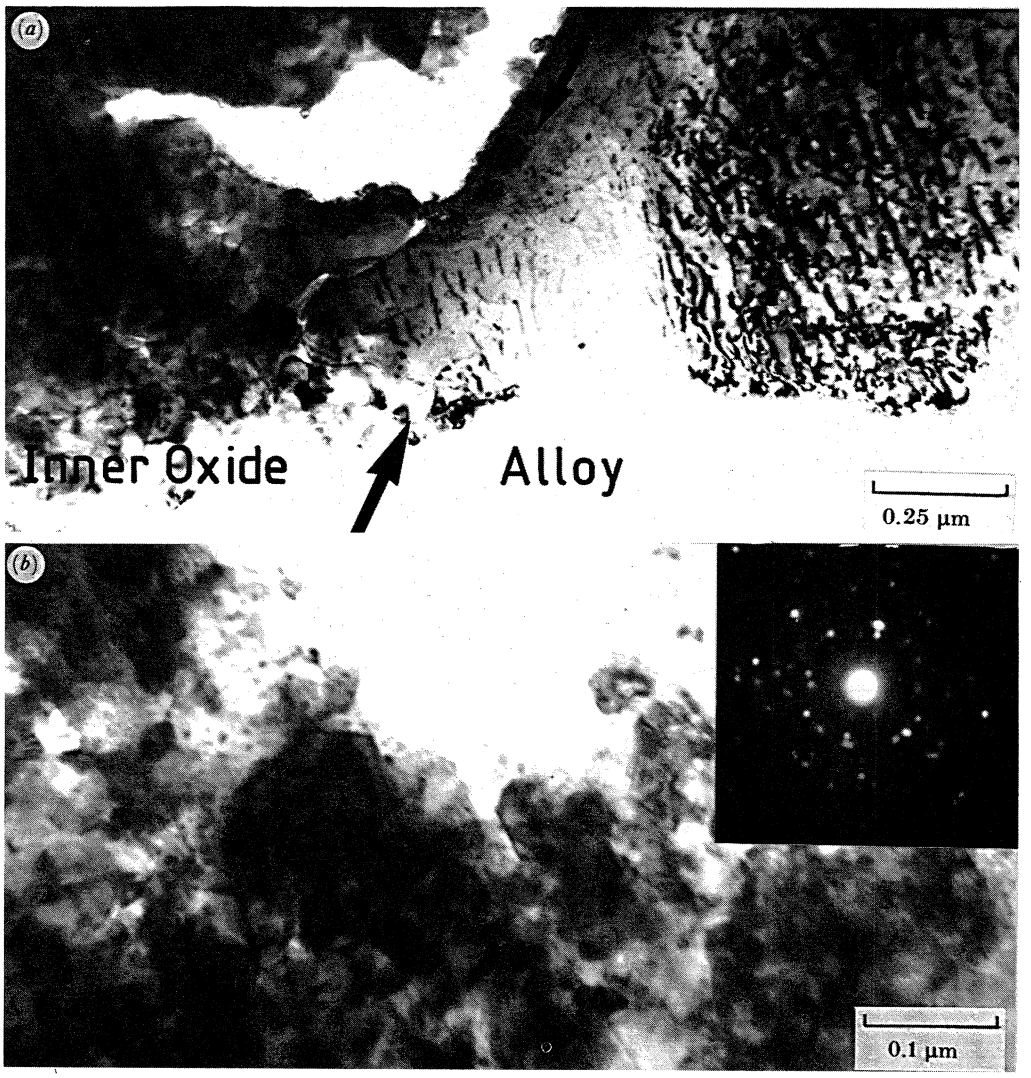

FIGURE 15. Fe–10Cr–34Ni oxidized in air for 1000 h at 600 °C showing 'non-protective' and RI oxide (*a*) at the metal–oxide interface, which is arrowed. A region which has preferentially ion-beam milled to form a large hole may be seen in the oxide. (*b*) The fine grained RI oxide approximately 1 μm from the metal–oxide interface. The M_3O_4 oxide is untextured, as demonstrated by the inset diffraction pattern.

DESCRIPTION OF PLATE 11

FIGURE 13. Fe–10Cr–20Ni oxidized in air for 1000 h at 600 °C. (*a*) Microstructure of the coarse grained and columnar magnetite layer. The arrow is normal to and approximately 5 μm from the original metal surface. Here the oxide is characteristically defect free. (*b*) A region of OI scale approximately 10 μm from the original metal surface. The epitaxial relationship between the two phases is shown in the inset diffraction pattern. (*c*) A *ca.* 1 μm grain of unoxidized (and nickel enriched) austenite encapsulated by RI fine grained spinel oxide. Bright-field and (*d*) dark-field, as imaged with a spinel reflection. The arrows in (*c*) and (*d*) delineate the interface between the RI oxide and the austenite. (*e*) The metal–oxide interface, where the scale consists of fine grained M_3O_4 and does not contain austenite (see inset diffraction pattern).

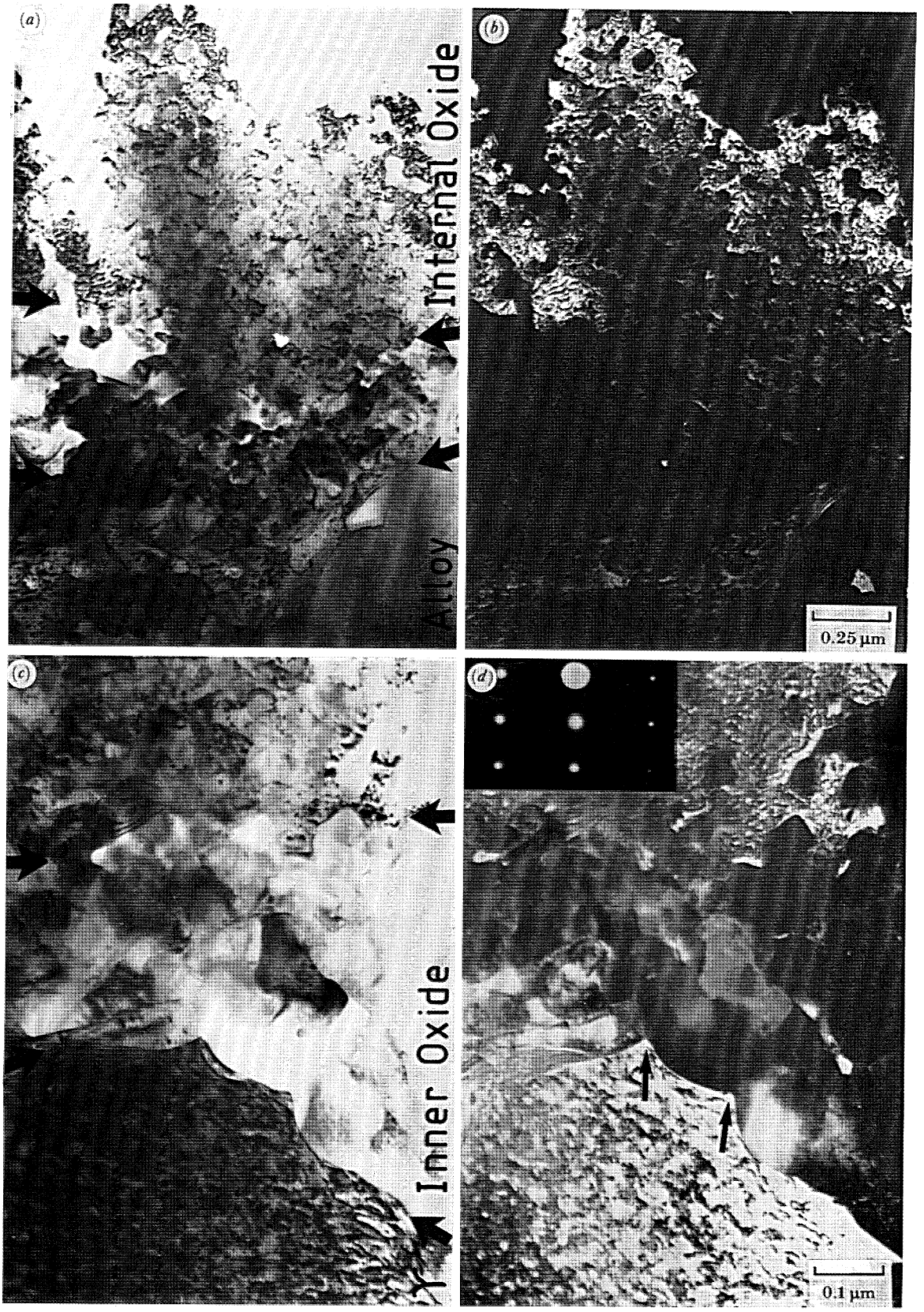

FIGURE 16. Fe–10Cr–34Ni oxidized for 1000 h in air at 600 °C showing the 'non-protective' scale in the region of the metal–oxide interface. (*a*) A band (*ca.* 250 nm) of RI oxide is sandwiched between the alloy and OI oxide above it, as delineated by the arrows. Bright-field and (*b*) dark-field (imaged with a spinel reflection), which shows the oxide in the region of the OI scale (cf. figure 11*c*). (*c*) RI oxide at the metal–oxide interface showing the cusped morphology of the scale growth. Bright-field and (*d*) dark-field (imaged with an austenite reflection) showing that the austenite in the OI oxide above the 'inner' spinel has an identical orientation as in the alloy.

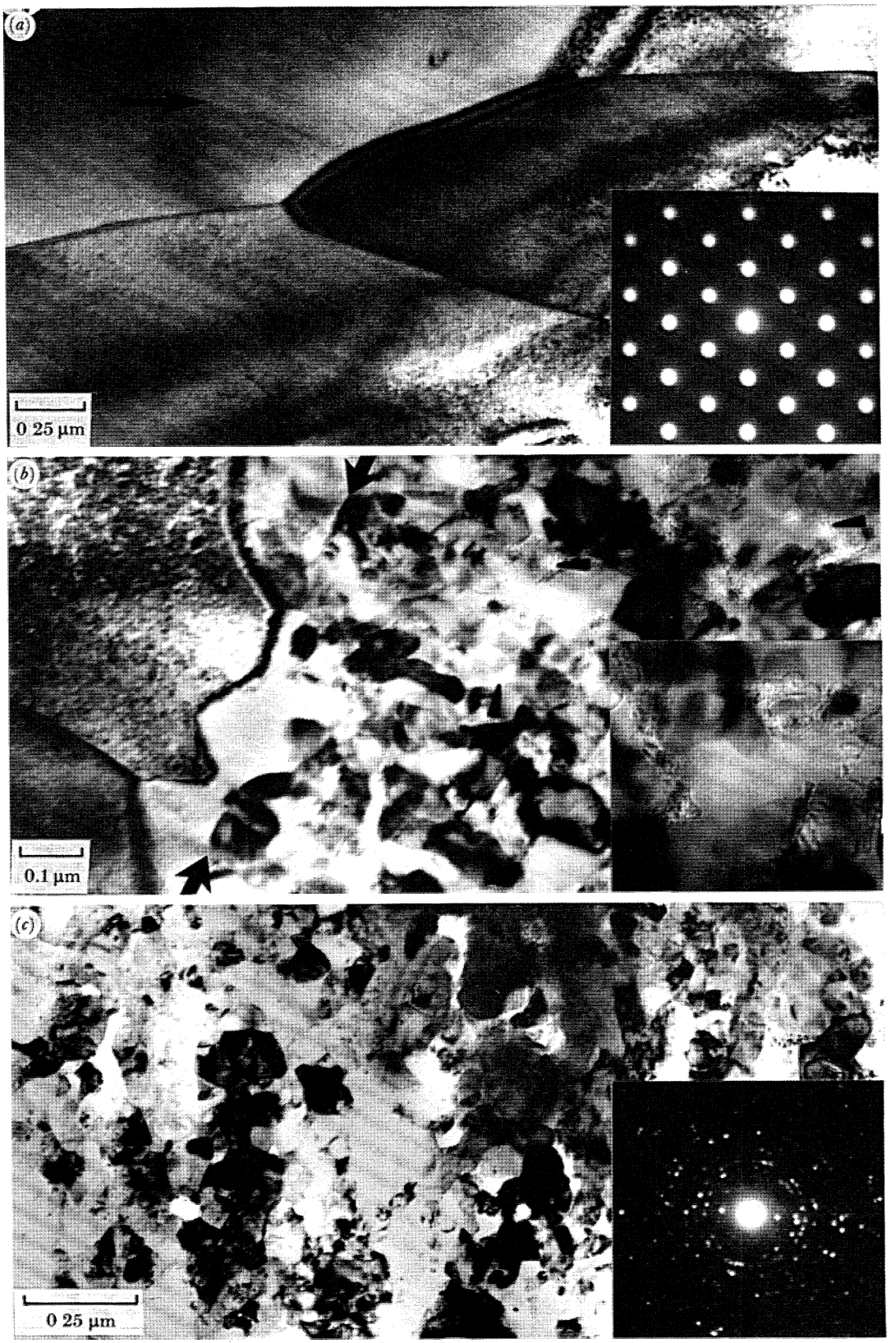

FIGURE 17. Fe–9Cr–1Mo oxidized in 1% CO–CO_2 for 1000 h at 600 °C. 'Edge-on' TEM. (*a*) Columnar grained magnetite. The arrow is normal to and approximately 3 μm from the duplex oxide interface. The inset shows a $(110)_{Fe_3O_4}$ diffraction pattern. (*b*) The duplex oxide interface where the position of the original metal surface is arrowed. Pores in the underlying fine grained oxide are also marked and are shown enlarged in the inset. The contrast of the pores has been Fresnel enhanced. (*c*) A typical region of fine grained inner oxide approximately 20 μm from the duplex oxide interface, which is untextured as shown by the inset diffraction pattern.

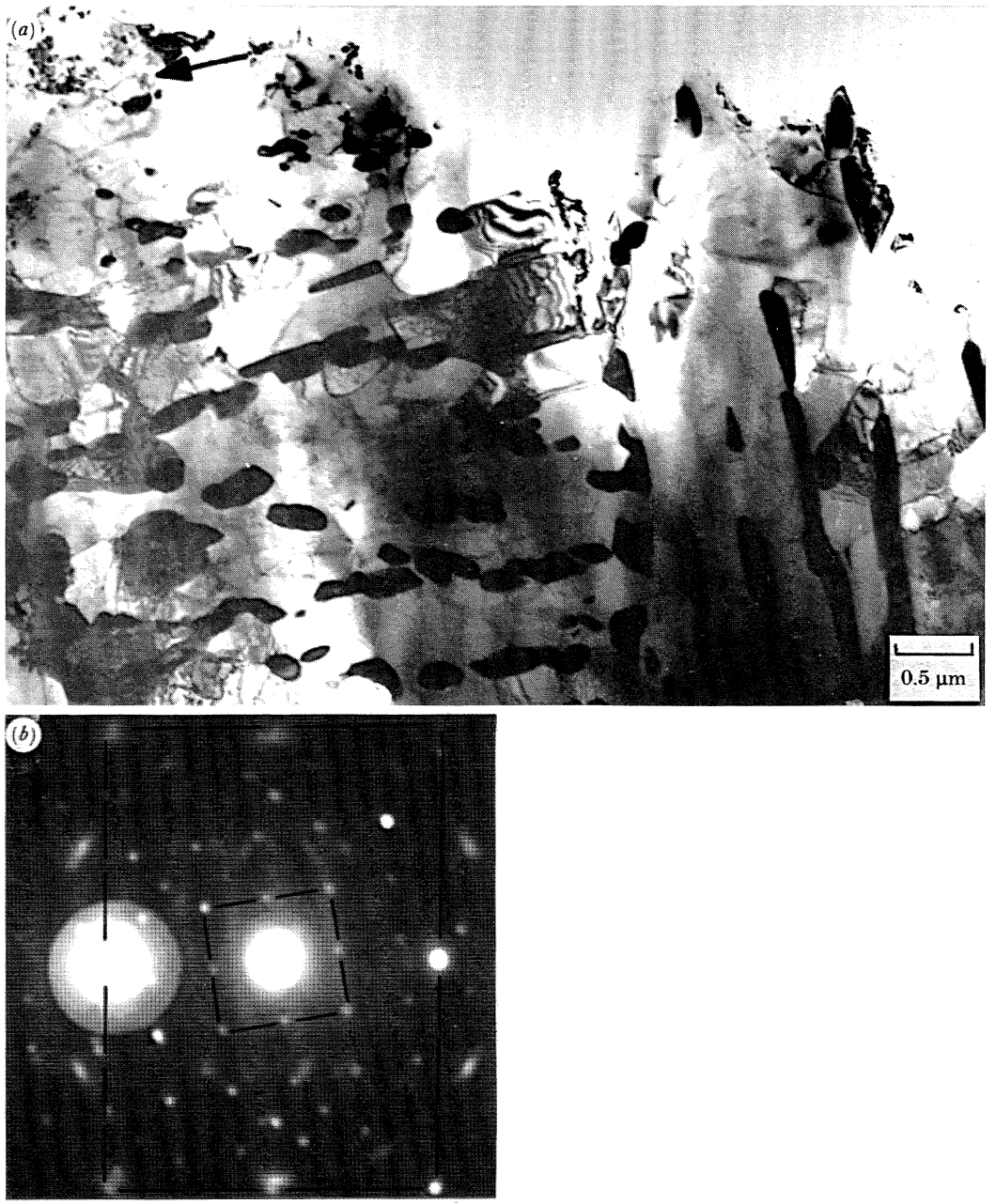

FIGURE 18. Fe–9Cr–1Mo oxidized in 1% CO–CO_2 for 1000 h at 600 °C showing the morphology and structure of the ferrite beneath the scale. (*a*) Bright-field micrograph showing carbide precipitates in the ferrite in the region of the alloy–oxide interface (arrowed). (*b*) $(011)_\gamma//(001)_{M_{23}C_6}$ diffraction pattern, the orientation relationship being as marked.

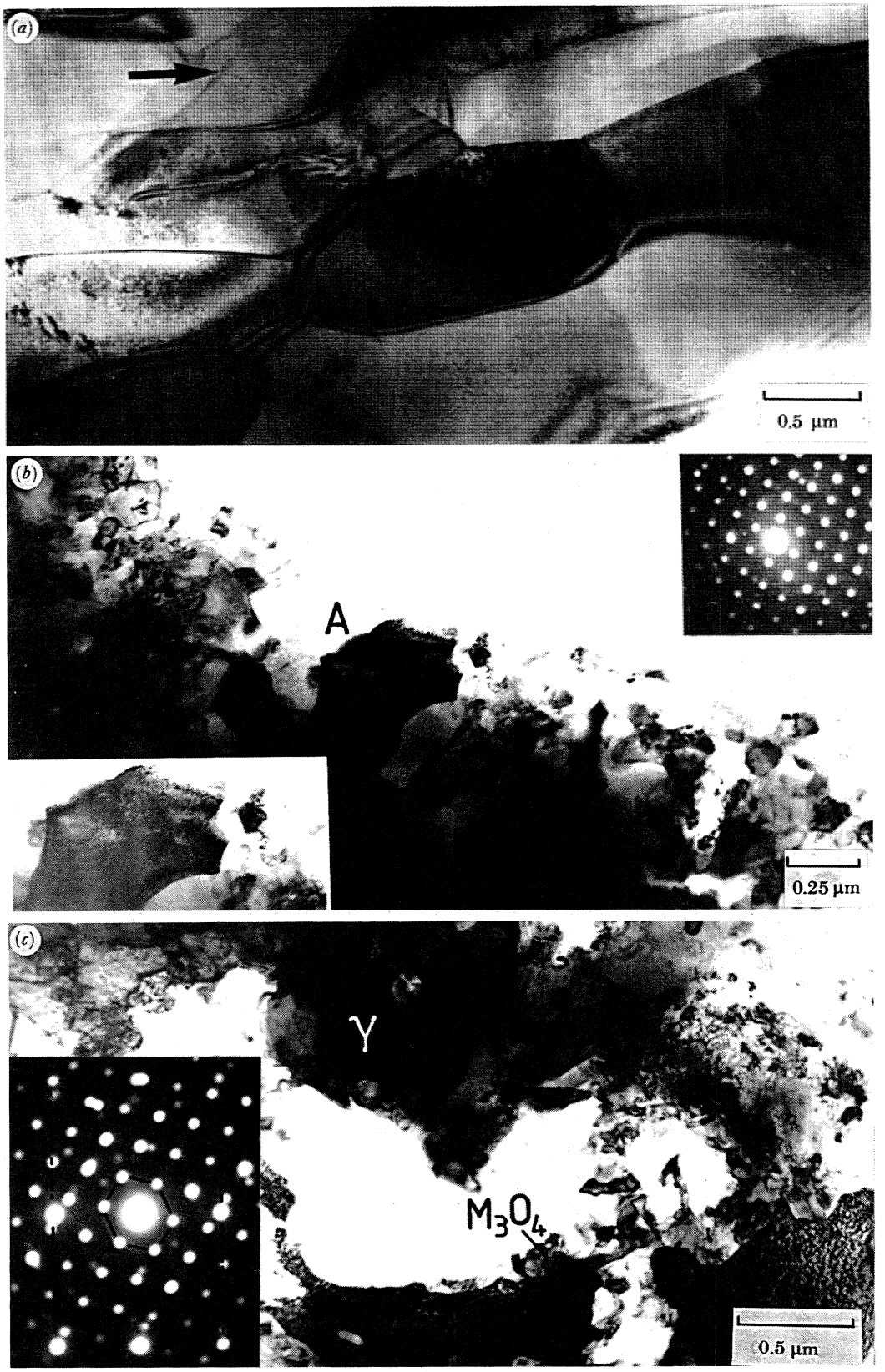

FIGURE 19. Fe–10Cr–10Ni oxidized in 1 % CO–CO_2 for 125 h at 600 °C showing: (*a*) columnar magnetite grains; the arrow is normal to and approximately 5 μm from the duplex oxide interface; (*b*) fine grained inner spinel oxide approximately 5 μm beneath the duplex oxide interface; a large spinel grain (see inset $(110)_{M_3O_4}$ diffraction pattern) may be observed at A and is shown enlarged in the inset micrograph; (*c*) a region of austenite and M_3O_4; here the two phases are orientated $(112)_\gamma//(011)_{M_3O_4}$ as shown in the inset diffraction pattern.

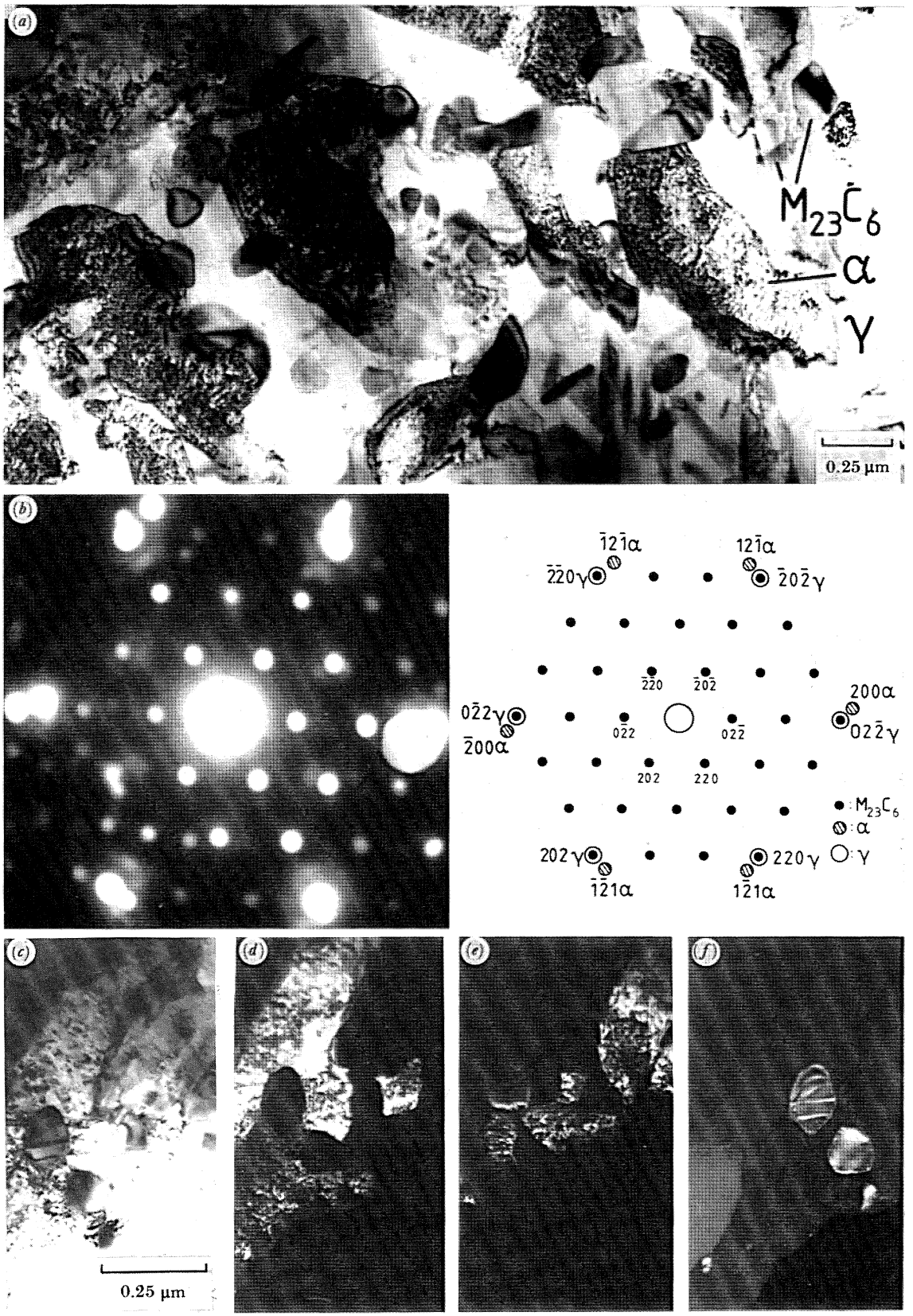

FIGURE 20. Fe–10Cr–10Ni oxidized in 1 % CO–CO_2 for 125 h at 600 °C. 'Edge-on' TEM showing the microstructure of the OI oxide approximately 100 μm beneath the duplex oxide interface. (*a*) Bright-field micrograph showing ferrite, austenite and $M_{23}C_6$ carbides, as marked; (*b*) $(012)_\alpha//(111)_\gamma//(111)_{M_{23}C_6}$ diffraction pattern; (*c*) Bright-field and (*d*) dark-field (imaged with a (200) ferrite reflection); (*e*) dark-field (imaged with a (220) austenite reflection); (*f*) dark-field (imaged with a (220) carbide reflection).

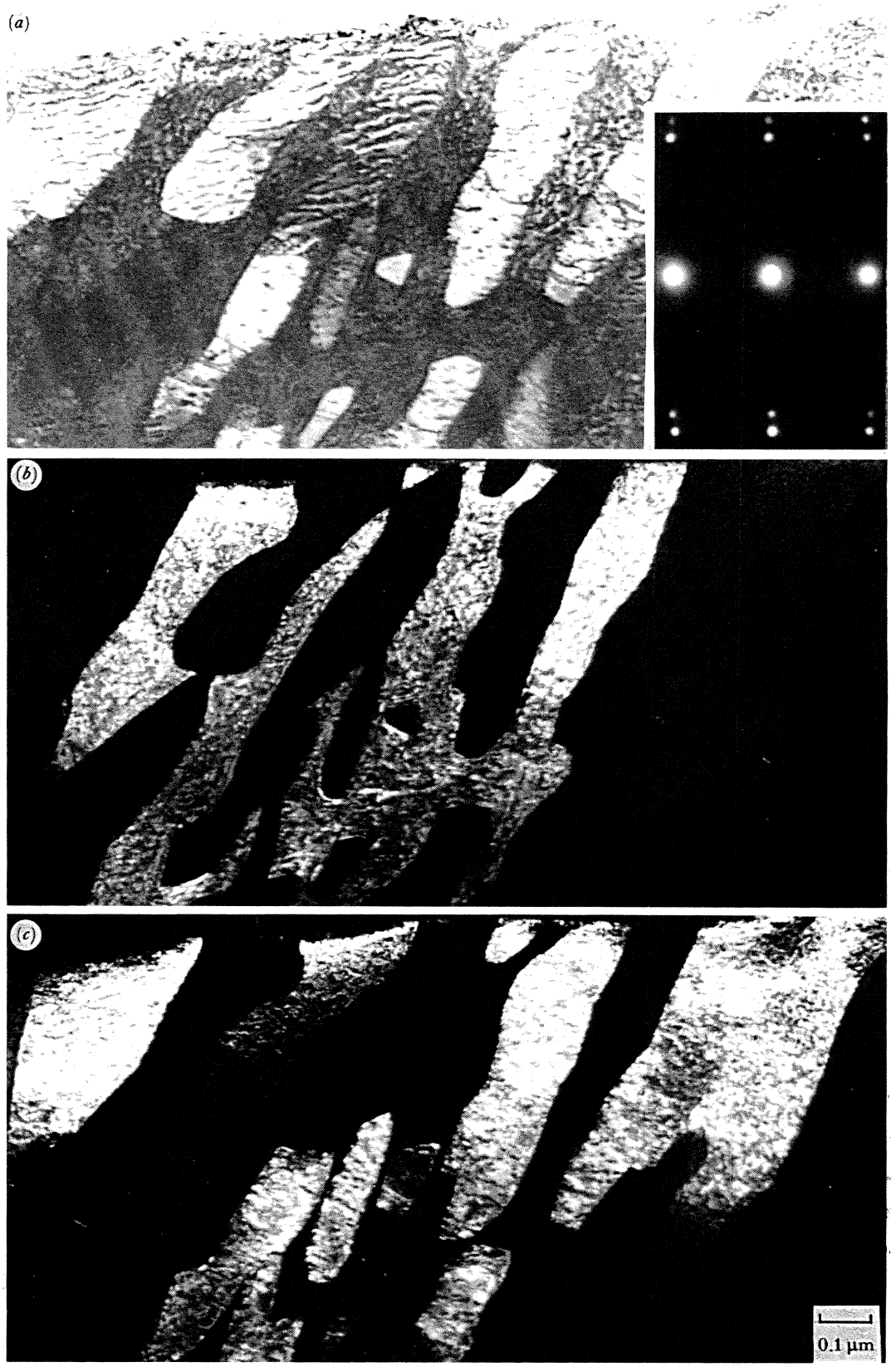

FIGURE 21. Microstructure of the Fe–10Cr–10Ni alloy after oxidation in 1 % CO–CO_2 for 125 h at 600 °C showing: (*a*) the duplex alloy microstructure; the inset shows a $(011)_\alpha//(112)_\gamma$ diffraction pattern; (*b*) dark-field (ferrite); (*c*) dark-field (austenite).

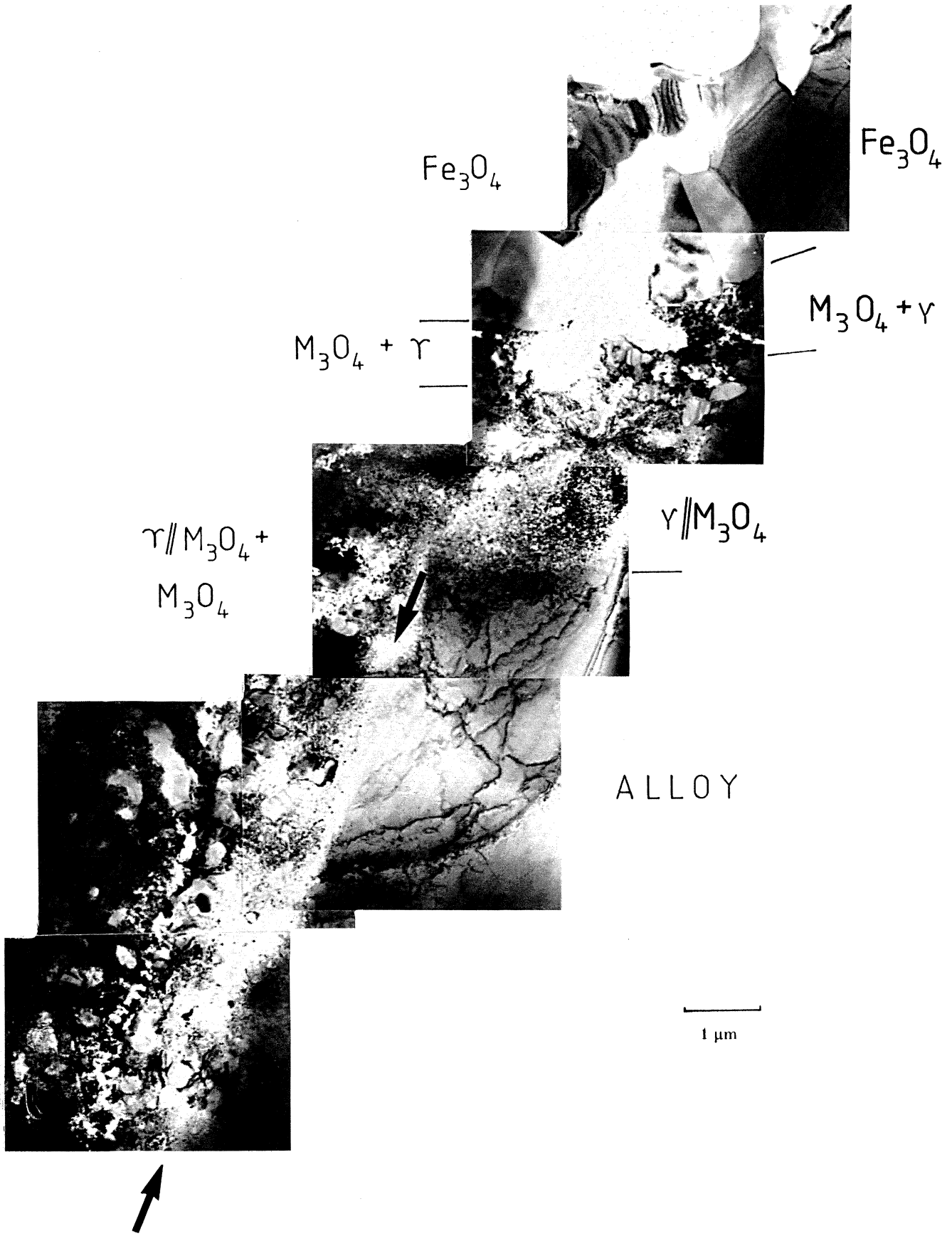

FIGURE 22. Bright-field TEM montage of the duplex scale formed on Fe–10Cr–20Ni in 1 % CO_2 after 125 h at 600 °C showing a region of preferential oxide growth at an alloy grain boundary (arrowed). The discreet layer of RI scale at the duplex oxide interface below which there is OI oxide should be noted.

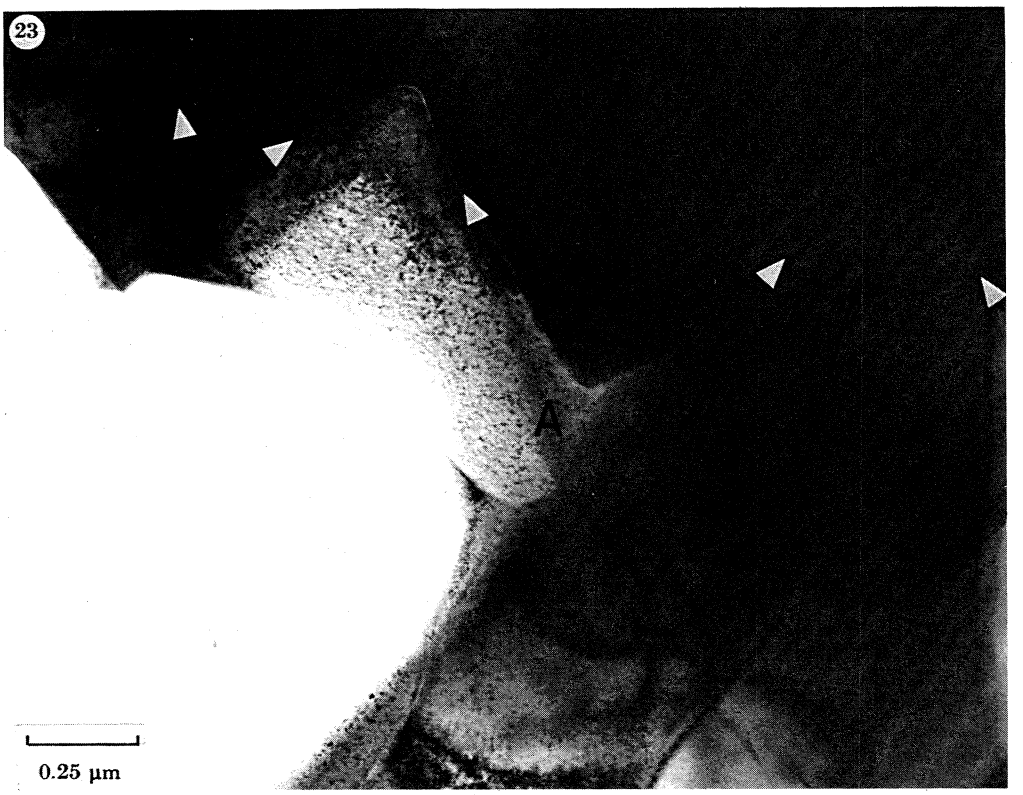

FIGURE 23. Microstructure of the magnetite formed on Fe–10Cr–20Ni after 125 h oxidation in 1 % CO–CO_2 at 600 °C. The image shows the scale at the oxide–gas interface, where the magnetite–nickel plate interface is marked. (The plate is used in the preparation of the 'edge-on' foils.) Grain boundaries in the magnetite are arrowed, which are regions where enhanced oxide growth has occurred, leaving cavities in the surface of the scale, as at A.

FIGURE 24. The duplex oxide interface in the scale formed on Fe–10Cr–20Ni after 125 h in 1 % CO–CO_2 at 600 °C. The interface is arrowed. Note the fine grained morphology of the RI oxide which exhibited an iron and chromium concentration gradient.

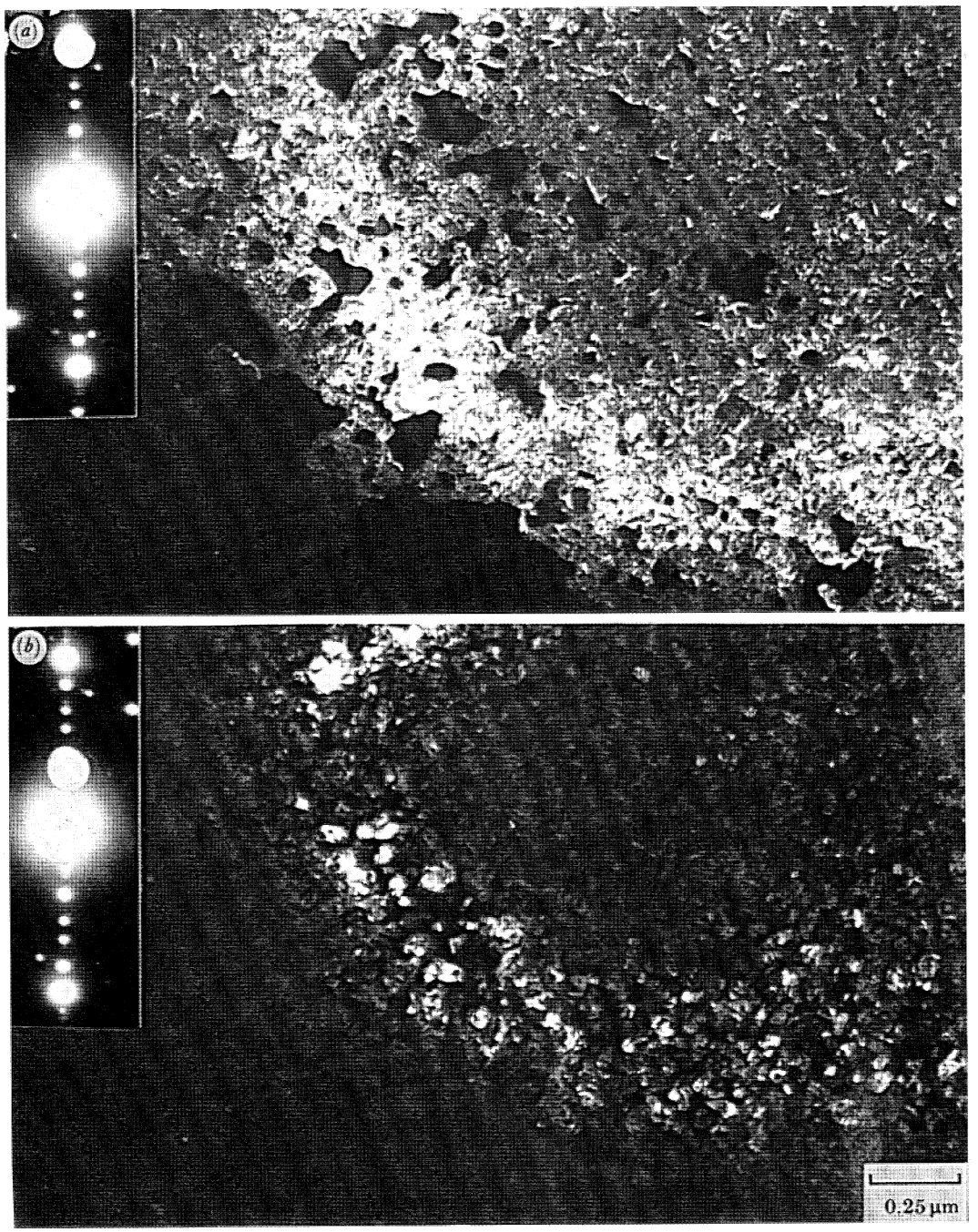

FIGURE 25. Microstructure of the inner scale formed at a grain boundary in Fe–10Cr–20Ni after 125 h in 1 % CO–CO_2 at 600 °C: (*a*) Dark-field micrograph, imaged with an (020) austenite reflection; (*b*) dark-field micrograph, imaged with an (020) spinel reflection. There are no indications that this RI oxide is porous.

DESCRIPTION OF PLATE 23

FIGURE 26. Fe–10Cr–20Ni oxidized in 1 % CO–CO_2 for 1000 h at 600 °C: (*a*) showing regions of cube–cube orientated austenite and spinel approximately 20 μm beneath the Fe_3O_4–M_3O_4 interface; (*b*) dark-field (austenite); (*c*) dark-field (spinel); (*d*) showing the diffuse metal–oxide interface approximately 50 μm beneath the Fe_3O_4–M_3O_4 interface; (*e*) dark-field (austenite); (*f*) dark-field (spinel).

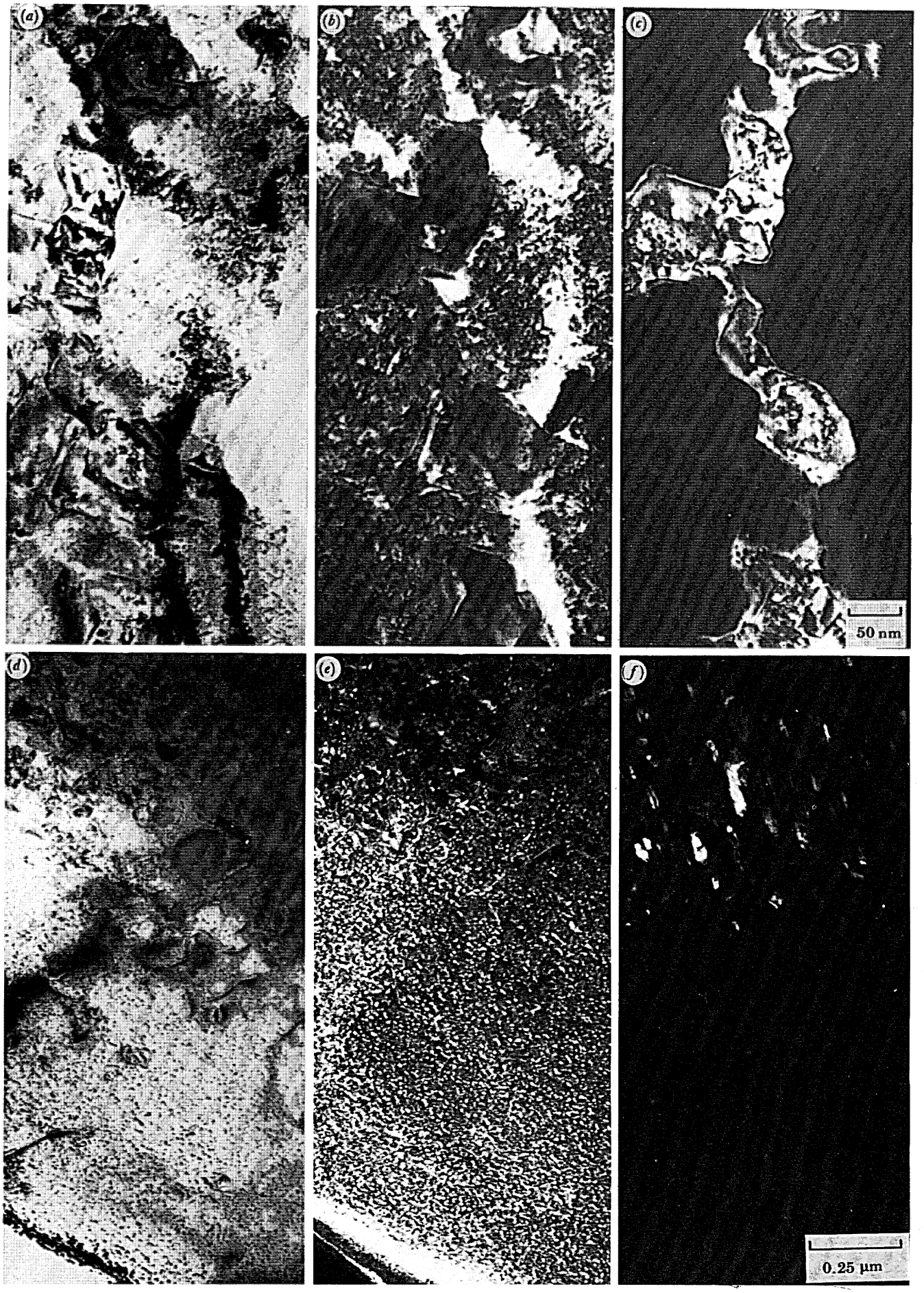

FIGURE 26. For decription see opposite.

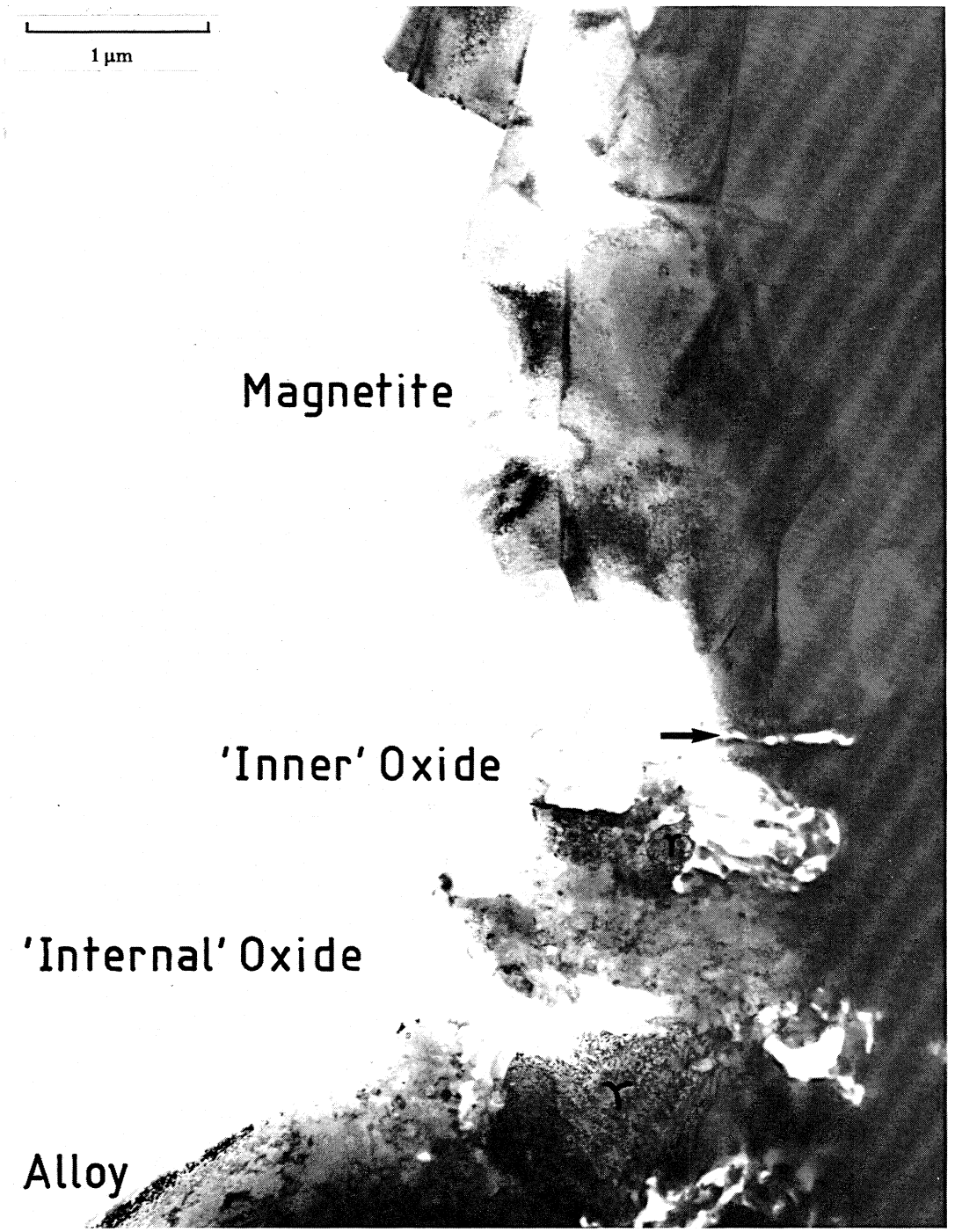

FIGURE 27. 'Edge-on' bright-field micrograph of the duplex scale formed on Fe–10Cr–34Ni in 1 % CO–CO_2 after 125 h at 600 °C. The microstructure of the inner oxide layer is complex and contains austenite. Note the partial spallation at the duplex oxide interface (arrowed) and that the oi oxide contains some large holes formed by 'etching' during ion beam thinning.

Relatively large grains of austenite were found to be retained within lower regions of the inner scale as a result of the preferential growth of the inward growing oxides at grain boundaries, as inferred from the optical micrographs of sections of the scale (figure 5*c*). Interestingly, the fine grained spinel surrounding such retained austenite did *not* itself contain austenite grains. While the large retained austenite grains were somewhat more depleted in chromium and enriched in nickel than the fine grained regions in the oxide away from the grain boundaries, the fully oxidized regions (as presumably formed at an early stage around the grain boundaries) were of higher chromium and lower nickel content than the spinel coexisting with austenite.

Away from grain boundaries the lower interface of the inward growing fine grained spinel had a relatively flat interface with the unoxidized substrate which, rather surprisingly, showed *no* chromium depletion or nickel enrichment. In this region (figure 13*e*) the spinel was of cationic composition, 88% Fe, 2% Cr and 10% Ni. Given the fine grained co-existence of austenite and 'orientated inward' oxide *above* this region, it is at first sight extraordinary that this 'random inner' oxide was both continuous and exhibited no orientation relationship with the sub-alloy scale. Because of the strong tendency for grain boundary oxidation in this alloy (figure 5*c*) it might be considered possible that here we are simply seeing the meeting of the inward oxidizing microstructure with prior fully oxidized material at such grain boundaries. The form of the region shown in figure 13*e* is not, however, suggestive of this type of process and furthermore no interface of the inward growing type of microstructure containing retained austenite with fully unoxidized austenite was ever found. The metal–oxide interface was *always* fully oxidized and fine grained, and exhibited the characteristics of a RI rather than OI oxide. Fully oxidized RI interfaces of the inward growing oxide with the subscale alloy were also identified in the Fe–10Cr–34Ni alloy with equally clear regions of OI oxide coexisting with fine grained austenite *above* them. Coupling this observation with the relative lack of chromium depletion in the zone beneath such regions, away from grain boundaries, it would thus appear that initially fully oxidized inward growing scales are then partially *reduced* with the further fractional uptake of iron into the regions remaining oxidized, together with the coupled rejection of nickel into the austenite thus now formed epitaxially with the oxide rather than the other way round. An alternative and more probable mechanism for the formation of this RI scale will be considered at greater depth in §5.

(iv) Fe–10Cr–34Ni(γ)

The scaling behaviour of the Fe–10Cr–34Ni alloy was, as has already been demonstrated by optical microscopy (figure 5*d*), particularly heterogeneous. In consequence, a number of sections through the alloy–scale interface were examined by 'edge-on' TEM and three distinct modes of oxidation were differentiated.

One type of scale found over relatively large areas of the specimens was characteristically 'protective' and consisted of an approximately 70 nm thick layer of fine grains (100 nm) of α-M_2O_3 with a chromium to iron ratio of 6:4, a value rather lower than that seen in the 'protective' scales formed on the 20Cr–Ni alloys in air. The scale was also very clearly two layered with a morphology (figure 14, plate 12) which we have previously associated with partial inward development (see paper I), there being indications that the inner third of the scale had grown into the austenite, probably essentially by cationic exchange (see §5). The alloy beneath the scale was both recrystallized and depleted in chromium (to 7% at the metal–oxide interface) to a depth of some 1.5 μm, in a similar manner to the high nickel

chromium alloys when oxidized in CO_2 and associated in that case with inward carbon diffusion. Such solute boundary drag effects are clearly not occurring in this case, but the recrystallization of the layer from which the chromium diffuses into the scale would progressively increase the tendency for iron rather than chromium to be drawn into the lower part of the 'protective' scale. Changes in the Fe:Cr ratio in the upper part of the scale are more likely to be controlled, as was discussed in paper I, by the changing relative diffusivities of the respective ions in the sesquioxide as its chemistry is itself changed.

Two types of 'non-protective' scale were characterized and it should be emphasized that we have no reason to believe that regions exhibiting these types of scaling behaviours were, before oxidation, chemically or microstructurally significantly different from one another. The first of these 'non-protective' scales consisted of an outer, and outward growing, layer of columnar grained magnetite with a very low chromium content, and an inward growing layer of fine grained RI spinel some 2 μm thick in the region characterized (figure 15, plate 13). The grain size of the spinel was fairly uniform (*ca.* 50 nm) throughout its thickness. The Fe:Cr:Ni ratios in the spinel ranged from 70:20:10 at the base of the magnetite to 10:85:5 at the spinel–alloy interface. Some small (*ca.* 200 nm) grains of austenite of very high nickel content were occasionally observed within the inner scale but they exhibited no particular orientation relationship to the untextured oxide grains around them. The interface between the spinel and the alloy where the chromium was depleted to 7.5% was much less flat than that of the superficially similar, but as we will find historically very different, spinel alloy interface in Fe–10Cr–20Ni. Equally in this type of region no 'orientated inward' spinel of the morphology seen in the Fe–10Cr–20Ni alloy was found between the 'random inward' spinel and outward growing magnetite.

The second type of 'non-protective' scaling observed on this alloy was however of similar character to that found on the Fe–10Cr–20Ni alloy but was of more limited extent. This allowed the gross microstructure of this interesting class of inward growing scale to be more easily characterized here than in the former alloy.

The metal–oxide interface region found on this alloy is shown in figure 16*a*, plate 14. The innermost part of the scale may be clearly seen to consist of a 250–500 nm band of fine grained 'random inward' M_2O_4 spinel bearing no obvious orientation relationship to the subscale austenite. *Above* this and nearer to the typical outward growing magnetite we again find coexisting epitaxial austenite and 'orientated inward' oxide, as demonstrated by the dark field spinel image in figure 16*b*. The only morphological difference between this apparently partially reduced region and the similar region in Fe–10Cr–20Ni, immediately beneath the outward growing scale, is that in the area characterized it was of more limited extent while the 'random inward' spinel beneath it would appear to be continuous over a slightly greater depth than in the lower nickel content alloy so that the regions of austenite above this layer were equally more isolated. The chemical composition of the inward moving RI oxide had a cationic concentration of 78% Fe, 6% Cr and 15% Ni, and while, as for the similar RI band in the 10Cr–20Ni alloy, there was no chromium depletion in the underlying alloy, concentration changes across the band could not be measured reliably. Equally, the average composition of this continuous band of fine grained spinel thus exhibits trends which parallel those seen in the RI oxide in the 10Cr–20Ni alloy.

Re-examining the region where the inward growing oxide in the interface region is continuous as shown in figure 16*c*, *d* we see the typical cusped morphology of an inward growing

scale and may also note that the austenite *above* and below this continuous RI *non*-epiaxially oriented oxide has an identical orientation. If this continuous scale is in fact progressively moving into the alloy this suggests that either there is preferential growth of those spinel grains growing into the alloy which do not bear a cube–cube orientation relationship with the alloy or that epitaxy is maintained by some other mechanism (see §5). The observation equally makes it still more difficult to imagine that the innermost continuous scales are formed at grain boundaries.

At this stage it is perhaps worth reconsidering an aspect of the inward scaling behaviour described above for the Fe–10Cr–10Ni alloy. It will be remembered that it was argued that the innermost, and thus first formed M_3O_4 grains, formed in ferrite and are relatively large. It should not be emphasized that grains of this type were *not* found nearer to the outward growing Fe_3O_4 scale. If we bear in mind the necessarily historical development as demonstrated by the position of a given structure in the section it would thus appear that in this alloy too, partial restructuring of the inward growing oxides occurs in the intervening regions of epitaxially oriented austenite and *solely* fine grained M_3O_4.

(*b*) *Oxidation in* 1 % $CO–CO_2$

It should be noted that whereas for oxidation in air all the results described in §3(*a*) were obtained for specimens oxidized for 1000 h, the typically larger weight gains obtained on oxidizing in 1 % $CO–CO_2$ made it preferable in some instances to examine the latter specimens after shorter oxidation times.

(i) Fe–9Cr–1Mo(α)

This alloy was examined 'edge-on' after exposure to 1 % $CO–CO_2$ for 1000 h and exhibited characteristic 'non-protective' scaling despite showing oxidation kinetics with $n = 2.14$. A typical region of the outer 35 μm of the scale is shown in figure 17*a*, plate 15. The grains which are of M_3O_4 spinel structure are typically 3–5 μm in size and columnar, while EDS analysis demonstrated that their cationic chromium content was less than 3 %. This outward growing scale is thus very similar to that seen on this alloy as oxidized in air where, that is, oxidation occurred in air 'non-protectively' (though in such cases the outermost regions of the magnetite were oxidized to haematite). It should be noted that the outward growing Fe_3O_4 formed in $CO–CO_2$ is completely non-porous at least in the 2 μm region nearest to the original metal surface. SEM examination of similar $CO–CO_2$ formed, but fractured scales (Rowlands & Manning 1981), has suggested that they contain channels extending from the outer oxide surface to the inner duplex oxide interface. Despite the examination of very large areas of the *outer* scale in 'edge-on' specimens no such channels could be found in the inner regions of the outward growing scale formed on Fe–9Cr–1Mo. At the base of the outer magnetite scale a finer grained (250–500 nm) Fe_3O_4 morphology was observed as shown in figure 17*b*, suggesting a nucleation period before the onset of the growth of the more favourably oriented columnar outer oxide morphology. No porosity could be found in this fine grained region of the outward growing oxide at the position of the original metal surface as marked in figure 17*b*. The inward growing fine grained (*ca.* 100 nm) oxide was however demonstrated to be porous throughout its 35 μm depth. A few of the fine (*ca.* 20 nm) irregular cavities in figure 17*b* are marked, their contrast being Fresnel enhanced in this image. The microstructure of this region of the scale is similar to that seen beneath nodules on the ferritic Fe–20Cr–2Ni alloy when this material

was oxidized in CO–CO_2 (see paper I). In neither case were carbides or carbon found within the inward growing scale. A region of the inward growing scale some 20 μm beneath that shown in figure 17*b* is shown in figure 17*c* and was equally porous but in this micrograph the contrast is not enhanced by viewing the region out of focus. Equally, however, it may be seen that the grain size is homogeneous throughout the 'random inward' scale and does not exhibit any texture. As in air, however, the chemical composition of the inward growing oxide exhibited a composition gradient with a higher chromium content in the oxide at the metal–oxide interface than nearer the original outer surface of the alloy (see table 6 and figure 29). It should be noted that no significant segregation was observed for the minor constituents of the alloy such as Mo, Mn and Si.

Optical microscopy (figure 6*a*) indicated carburization *beneath* the oxide scale to a depth of about 75 μm from the metal–oxide interface. The carbide morphology and microstructure are demonstrated by the micrographs shown in figure 18*a*, plate 16. It may be seen that the $M_{23}C_6$ is in a Kurdjumov–Sachs (K–S) orientation relation with the ferrite as demonstrated by the $(110)\alpha$–$(100)M_{23}C_6$ diffraction pattern shown in figure 18*b*. Typically the cation composition of the carbides was 45% Fe, 45% Cr, 3% Mn, 7% Mo with marked chromium depletion in the surrounding ferrite to values of 3%. It was found that the molybdenum concentration was still higher in carbides nearer to the metal–oxide interface and a carbide 100 nm from this interface contained Fe, Cr and Mo in ratio of 49:3:48. The historical development of this scale is as difficult to visualize as are some of those found on the higher Ni content alloys oxidized in air when it is remembered that there is here neither apparent trace element segregation in the 'random inward' scale growing into performed carbides nor any carbon or carbides in either the inward or outward growing scales. We should emphasize, however, that in 'breakaway' oxidation intergranular carbon is frequently found and readily recognized (Newcomb & Stobbs 1985).

(ii) Fe–10Cr–10Ni(α)

Despite the relatively greater n exhibited by this alloy in comparison with its effectively breakaway behaviour in air, the mass gains in CO–CO_2 were very large and the 'non-protective' scales were observed on 'edge-on' specimens oxidized for 125 h. The columnar morphology of the outer growing Fe_3O_4 scale is shown in figure 19*a*, plate 17 and is very similar to that seen on the 9Cr–1Mo alloy while being equally non-porous. Unlike the 9Cr–1Mo alloy, however, the inward growing 100 nm grained M_3O_4 spinel was *also* non-porous. The thickness of this inward growing region of the scale after 125 h was approximately 10 μm and the inner oxide morphology (see figure 19*b*) here is very similar to that seen on the same alloy as oxidized in air. While the grain size was fairly homogeneous with depth a few larger grains were also identified, particularly lower in the scale, where regions of austenite were also again found as presumably transformed from the previously ferritic alloy with the rejection of nickel from the oxidized regions. The region shown in figure 19*c*, for example, exhibits a $(112)_\gamma//(011)M_3O_4$ orientation relation, although elsewhere $(112)_\gamma//(013)M_3O_4$ orientations were also recognized. As in the 9Cr–1Mo alloy no carbides were found in the inward growing scale though again $M_{23}C_6$ carbides were found to a depth of 100 μm beneath the scale. A bright field micrograph of such a region is shown in figure 20*a*, plate 18, where the duplex (α/γ) nature of the alloy is apparent. The orientation relations between the alloy and carbide phases are demonstrated in figure 20*b*. Figures 20*c–f* show dark field micrographs of the area in figure 20*c* as imaged

TABLE 6. SUMMARY OF THE OXIDATION CHARACTERISTICS OF THE Fe–9Cr–1Mo AND Fe–10Cr–Ni ALLOYS OXIDIZED IN 1% CO–CO_2 AT 600 °C

(The data refer to the oxides formed after the times specified.)

alloy	Fe–9Cr–1Mo	Fe–10Cr–10Ni	Fe–10Cr–20Ni	Fe–10Cr–34Ni
alloy microstructure				
pre-oxidation				
XRD	α	α	γ	γ
TEM	α	α	γ	γ
post-oxidation				
TEM	α	α+γ	γ	γ
X-ray diffraction				
lattice parameters/nm				
1500 h. M_3O_4 a_o	0.833	0.834	0.833	0.834
oxidation kinetics 1000 h				
mass gain/(mg cm^{-2})	83.15	200.42	63.16	36.28
n	2.14	1.92	1.15	1.06
10^9 k_p/(g^2 cm^{-4} s^{-1})	1.92	11.2	1.11	0.365
10^9 k_n/(g cm^{-2})^n s^{-1}	1.36	12.7	11.6	8.26
optical metallography				
scale thickness/μm				
125 h	ND	60	6	8.5
1000 h	70	100	60	50
scanning electron microscopy				
surface morphology	hopper (Fe_3O_4)	hopper (Fe_3O_4)	hopper (Fe_3O_4)	hopper (Fe_3O_4)

transmission electron microscopy 125 h																	
oxide identification	$\alpha+M_{23}C_6$	M_3O_4[a]		Fe_3O_4	α+γ	$\alpha+\gamma+M_{23}C_6$	$\gamma+M_3O_4$	M_3O_4	Fe_3O_4	γ	$\gamma+M_3O_4$	M_3O_4	Fe_3O_4	γ	$\gamma+M_3O_4$	M_3O_4	Fe_3O_4
alloy[b]–oxide Fe:Cr:Ni composition (% by mass)																	
Fe	97.5	35	75	95.5						69	32[c]	43	76	94.5	55	28[c]	45	68	91.5
Cr	0.5	64	23	< 3						11	15[c]	54	20	1.5	10	16[c]	38	24	1.5
Ni	—	—	—	—						19	52[c]	3	4	2.5	35	56[c]	7	8	6
oxide thickness/μm		35		35			20	10	30		2	1		3		1	1.5		6
oxide grain size/μm		0.1		4			0.1	0.1	2		0.1	0.1		2		0.1	0.1		2
oxide pores		✓		—			—	—	—		—	—		—		—	—		—

[a] 1000 h.

[b] Data refer to the alloy composition 50 nm from the metal–oxide interface.

[c] Data refer to the composition of M_3O_4.

The broken lines refer to the position of the metal surface before oxidation; the solid lines refer to the positions of inner oxide interfaces.

ND, no determination.

with $(200)_\alpha$, $(220)_\gamma$, and $(220)M_{23}C_6$ reflections respectively. The alloy was also duplex well beneath the area where carbides were formed and such a region is shown in figure 21, plate 19 exhibiting a K–S orientation relation between the two phases (see inset diffraction pattern).

(iii) Fe–10Cr–20Ni(γ)

The thickness of the scale formed on Fe–10Cr–20Ni after 125 h oxidation was found to be *ca.* 6 μm, compared to *ca.* 60 μm for Fe–10Cr–10Ni after a similar period of oxidation. While the mass-gain data might suggest that a thicker scale should have been formed it will be noted that no carbides were formed in this alloy. The form of the duplex oxide identified on the austenitic 10Cr–20Ni alloy is shown in figure 7*b* which indicates that enhanced growth of inner oxide on this alloy characteristically occurs at austenite grain boundaries. Similarly, figure 22, plate 20 shows a bright field TEM montage of a typical region of the duplex scale, where preferential growth of the inner oxide has occurred at a grain boundary in the Fe–10Cr–20Ni alloy. While the thicknesses of the inner and outer scales were generally both *ca.* 3 μm away from grain boundaries, the oxide at the alloy grain boundary extends approximately 13 μm from the duplex oxide interface.

The outer layer of oxide was again, as on the ferritic alloys, shown to be magnetite (94.5% Fe, 1.5% Cr and 2.5% Ni) and exhibited a typically elongated columnar morphology (see figure 22). No pores were identified in the non-grain-boundary regions of the inner or outer oxides. Figure 23, plate 21 shows a region of the upper surface of the outer oxide where we see the hopper morphology in cross section and can note how the cavity, associated with the preferentially outward oxide growth at grain boundaries, does not extend to the original metal surface.

Oxide in the 1 μm region immediately beneath the columnar magnetite layer was comparatively fine grained, with a typical grain size of *ca.* 100 nm, as shown in figure 24, plate 21. EDS analysis of this region of the scale not only indicated that the fine grained spinel contained only minor concentrations of nickel (*ca.* 3%) but that iron was concentrated at the duplex oxide interface where the spinel had a cation composition of 76% Fe, 20% Cr and 4% Ni compared with 43% Fe, 54% Cr and 3% Ni approximately 0.75 μm from this interface.

The morphology and composition of the inward growing oxide was shown to change towards the metal–oxide interface. Unoxidized alloy grains of austenite were, for example, identified surrounded by fine grained spinel and such grains were found to be depleted in both iron and chromium having a typical composition of 28% Fe, 2% Cr and 70% Ni. Coarse grained spinel (*ca.* 250 nm) was identified in other regions of the inner scale with a cation composition of 74% Fe, 22% Cr and 4% Ni. The grain size of this oxide should be compared with the *ca.* 100 nm M_3O_4 grains in the region of the duplex oxide interface, and while similar morphologies were observed on both the ferritic Fe–10Cr–10Ni and austenitic Fe–10Cr–34Ni alloys, we must again note that the fine grained M_3O_4 in the upper parts of the inner scale will eventually encompass such coarser grained regions.

The oxidation zone at the metal–oxide interface, and in the region of preferential growth at the alloy grain bundary, was shown to consist of epitaxially oriented austenite and 'orientated inward' grown spinel, exhibiting no porosity. A 2 μm band of cube–cube orientated metal and oxide was observed sandwiched between the alloy matrix and complex inner oxide discussed above. Figure 25*a*, *b*, plate 22, shows dark field micrographs of the alloy and 25–50 nm fine grained oxide imaged with (220) austenite and spinel reflections respectively. EDS analysis

indicated that the cube–cube orientated oi scale formed in Fe–10Cr–20Ni had an overall cation composition of 32% Fe, 15% Cr and 52% Ni, although the concentrations of these elements were locally variable with the nickel strongly rejected from the oxide into the stabilized austenite. The *average* composition was however similar to that observed in the regions of preferential oxide growth at the alloy grain boundaries. When the behaviour of this alloy is compared with that of Fe–20Cr–20Ni it is particularly interesting that no carbides were found beneath or within the region of oi oxidation as they were in the Fe–20Cr–10Ni alloy, although here too there is no chromium depletion in the subscale alloy matrix.

This alloy was also examined after 1000 h to further explore the temporal development of this type of scale. By this time the scale was found to be about 55 μm in thickness, but the overall form of the microstructure was otherwise unchanged. A region approximately in the middle of the 'orientated inward' scale is, for example, shown in figure 26*a–b*, plate 23, while the metal–oxide interface region is shown in figure 26*d–f*. Note in particular the way the oxide develops initially in the lowest regions of the scale as isolated epitaxial regions of spinel and compare this behaviour with that observed on the same alloy as oxidized in air when the innermost non grain boundary 'random inward' scale was *continuous* and bore no epitaxial orientation relation with the alloy.

(iv) Fe–10Cr–34Ni(γ)

'Edge-on' transmission electron microscopy of the scale formed on this alloy after 125 h indicated that its oxidation behaviour was similar to that observed for the Fe–10Cr–20Ni alloy. Figure 27, plate 24, shows a region of the non-porous outer magnetite of *ca.* 2 μm grain size and approximately 6% Ni content. The relative thickness of the inner oxide compared with the outward growing scale was rather lower than in Fe–10Cr–20Ni, being for this alloy 2.5 μm, but was otherwise of indistinguishable microstructure. The chemical compositions of the different types of region in the 'random inward' scale were however marginally altered (see table 6 and figure 29).

4. Data summary

Given the relatively complicated and diverse processes that occur on the range of alloys investigated summaries of the principal results obtained by all the techniques used as given for air oxidation in table 5 and for oxidation in 1% $CO–CO_2$ in table 6. Equally the schematic diagrams, in figures 28 and 29, of the morphologies of the different scales formed in the two atmospheres are intended as an aid to the recognition of the similarities and differences in the ways by which 'non-protective' oxidation can occur.

Perhaps the major point to note in the examination of this data is that, with the possible exception of Fe–10Cr–10Ni, whose behaviour approaches that normally associated with 'breakaway', all the 'non-protective' inward oxidation behaviours have been demonstrated to be essentially temporally progressive so that a structure seen, at a given time, deeper beneath the scale was earlier higher and will later become more similar to that seen nearer to the outward growing scale. This has major implications since no previous studies of the oxidation of such alloys have considered the detailed temporal change within the inner layer oxide. It has generally been assumed that once oxidation has occurred then the oxide structure does not change. The data also emphasizes how progressive changes in structure and local chemistry can become dominated by instabilities in the relationships between diffusionally limited

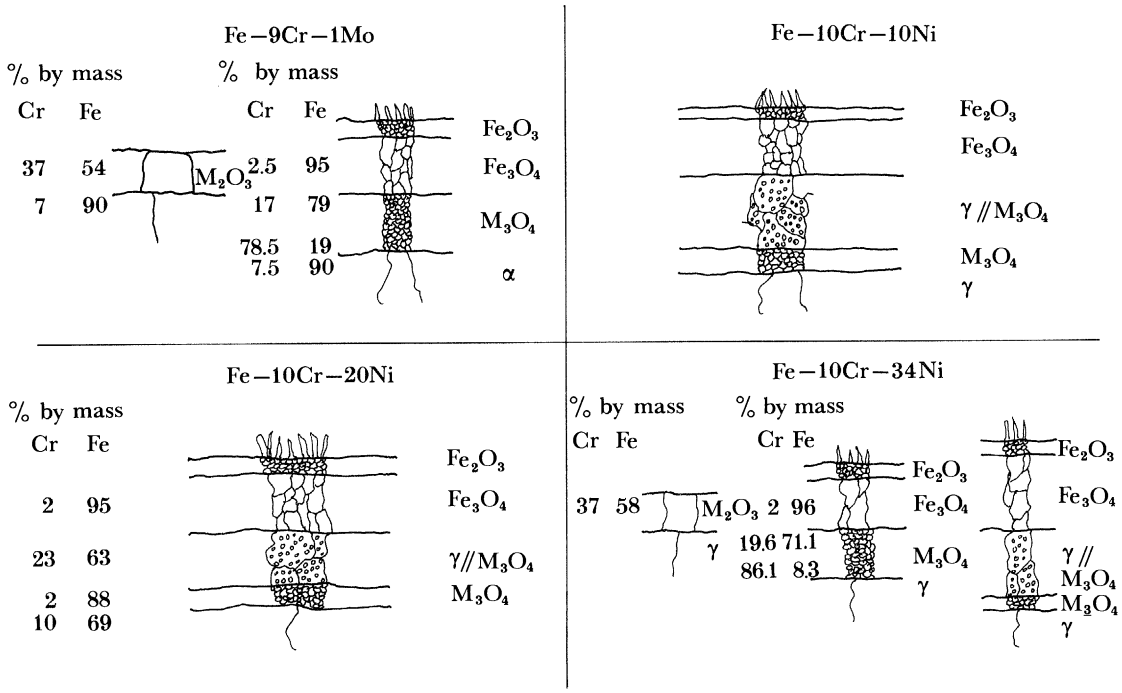

FIGURE 28. Schematic diagrams of the oxides formed on Fe–9Cr and the Fe–10Cr–Ni alloys after oxidation in air for 1000 h at 600 °C.

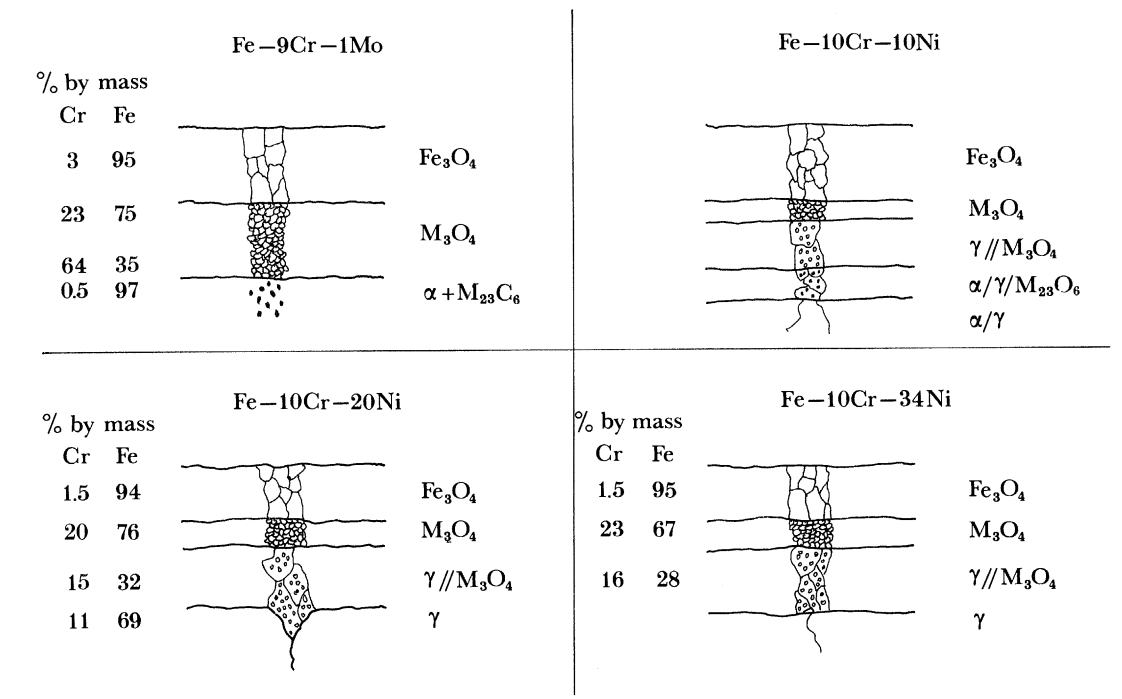

FIGURE 29. Schematic diagrams of the oxides formed on Fe–9Cr and the Fe–10Cr–Ni alloys oxidized in 1 % $CO–CO_2$ at 600 °C.

reactions. The diverse nature of the apparently rate limiting mechanisms of oxidation in the different alloys is discussed in §5.

5. The mechanisms of 'non-protective' scale formation

It will be clear from §4 both that 'non-protective' scaling can occur with a number of different and yet characteristic morphologies and that there is no single mechanism by which the process occurs. Our aim here is thus to point out the trends observed in the scale microstructures and microchemistries, as correlated with the different mass-gain behaviours, so as to delineate the specific mechanisms which are involved. While in some instances we will find that it is important to correlate the data for the 10Cr–Ni alloys with the results obtained for protective oxidation on the 20Cr–Ni alloys (see paper I), we shall concentrate on modelling the 'non-protective' behaviour. In §5*a* we consider the process involved when oxidation occurs in air and in §5*b* we examine the ways in which inward oxidation occurs in an atmosphere of 1% CO–CO_2.

(*a*) *'Non-protective' oxidation in air*

It is first necessary to consider the ways by which alloying elements can become segregated in an oxide and the effect which such segregation can have on the development of a scale. Segregation in duplex scales has been extensively reported. Pfeil (1929) has for example shown that most of the transition elements become concentrated in the inner layer scales of iron alloys oxidized in air at 1000 °C and that the first row transition elements may be placed in order of decreasing cation mobility, Fe:Mn:V:Ni:Cr. These and further results on similar types of segregation (see, for example, Rahmel 1962) are generally accounted for by considering the energetics of cation transfer through the spinel lattice in relation to cation site preference energies. While Azaroff (1961) showed that the preferred diffusion path for a cation in a CCP structure is via alternate adjacent octahedral and tetrahedral interstices, Cox *et al.* (1974) related the diffusivities of different cations to their relative preference energies for the two sites in a spinel. It was predicted that the relative mobilities of the ions below are, in order of decreasing mobility:

trivalent ions: $Fe^{3+}:Ti^{3+}:V^{3+}:Mn^{3+}:Cr^{3+}$;
divalent ions: $Mn^{2+}:Fe^{2+}:Co^{2+}:Cu^{2+}:Ni^{2+}$.

It is thus clear, as was originally suggested some time ago (Cox *et al.* 1972), that chromium will diffuse outward through the magnetite scale only slowly despite the higher activation energy for the oxidation of chromium than iron (see table 8 in paper I). While nickel would also diffuse only very slowly upwards through a spinel scale, the activation energy for the oxidation of nickel is equally comparatively low. In general, it should perhaps be noted that grain boundary diffusivities of all the above elements would be expected to be markedly higher than through single crystals, though at the same time it would not be surprising if the diffusivities for such a process were similarly relatively ranked.

Considering firstly the oxidation behaviour of the 9Cr–1Mo alloy, it is reasonable to assume that the first-formed oxide on this alloy was iron–chromium spinel as was also seen on the Fe–20Cr–Ni alloys (see paper I) and has been reported for Fe–10Cr (Lloyd *et al.* 1977) and Fe–14Cr (Wood & Whittle 1967). A chromium content as low as 3% is needed before the first formed oxide is liable to be Fe_3O_4 (Labun *et al.* 1982). It would thus appear that the first formed spinel on 9Cr–1Mo can either become further oxidized to rapidly establish a thin 'protective'

fine grained α-M_2O_3 scale, or, if presumably the iron content is locally high, a developing region of magnetite. Since iron would diffuse through Fe_3O_4 some 10^8 times faster than through α-M_2O_3 (Hodge 1978) it is not surprising that magnetite can develop outwards with ease, and though the outer regions of this scale will oxidize to Fe_2O_3, the open blade and whisker morphology of this latter oxide will not prevent the ingress of oxygen to the Fe_2O_3–Fe_3O_4 interface. The outward development of the magnetite by the upward diffusion of iron thus encourages the further *inward* growth of the initially formed fine grained spinel with progressively increasing chromium content through the interchange of iron and chromium (as energetically favoured) in the oxide at the alloy-oxide interface. The developing fine grained morphology of the 'random inward' oxide beneath the original metal surface is not, however, consistent with the process being by cationic exchange alone and it would appear that inward oxidation is almost certainly occurring as well through the inward diffusion of oxygen. There is also considerable indirect evidence for this as derives, for example, from a consideration of the form of the inward growing scales on the alloys with high Ni content. The depletion of chromium in the ferritic alloy beneath the inward growing scale suggests that the upward diffusion of chromium in the alloy is slow and we argued in paper I that it is potentially the progressive decrease in chromium content at the metal–oxide interface of a '*protective*' scale which can lead to cube law ($n = 3$) kinetics. A similar value of n is found for Fe–9Cr–1Mo as oxidized in air though now the rate constant is considerably larger, presumably because the diffusion of Fe through a spinel is so much easier than through α-M_2O_3. The other similarities in the way that, in particular, Fe–20Cr–2Ni oxidizes in CO–CO_2 have already been alluded to in §3*a* but it should be noted that under different circumstances a power law of $n = 3$ can yield either a 'protective' or a 'non-protective' scaling behaviour. Overall in the alloys considered, the diversity of the processes seen simultaneously makes a mechanistic development based on the power-law behaviour alone unlikely to be beneficial.

Considering the inward oxidation behaviour of Fe–10Cr–10Ni it is very clear that this occurs principally through the inward motion of oxygen. Given the oxidation power law for the material this is hardly surprising since the oxidation could be argued to be essentially 'breakaway'. There are however similarities in the development of the innermost layer 'random inward' spinel grains and 'orientated inward' oxide above this, with the development of inward scaling on the 20 and 34Ni alloys. This would suggest that similar inward diffusional movement of oxygen is occurring in all three materials.

The particularly intriguing and characteristic feature of the inward growing scale on the Fe–10Cr–20Ni and of one of the 'non-protective' scales on Fe–10Cr–34Ni is the form of the innermost fine grained and continuous RI spinel layer *beneath* OI oxide. The points which should be noted include: (*a*) the layer is better developed in the 34Ni alloy than in that containing 20% Ni; (*b*) the austenite above this continuous layer in the OI oxidation region is at an identical orientation to that in the subscale alloy and (*c*) while there is no depletion of chromium or nickel beneath the layer, the average nickel content above the layer in the OI oxidation zone is well above that of the bulk alloy.

This innermost spinel layer has the essential appearance of the first formed, but subsequently inward developing, spinel layer as seen in Fe–9Cr–1Mo but there remaining in contact with the outward growing magnetite scale. Now, however, it is displaced down into the alloy and the above phenomenological characterization points to the mechanism involved being cationic exchange. Under these circumstances, the driving force for the downward motion of the oxide

layer would be the exchange of chromium or iron ions at its front face for nickel ions above it. This process coupled with limited upward diffusion of nickel would naturally lead, for example, to the enrichment of the layer in chromium and to an increasing nickel concentration in the OI oxidation zone, while the downward drifting inner scale becomes nickel depleted. The maintained austenite orientation across a 'random inward' scale would be explained if the original downward motion was not uniform, so that a region of the original austenite grain could become trapped above a finally continuous layer. In fact, while the layer, as examined in Fe–10Cr–20Ni, is depleted in nickel and enriched in iron it is *depleted* in chromium with a cationic composition of 88% Fe, 2% Cr and 10% Ni. In just the same way the 'random inward' oxide formed on the alloy of highest nickel content, Fe–10Cr–34Ni, was similarly depleted in nickel (15%) but also in chromium (6%) relative to the undepleted and underlying metal. The chromium depletion is not consistent with the mechanism proposed unless cationic exchange with the adjacent 'oriented inward' oxide immediately above the 'random inward' oxide, with ready diffusion in the associated austenite, is leading to immediate and easy redistribution of the chromium into this OI oxide. Certainly the chromium content of the OI oxide is high at about 23% in the 10Cr–20Ni alloy. It is also true that if the chromium content could be kept low in the innermost layer, as it is, then its associated ion diffusivities would be enhanced. That the 'orientated inward' oxide behind this layer remains in contact with it, in both Fe–10Cr–20Ni and Fe–10Cr–34Ni, suggests that it is the diffusion of this layer which could well be the rate determining process in the oxidation reaction. It should be remembered that both alloys obey parabolic mass-gain laws and exhibit *no* chromium depletion beneath the inner oxide (cf. Fe–9Cr–1Mo with $n = 3.25$ and subscale chromium depletion). Whatever is the rate controlling diffusional process, it is difficult to imagine any other mechanism by which the 'random inward' oxide layer would be continuous and yet lie beneath unoxidized alloy.

The dissimilarity in the chromium content of this inner moving scale, by comparison with the *increased* chromium content of the inward growing fine grained spinel which remains in contact with outward growing scales should be emphasized. Equally it is clear that the OI oxidation process in the intervening region necessarily requires the inward diffusion of oxygen. The formation of an 'orientated inward' oxide consisting of austenite and spinel means that a high outward flux of cations can be maintained towards the outward growing scale by the diffusion of iron and chromium through the austenite rather than the spinel. A similar process could be involved in maintaining a high iron flux to the outward growing scale in the Fe–10Cr–10Ni alloy since in this alloy the OI oxidation zone contained austenite of high diffusivity by comparison with that for a fully oxidized spinel interface region beneath the outer scale, which in this case is again not present.

Overall, comparing all the different inward growing scales formed on these materials it is clear that oxygen must be able to diffuse readily through M_3O_4 of low chromium content. Note, for example, that when the 'random inward' scale drifts into the alloy by cationic exchange, there is a sufficient supply of anions to oxidize the material above this RI scale but beneath the outward growing magnetite. Considering, however, the relatively limited inward development of the fine grained spinel on Fe–10Cr–34Ni, when this spinel remains in contact with the outward growing magnetite by comparison with the situation when it moves downwards by cationic exchange, it is equally clear that oxygen diffuses only slowly through even a fine grained spinel containing chromium. This is perhaps because chromium is so much more readily oxidized than iron with the result that diffusion pathways for the anions might be blocked by

chemical interaction. EELS analysis of the oxygen levels at different depths in the mixed cation spinel is however currently of insufficient sensitivity to detect the changes in the anion content with depth which might be expected on the above argument.

In conclusion we should emphasize that we suggest that local chemical instabilities in the Fe:Cr ratio at the base of an initially formed scale can lead to it developing very differently in different regions of the same alloy as is particularly exemplified by the behaviour of Fe–10Cr–34Ni. Furthermore any arguments on the oxidation rate limiting process based on mass gain data are of extremely limited value when the oxidation can proceed by such diverse modes in different areas. The qualitative use which is made of such data here and in paper I is limited either to the comparison of scales which develop relatively homogeneously or to situations in which the most 'non-protective' mode of oxidation is so extensive (either laterally or in depth) that it will account for the major fraction of the mass gains recorded.

(*b*) '*Non-protective*' *oxidation in* 1 % $CO–CO_2$

We should note first that thicker scales grow in the low oxygen potential environment of 1 % $CO–CO_2$ than in air with, excluding Fe–10Cr–10Ni, smaller n. However, the reduction in oxygen potential would be expected to suppress the formation of an iron rich scale and favour the selective oxidation of chromium. The oxidation of iron occurs by the transport of iron through vacancies and has a diffusion coefficient proportional to $p_{O_2}^{\frac{2}{3}}$ (Kofstad 1972). The rate of scale thickening for a p-type oxide, such as magnetite, for which cation vacancies are the transport species is given by: $\mathrm{d}x/\mathrm{d}t = Ap_{O_2}^{1/n} Dv/x.$

However, the oxidation rate of an n-type oxide, for which cation interstitials are the transport species, may be expressed as: $\mathrm{d}x/\mathrm{d}t = Bp_{O_2}^{-1/n} Di/x.$

In this case, p_{O_2} represents the partial pressure of oxygen at the metal–oxide interface so that the rate of oxidation is independent of the external gas pressure.

Dieckmann & Schmalzried (1977) have shown that between 900 and 1400 °C the oxygen partial-pressure dependence of the tracer diffusion coefficient of Fe^{59} in single crystal magnetite changes from being proportional to $p_{O_2}^{\frac{2}{3}}$ to being proportional to $p_{O_2}^{-\frac{2}{3}}$ as the oxygen partial pressure is reduced. They concluded that the dominant diffusion mechanism changes from a vacancy mechanism to one involving the diffusion of interstitial ions, as the oxygen pressure is reduced. M. I. Manning (personal communication 1982) has extrapolated the data to show that the change in p_{O_2} dependence from $\frac{2}{3}$ to $-\frac{2}{3}$ occurs at 10^{-24} atm† at 500 °C. The p_{O_2} of the 1 % $CO–CO_2$ atm used in this study at 600 °C was 1.8×10^{21} atm. The oxidation rate should therefore be proportional to $p_{O_2}^{-\frac{2}{3}}$, and an interstitial diffusion process may be assumed to be dominant. Accordingly, the oxidation of iron should be independent of the external gas pressure when oxidation is carried out in 1 % $CO–CO_2$. The formation of p-type chromium oxide in both environments, however, may be assumed to be dependent on the partial pressure of oxygen.

The mechanism for the growth of two-layer oxides in carbon dioxide would appear to be well established (see, for example, Harrison *et al.* 1974; Antill *et al.* 1968; Gibbs 1973). A number of workers have used essentially standard methods to show that the outer magnetite and inner spinel maintain equal thickness (see, for example, Pritchard & Truswell 1974) as the scale develops, the inner spinel growing in the volume made available by the departing metal (Gibbs

† 1 atm = 101 325 Pa.

et al. 1974) while the magnetite develops at the gas interface (Gibbs 1973). The rate-controlling process has been demonstrated generally to be the outward diffusion of iron across microporous inner oxide layers (Surman 1973). Conventional models further require the inward movement of CO_2 within the oxide to the metal–oxide interface to produce the spinel layer (Gibbs 1973). That CO_2 enters the alloy via pores has equally been generally assumed on the basis of the hopper morphology of the outer oxide and the fact that the carbon content both of the alloy and of the scale (see, for example, Leach *et al.* 1974) can increase.

While such a process undoubtedly occurs during 'breakaway' oxidation, the characteristic feature of all the oxide scales investigated here, as formed in 1% CO–CO_2, is that when continuous they never contain carbon. Of the alloys examined here the 'random inward' (but not the outer) scale on Fe–9Cr–1Mo was microporous but neither scale on Fe–10Cr–10Ni contained any pores larger than about 0.5 nm (the limit of detectability of such a pore, when examined by using enhanced Fresnel contrast). Both these alloys developed carbides beneath their outward and inward growing scales. Still more interestingly, the outward growing magnetite and inward growing spinel scales on both Fe–10Cr–20Ni and Fe–10Cr–34Ni similarly contained no pores (as well as no carbon) but both developed an extensive OI oxide beneath the continuous fine grained spinel immediately under the outward growing Fe_3O_4. Furthermore it will be remembered that the Fe–20Cr–20Ni and Fe–20Cr–34Ni both exhibited non-porous chromium oxide scales but still developed a carbide distribution in the austenite beneath them (see paper I).

Clearly it is necessary to assume that at least CO, and almost certainly CO_2, can gain ingress to the alloy through the grain boundaries of either a magnetite spinel or chromium oxide scale. It will be remembered that the diffusivity of oxygen in chromium oxide is generally considered to be negligible (Howes 1970) although at least slight inward development of the scales on 20Cr–Ni alloys oxidized in air was observed. Even so it is still necessary to understand how, as a function of chromium content, either inward oxidation or carburization might then occur to the exclusion of the alternative process except in Fe–10Cr–10Ni. A three-way comparison of the different types of scales which form on Fe–10Cr–34Ni in air and in CO–CO_2, and on Fe–20Cr–34Ni in the latter atmosphere, is helpful in delineating the types of mechanism which must be involved. Fe–20Cr–34Ni oxidizes in CO–CO_2 in a way which was defined as 'protectively' to form a fine grained non-porous Cr_2O_3 scale with depletion of chromium beneath this in the alloy and extensive subscale carburization (see paper I). Comparing now the Fe–10Cr–34Ni alloy's most 'non-protective' mode of scaling behaviour in air and in CO–CO_2 we see that the outward development of Fe_3O_4 is a common feature (although this is, of course, oxidized to Fe_2O_3 at the air–oxide interface) as is the inward growth and development of M_3O_4 in OI form. The essential difference between the two types of inward growing scales is that whereas in CO–CO_2 the RO continuous fine grained spinel zone remains in contact with the outward growing magnetite, in air this band can remain in contact with the subscale alloy drifting downwards by, as discussed above, a mechanism which would appear to be cationic exchange, nickel being concentrated above it. That OI oxide forms in the Fe–10Cr–34Ni alloy in both air and CO–CO_2 without any internal deposition of carbides in the alloy or beneath the scale points strongly to the oxidizing species for this part of the process being in *both* cases *oxygen*. Examination of the relative exothermic and endothermic natures of the potential reactions which could occur when CO_2 comes in contact with an Fe–Cr alloy it may be noted from table 8 of paper I that as 600 °C:

$$2CO_2 \rightarrow \underset{\substack{\downarrow \\ (2)\text{ or }(3)}}{2CO} + \underset{\substack{\downarrow \\ (4)\text{ and }(5)\text{ or }(6)}}{O_2} : +90\text{ kcal}\dagger; \quad (1)$$

$$\tfrac{2}{3}Cr + CO \rightarrow \tfrac{1}{3}Cr_2O_3 + \underset{\substack{\downarrow \\ (4) \\ \uparrow}}{C} : -60\text{ kcal}; \quad (2)$$

$$\tfrac{3}{4}Fe + CO \rightarrow \tfrac{1}{4}Fe_3O_4 + C : -40\text{ kcal}; \quad (3)$$

$$O + C \rightarrow CO : -40\text{ kcal}; \quad (4)$$

$$\tfrac{3}{4}Fe + O \rightarrow \tfrac{1}{4}Fe_3O_4 : -50\text{ kcal}; \quad (5)$$

$$\tfrac{2}{3}Cr + O \rightarrow \tfrac{1}{3}Cr_2O_3 : -100\text{ kcal}. \quad (6)$$

This combination of reactions would lead to a build up of CO but not C at the interface between the inward oxidizing spinel and the alloy. Assuming simplistically that (5) and (6) occur in the proportion 1:2 the total reaction would appear to be exothermic for the original two molecules of CO_2. While such a process would not thus appear to be impossible the competitive reaction of CO_2 with chromium should be examined:

$$\tfrac{8}{3}Cr + 2CO_2 \rightarrow \tfrac{4}{3}Cr_2O_3 + 2C : -240\text{ kcal} \quad (7)$$

so that it would appear that the latter type of reaction with inward chromium oxide formation and the deposition of carbon is to be preferred. This indeed would appear to be the dominant process in the alloys of higher chromium content. That it is self evidently not the main reaction in the Fe–10Cr–Ni alloys, at least when the nickel content is 20% or above, points both to the relative difficulty with which chromium is oxidized in CO–CO_2 and equally provides further indirect evidence that the development of the 'orientated inward' scale involves not only cationic exchange, to alloy upward motion of iron towards the magnetite, but also direct inward internal oxidation. It will be noted that the process involved in the combination of reactions (1)–(5) involves a build up of chromium rich spinel and CO at an inward growing fine grained spinel interface with the alloy. Given that CO_2 can gain ingress to this region, despite the lack of porosity of the outer scale, presumably means that the smaller CO molecules should have little difficulty in moving back out of the scale once the concentration has risen sufficiently. Interestingly this would suggest that if the external CO concentration be increased there would be a greater tendency to spallation and 'breakaway' behaviour as is observed (Surman & Brown 1974). Equally it might be predicted that in pure CO_2 the reaction, as seen on Fe–10Cr–34Ni would proceed more readily.

Further examination of the combination of (1)–(6) reveals that, as the chromium activity is increased, as it would be as the nickel content is lowered, (6) is promoted over (5) with an increasing net exothermicity and that the deposition of carbon is encouraged by the increasing dominance of (2) and cessation of (4). This tendency is consistent with the trends seen on moving from Fe–10Cr–34Ni to Fe–10Cr–10Ni and finally to Fe–9Cr–1Mo which could be considered to further establish the nature of the mechanism for the formation of M_3O_4, as a 'random inward' oxide on this latter alloy, as being only to a limited extent through cationic exchange.

† 1 cal = 4.184 J.

Further evidence for CO–CO_2 oxidation of in particular, the Fe–10Cr–20Ni and 34Ni alloys occurring in the general way described is obtained by examination of the relative chromium and iron concentrations at the top and bottom of the fine grained spinel layer in each alloy. In Fe–10Cr–20Ni the cationic ratios of Cr, Fe and Ni are 20:76:4 at the top of this layer and 54:43:3 at the bottom, compared with values of 24:68:8 and 38:45:7 respectively in the 34Cr alloy. There is thus a lower initial and yet higher final chromium content on the lower by comparison with the higher nickel alloys. This points to the initially higher Fe activity and yet finally lower chromium activity as in both alloys this element is enriched beneath the scale.

The remaining surprise in the 'non-protective' oxidation of the 20 and 34Ni alloys is that this can occur with nearly linear kinetics, while similar 'orientated inward' scales form in air with roughly parabolic kinetics. The first point indicates that despite the lack of porosity of both the outward growing magnetite and inward growing spinel, CO_2 can gain ingress easily. However this might be occurring we can further see, by comparison of the respective scales, that the parabolic nature of the scaling of the alloys in air must be associated with the novel process suggested for the downward movement of the 'inner' finer grained spinel. Since this layer should not become thicker as it moves, the $n = 2$ behaviour might be related to what would be a decreasing value of its chromium content together with an increasing nickel content above it. We have argued that a similarly concentration change related increase in n for the oxidation behaviour of the 20Cr–Ni alloys in air where, the diffusion of the cations through the M_2O_3 scale (as distinct from M_3O_4) is apparently parabolically controlled for a given subscale concentration. Further evidence for the way pores would appear to be immaterial for the 'non-protective' inward oxidation of this type of alloy is obtained when it is remembered that the inward growing 'random inward' spinel which forms on Fe–9Cr–1Mo is particularly porous and yet this alloy oxidizes with roughly *cube* law kinetics. For this latter alloy we see the combined effect of the fact that the inward oxidation occurs below the spinel–alloy interface with the fact that there is a resultantly more rapid depletion in chromium content than in the 10Cr–20Ni or 10Cr–34Ni alloys where the primary reaction can take place above the position where inward oxidation has already occurred so that the relevant chromium activity level decrease is then, in an associated way, less rapid.

6. Conclusions

We believe that we have identified the important rate limiting aspects of the different scaling behaviours described although we have not attempted to develop mathematically the diffusional behaviour of the broadly described models which we have identified. This will be completed elsewhere.

We shall not restate the large number of different processes which we have described, either here or in paper I, but certain general conclusions merit attention. For example it would appear that: (*a*) inward oxidation is more common than is generally recognized; (*b*) inward motion of oxidizing species through a scale is generally more easy than has hitherto been thought and not dependent on the presence of connected porosity (though this is what is required, as we recognize, for the onset of 'breakaway'); (*c*) the type of process involved in oxidation can be different on different parts of the same alloy at a given time and can also change as a function of time; (*d*) the power law for mass gain data is, of itself, an extremely model insensitive parameter not only because totally different processes can often occur as a result of chemical

instabilities side by side but also because, as we have shown, very different processes can yield similar power laws; (*e*) cationic exchange can lead not only to the upward motion of a given cation but also to the bodily movement of a scale downwards into the subscale alloy ahead of unoxidized alloy. This process is particularly interesting in that it points to a fundamental mechanism by means of which *passivation* might be achieved by the promotion of a form of 'non-protective' oxidation of this type: the interface regions beneath an outward growing scale but above the downward moving scale being thereby potentially enrichable with an element of low oxidation potential; (*f*) this of itself points to a limitation in the appropriateness of the terms 'protective' and 'non-protective', as used to entitle the behaviours described respectively in paper I and here. Furthermore, it would appear to be a fundamentally characteristic aspect of the oxidation of alloys of the type described here that chemical instabilities can arise in such a way that both 'protective' and 'non-protective' processes can occur simultaneously and side by side. It will be apparent that it is only by the full comparison of ranges of alloys, as a function of both nickel and chromium content, that we can come to understand the general importance of the way changes in structure and local chemistry can become dominated by instabilities in the relationship between competing diffusion limited reactions. The high model sensitivity of the microstructures seen historically as formed in the scales, and the usefulness of the phenomenological set of definitions for the different types of processes are then clear. It is the combination in approach which has allowed us to delineate the important processes in most of the different types of scaling process we have described.

We thank Professor R. W. K. Honeycombe, F.R.S., for the provision of laboratory facilities; we acknowledge the partial support of both the SERC and CERL (Leatherhead). This paper is published by permission of the Central Electricity Generating Board.

References

Allan, S. J., Norton, J. F. & Popple, L. A. 1974 In *Proceedings of BNES international conference on corrosion of steels in* CO_2 (ed. D. R. Holmes, R. B. Hill & L. M. Wyatt), pp. 284–297.

Antill, J. E., Peakall, K. A. & Warburton, J. B. 1968 *Corros. Sci.* **8**, 689–701.

Azaroff, L. V. 1961 *J. appl. Phys.* **32**, 1658–1662.

Boggs, W. E., Kachik, R. H. & Pellissier, G. E. 1967 *J. electrochem. Soc.* **114**, 32–39.

Cox, M. G. C., McEnaney, B. & Scott, V. D. 1972 *Phil. Mag.* **26**, 839–851.

Cox, M. G. C., McEnaney, B. & Scott, V. D. 1974 *Phil. Mag.* **29**, 585–600.

Dieckmann, R. & Schmalzried, S. 1977 *Ber. BunsenGes. phys. Chem.* **81**, 414–419.

Gibbs, G. B. 1973 *Oxidat. Metals* **7**, 173–184.

Gibbs, G. B., Pendlebury, R. E. & Wootton, M. R. 1974 In *Proceedings of BNES international conference on corrosion of steels in* CO_2 (ed. D. R. Holmes, R. B. Hill & L. M. Wyatt), pp. 59–72.

Harrison, P. L., Dooley, R. B., Lister, J. K., Meadowcroft, D. B., Nolan, P. J., Pendlebury, R. E., Surman, P. L. & Wootton, M. R. 1974 In *Proceedings of BNES international conference on corrosion of steels in* CO_2 (ed. D. R. Holmes, R. B. Hill & L. M. Wyatt), pp. 220–233.

Harrison, P. L. 1976 *CEGB Report* no. RD/LIR/933.

Holmes, D. R., Mortimer, D. & Newell, J. E. 1974 In *Proceedings of BNES international conference on corrosion of steels in* CO_2 (ed. D. R. Holmes, R. B. Hill & L. M. Wyatt), pp. 151–164.

Hodge, J. D. 1978 *J. electrochem. Soc.* **125**, 55–57.

Howes, V. R. 1970 *Corros. Sci.* **10**, 99–103.

Kofstad, P. 1966 *High temperature oxidation of metals*, p. 88. New York: Wiley–Interscience.

Kofstad, P. 1972 *Non-stoichiometry, diffusion and electrical conductivity in binary metal oxides*, p. 232. New York: Wiley–Interscience.

Labun, P., Covington, J., Kuroda, K., Welsch, G. & Mitchell, T. E. 1982 *Met. Trans.* (A) **13**, 2103–2112.

Leach, J. S. L., Nehru, A. Y., Taylor, D. E. & Taylor, M. F. 1974 In *Proceedings of BNES international conference on corrosion of steels in* CO_2 (ed. D. R. Holmes, R. B. Hill & L. M. Wyatt), pp. 97–108.

Lloyd, G. O., Saunders, S. R. J., Kent, B. & Fursey, A. 1977 *Corros. Sci.* **17**, 269–299.
Metcalfe, E. 1979 *CEGB Report* no. RD/L/N80/79.
Newcomb, S. B. 1983 *Ph.D. thesis*, University of Cambridge.
Newcomb, S. B., Smith, D. J. & Stobbs, W. M. 1983 *J. Microsc.* **130**, 137–146.
Newcomb, S. B., Stobbs, W. M. & Metcalfe, E. 1986 *Phil. Trans. R. Soc. Lond.* A **319**, 191–218.
Newcomb, S. B. & Stobbs, W. M. 1985 *J. Microsc.* **140**, 209–220.
Pfeil, A. B. 1929 *J. Iron Steel Inst.* **119**, 501–547.
Pritchard, A. M. & Truswell, A. E. 1974 In *Proceedings of BNES international conference on corrosion of steels in* CO_2 (ed. D. R. Holmes, R. B. Hill & L. M. Wyatt), pp. 234–246.
Rahmel, A. 1962 *Z. Elecktrochem.* **66**, 363–369.
Rowlands, P. C. & Manning, M. I. 1981 In *Proceedings of 6th NACE international conference on high temperature corrosion* (ed. R. A. Rapp), pp. 300–309. Texas: National Association of Corrosion Engineers.
Surman, P. L. 1973 *Corros. Sci.* **13**, 825–832.
Surman, P. L. & Brown, A. M. 1974 In *Proceedings of BNES international conference on corrosion of steels in* CO_2 (ed. D. R. Holmes, R. B. Hill & L. M. Wyatt), pp. 85–96.
Tallman, G. R. & Gulbransen, E. A. 1968 *Nature, Lond.* **218**, 1046–1047.
Wood, G. C. & Hodgkiess, T. 1966 *J. electrochem. Soc.* **113**, 319–327.
Wood, G. C. & Whittle, D. P. 1967 *Corros. Sci.* **7**, 763–782.

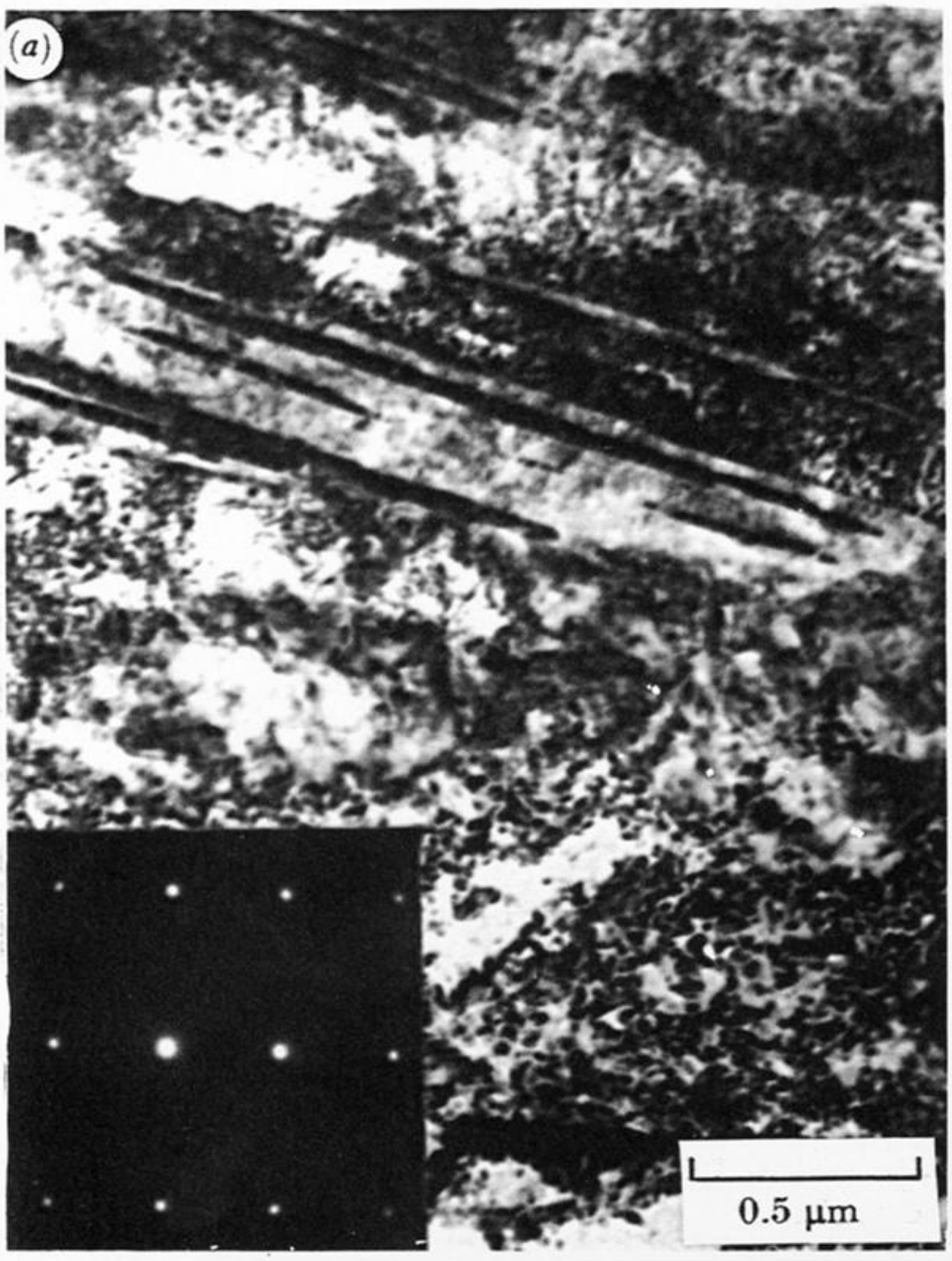

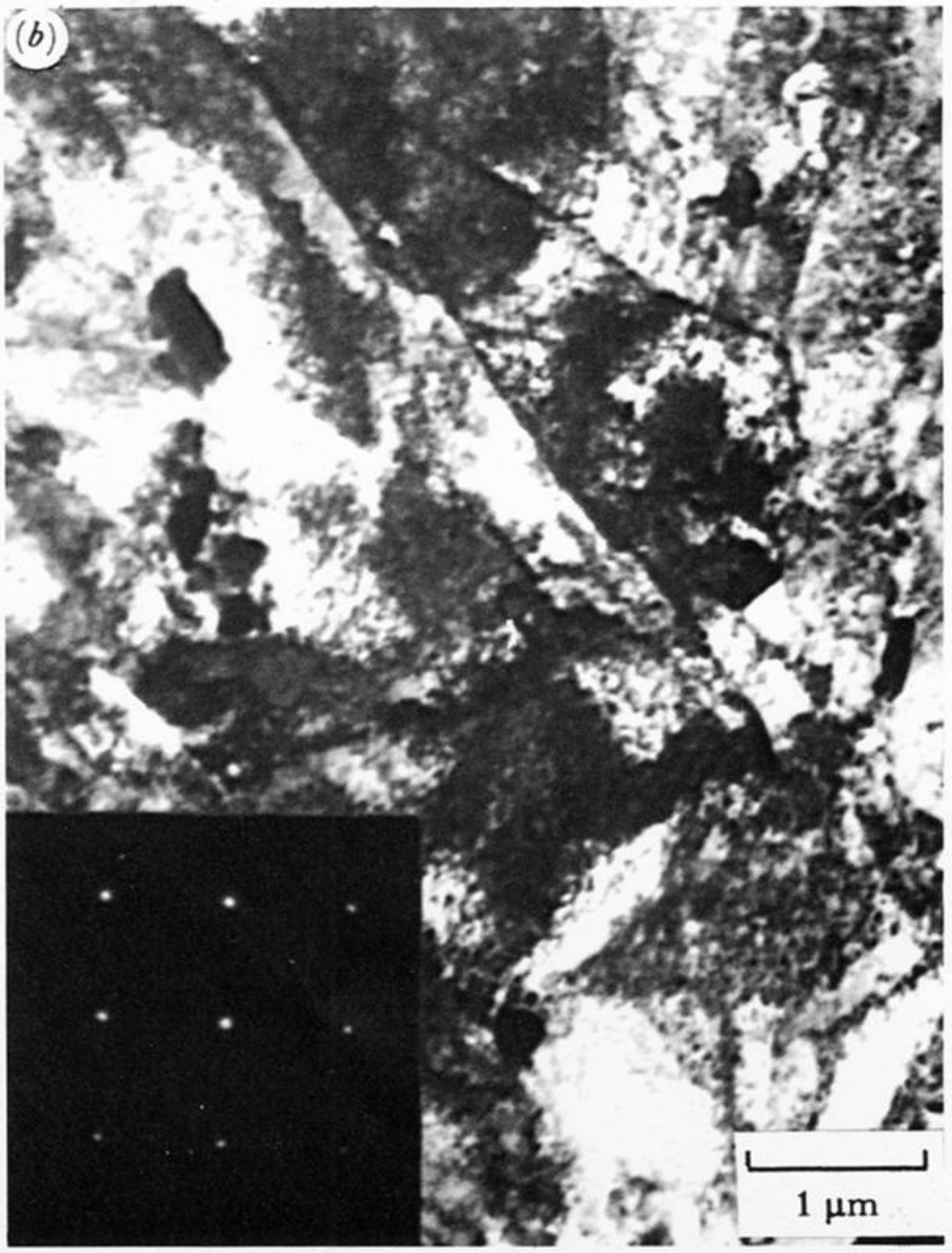

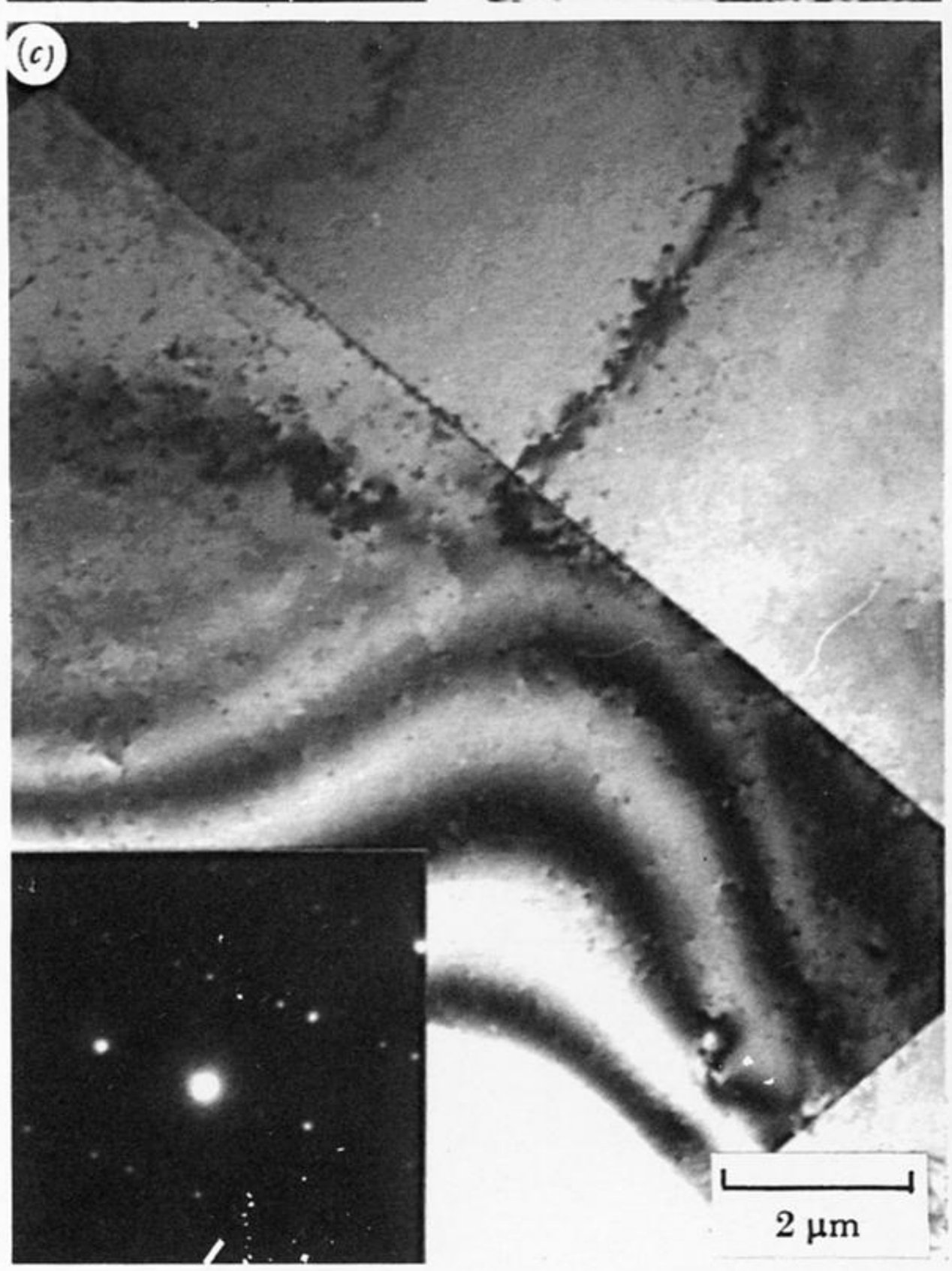

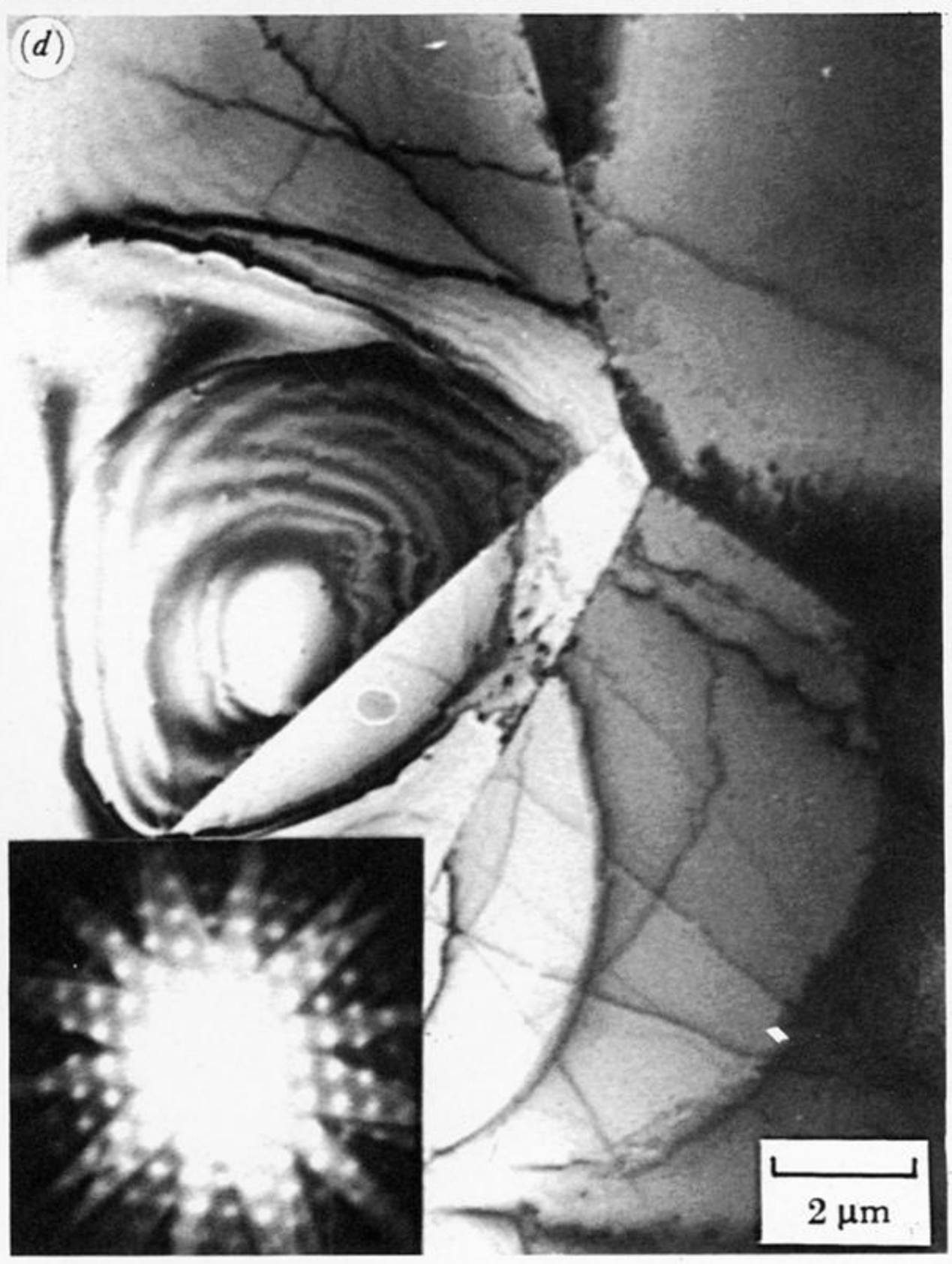

FIGURE 1. Microstructures of the alloys prior to oxidation. Bright field TEM. Diffraction patterns for each alloy are shown in the insets. (*a*) Fe–9Cr–1Mo: diffraction plane: $(011)_\alpha$; (*b*) Fe–10Cr–10Ni: diffraction plane: $(001)_\alpha$; (*c*) Fe–10Cr– 20Ni: diffraction plane: $(011)_\gamma$; (*d*) Fe–10Cr–34Ni: diffraction plane: $(011)_\gamma$.

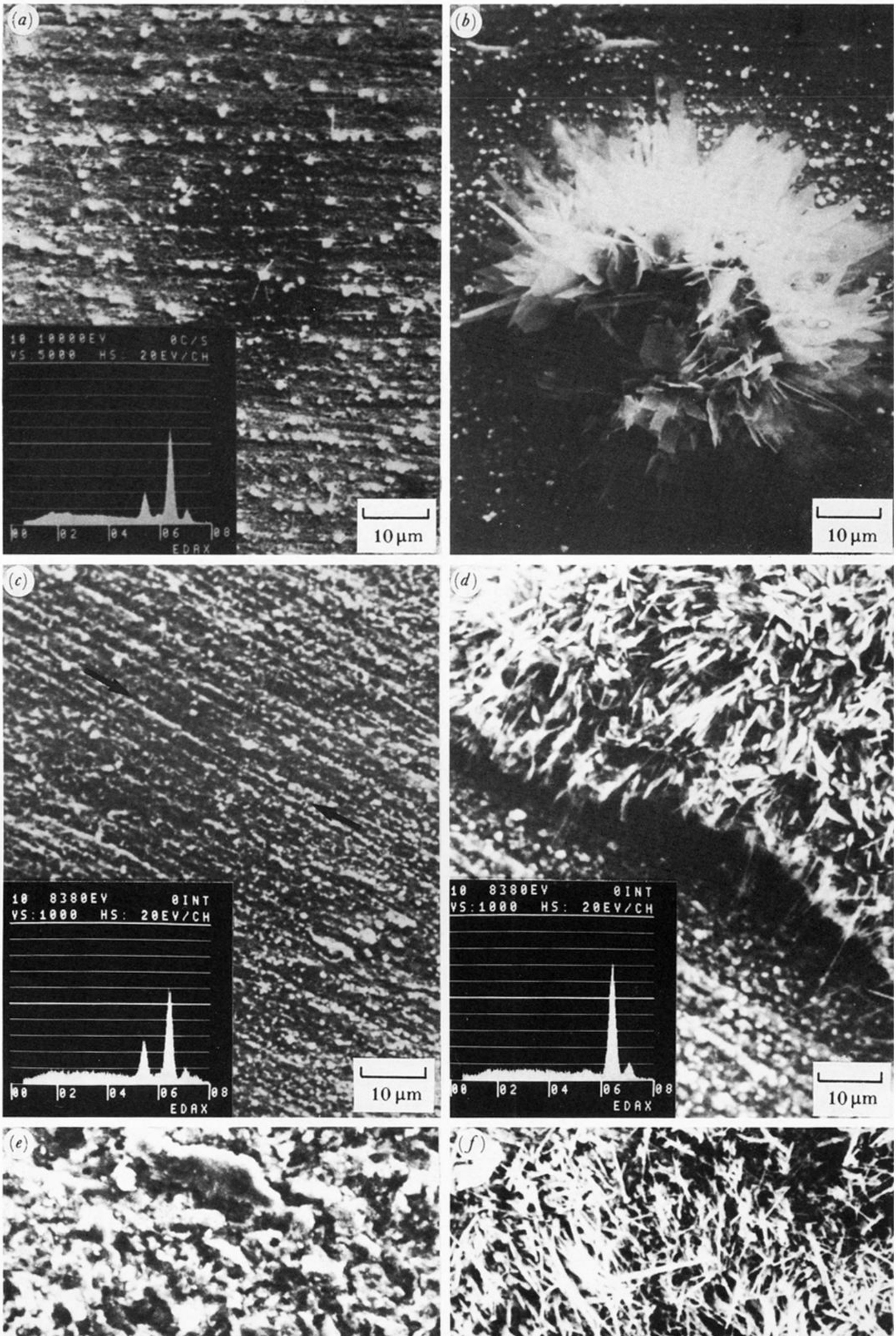

FIGURE 3. Scanning electron micrographs and 20 kV EDS analyses (Cr:5.411, Fe:6.398, Ni:7.41 keV) of the surfaces of the oxides formed in air after 1000 h oxidation at 600 °C. (*a*) Fe–9Cr–1Mo: 'protective' scale; (*b*) Fe–9Cr–1Mo: 'non-protective' nodule; (*c*) Fe–10Cr–10Ni: 'protective' scale; scratches on the surface of the alloy are arrowed; (*d*) Fe–10Cr–10Ni: 'non-protective' region adjacent to a 'protective' scale; (*e*) Fe–10Cr–20Ni: original M_3O_4–Fe_3O_4 interface, the upper oxides having spalled; (*f*) Fe–10Cr–34Ni: outermost haematite scale.

FIGURE 4. Scanning electron micrograph and 20 kV EDS analysis (Fe: 6.398 keV) of the surface of the scale formed on Fe–10Cr–10Ni in 1 % CO–CO_2 after 1000 h at 600 °C.

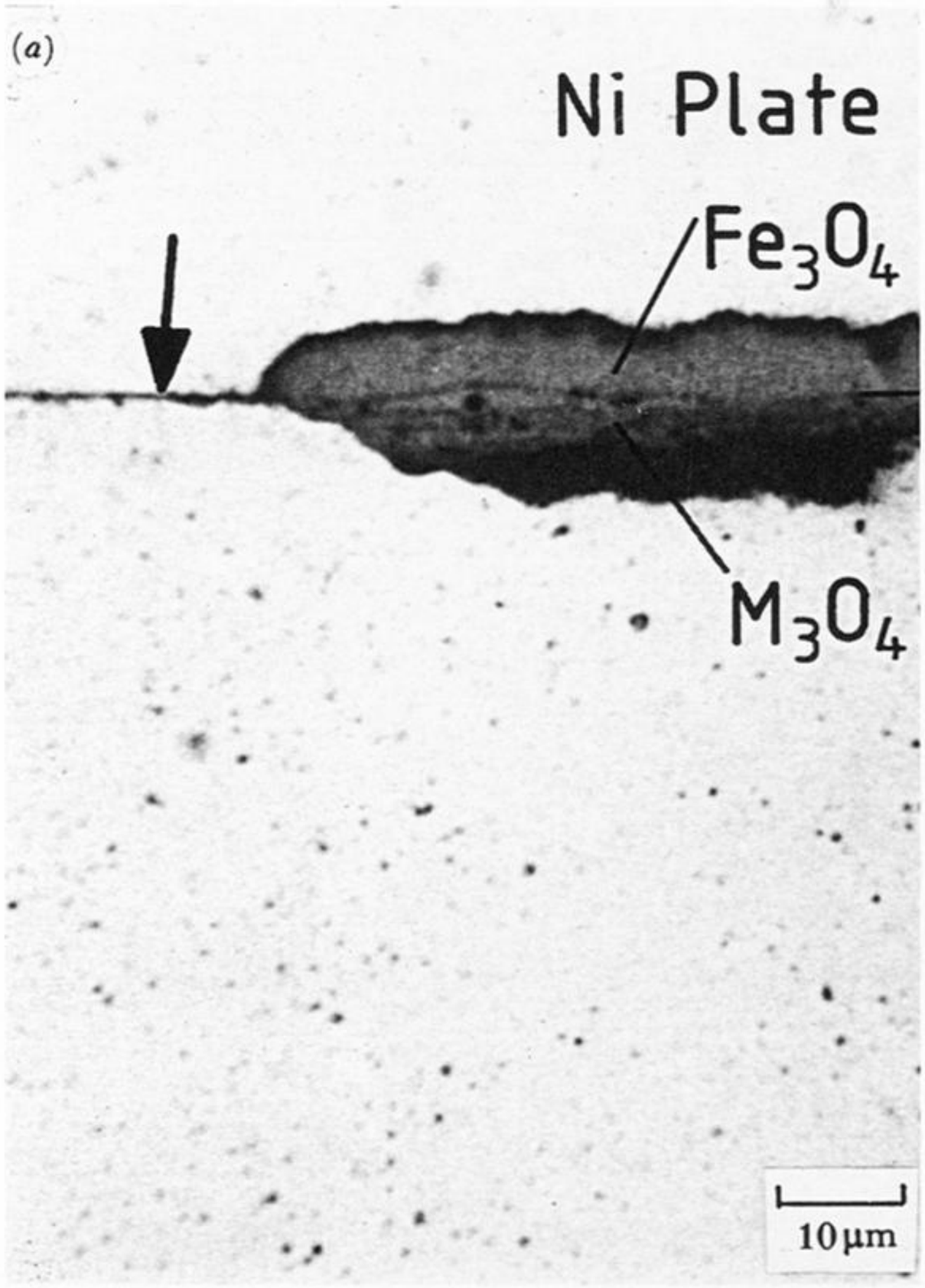

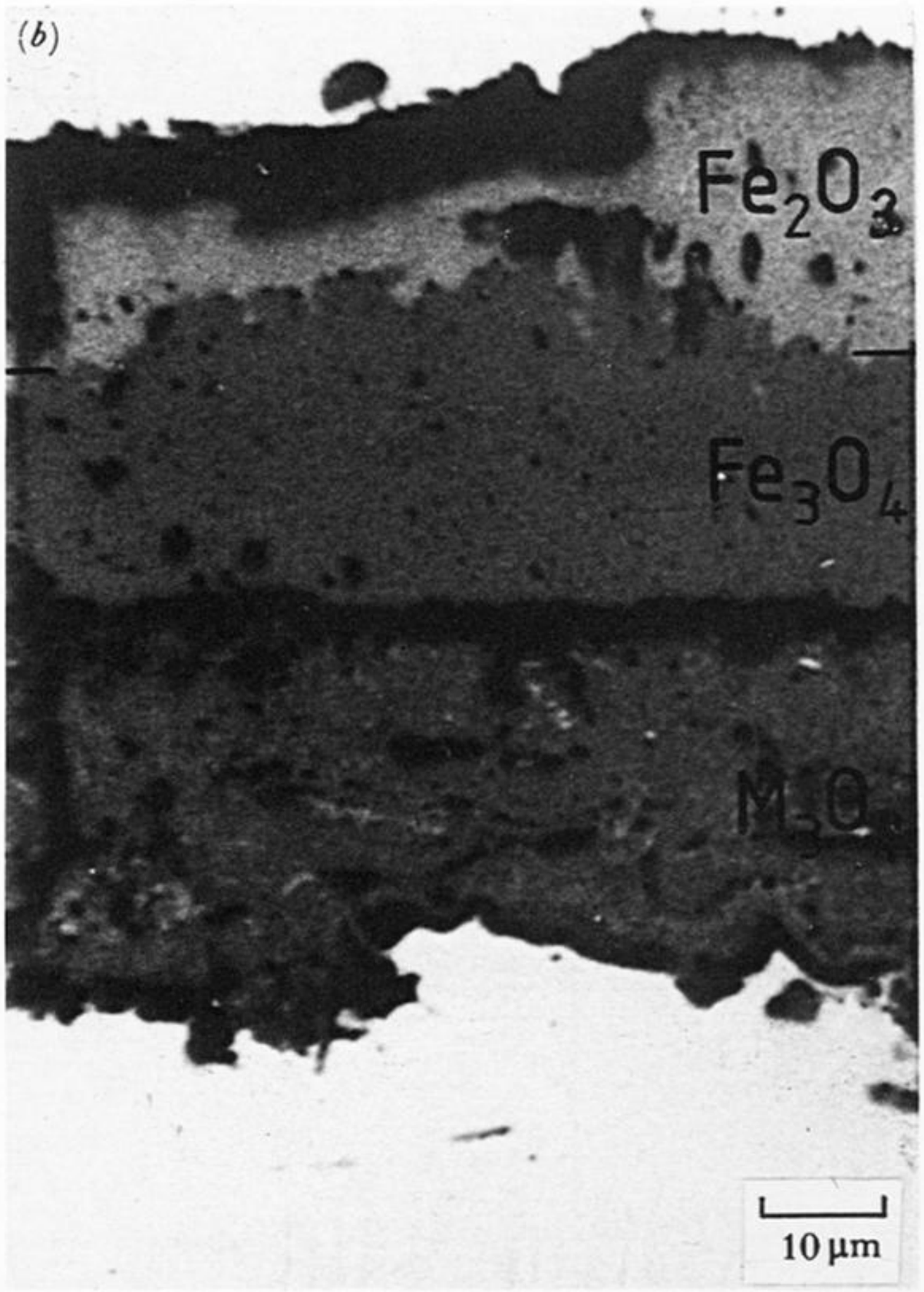

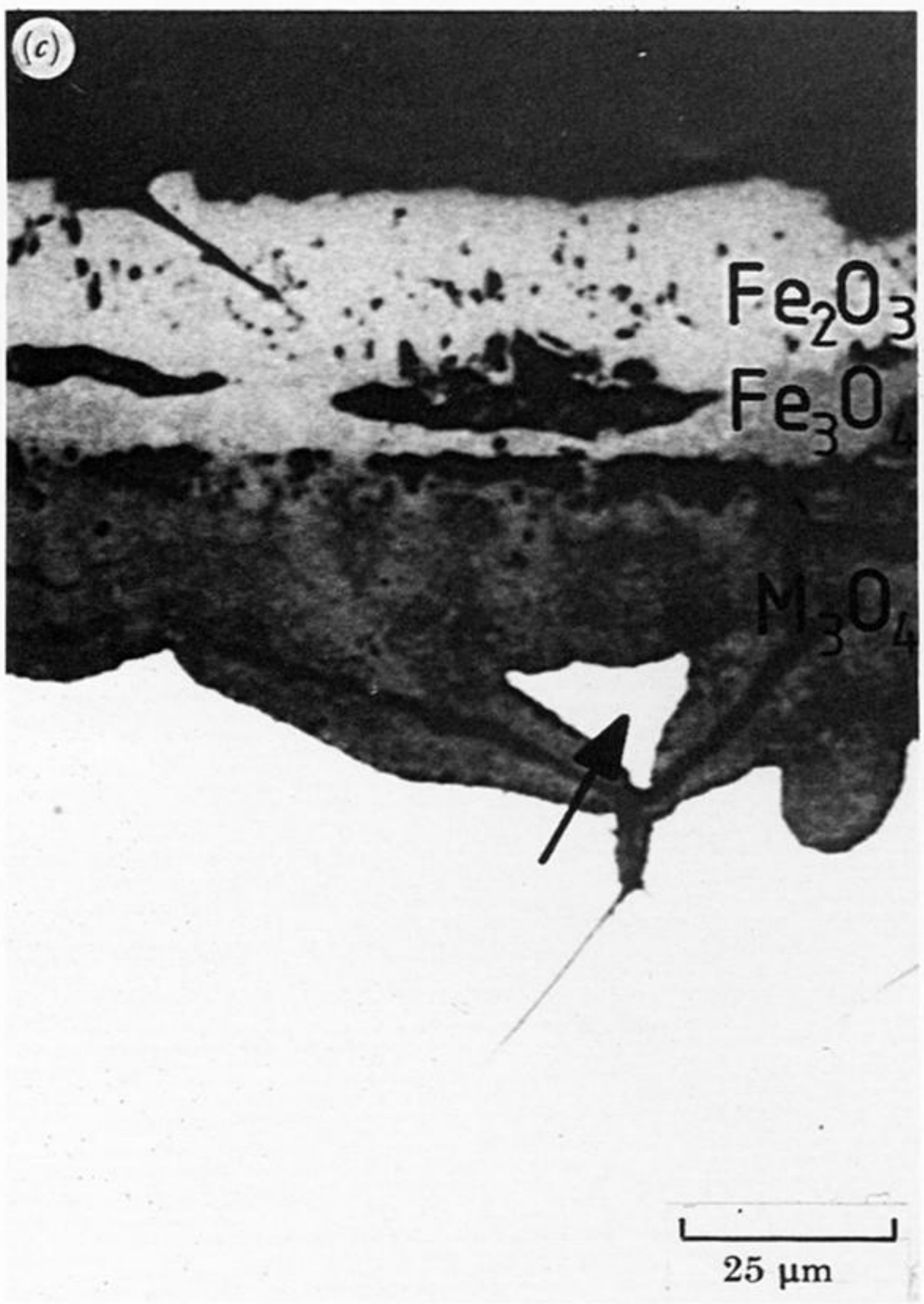

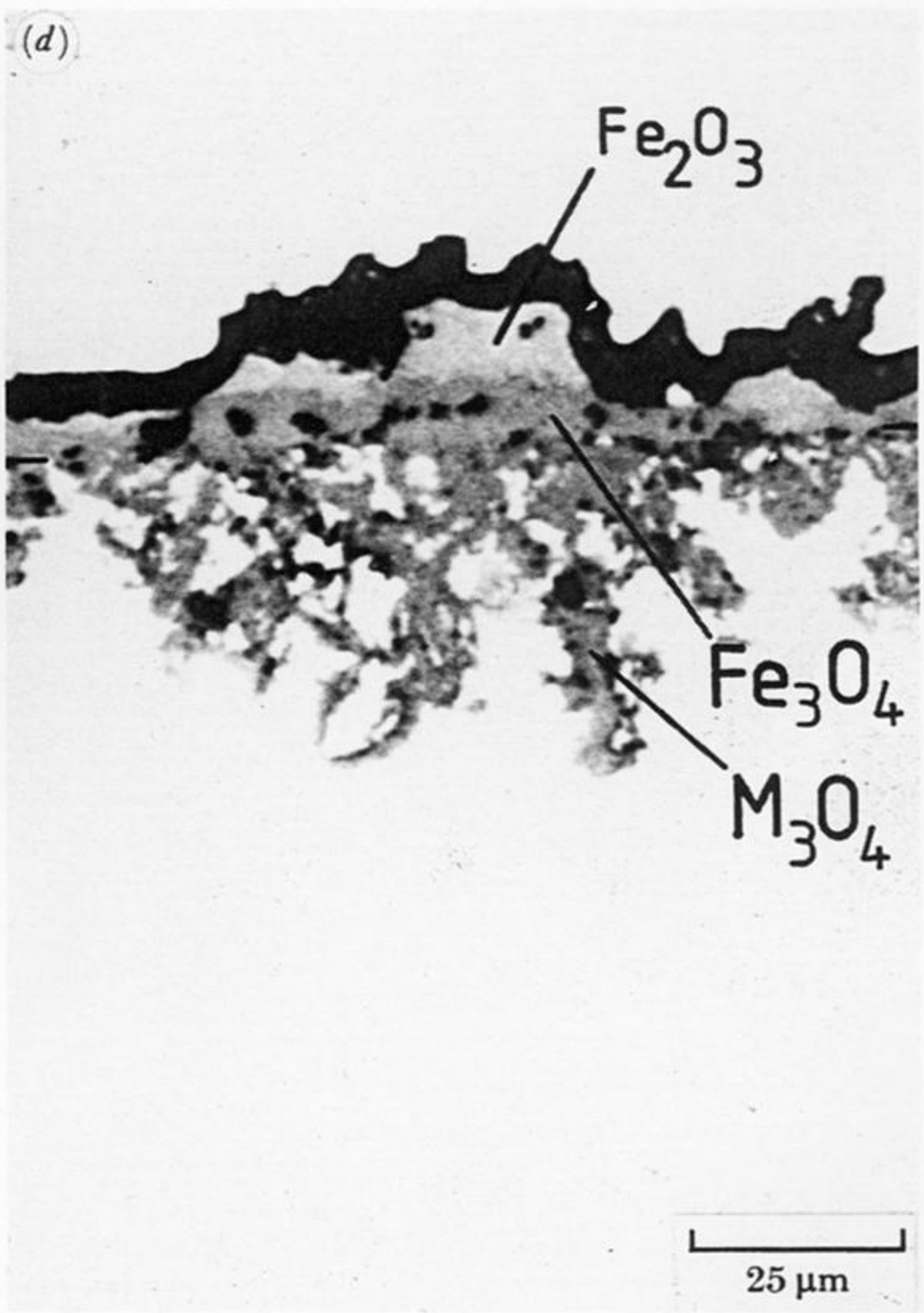

FIGURE 5. Optical micrographs of the scales formed on the Fe–9Cr and Fe–10Cr–Ni alloys after 1000 h oxidation in air at 600 °C. (*a*) Fe–9Cr–1Mo: a thin layer of 'protective' oxide, lying adjacent to a multilayered scale is arrowed; (*b*) Fe–10Cr–10Ni: note the separation of the scale at the Fe_3O_4–M_3O_4 interface; (*c*) Fe–10Cr–20Ni: unoxidized alloy situated in the inward grown M_3O_4 scale is arrowed; (*d*) Fe–10Cr–34Ni: note the inhomogeneity in the thicknesses of the scale.

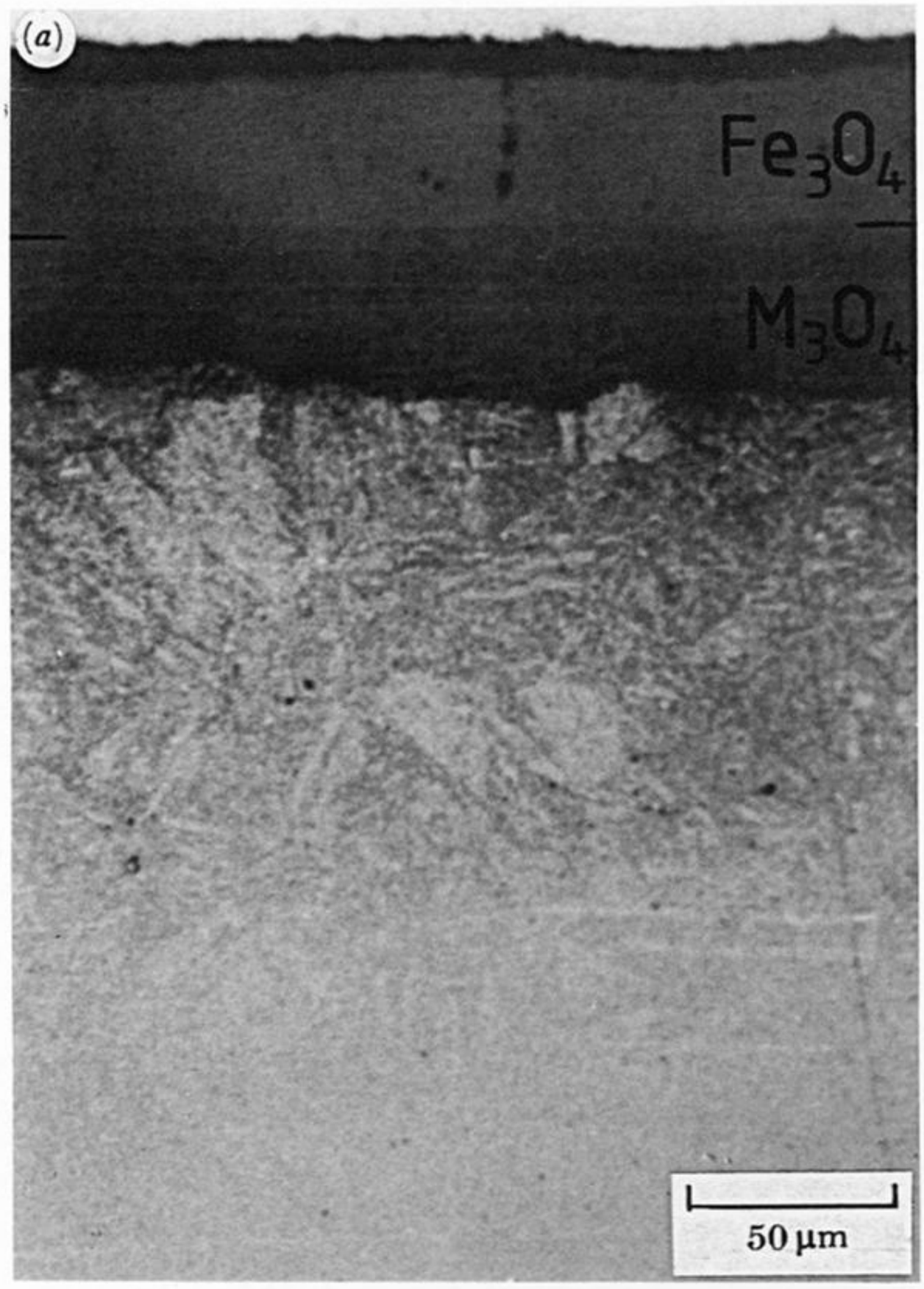

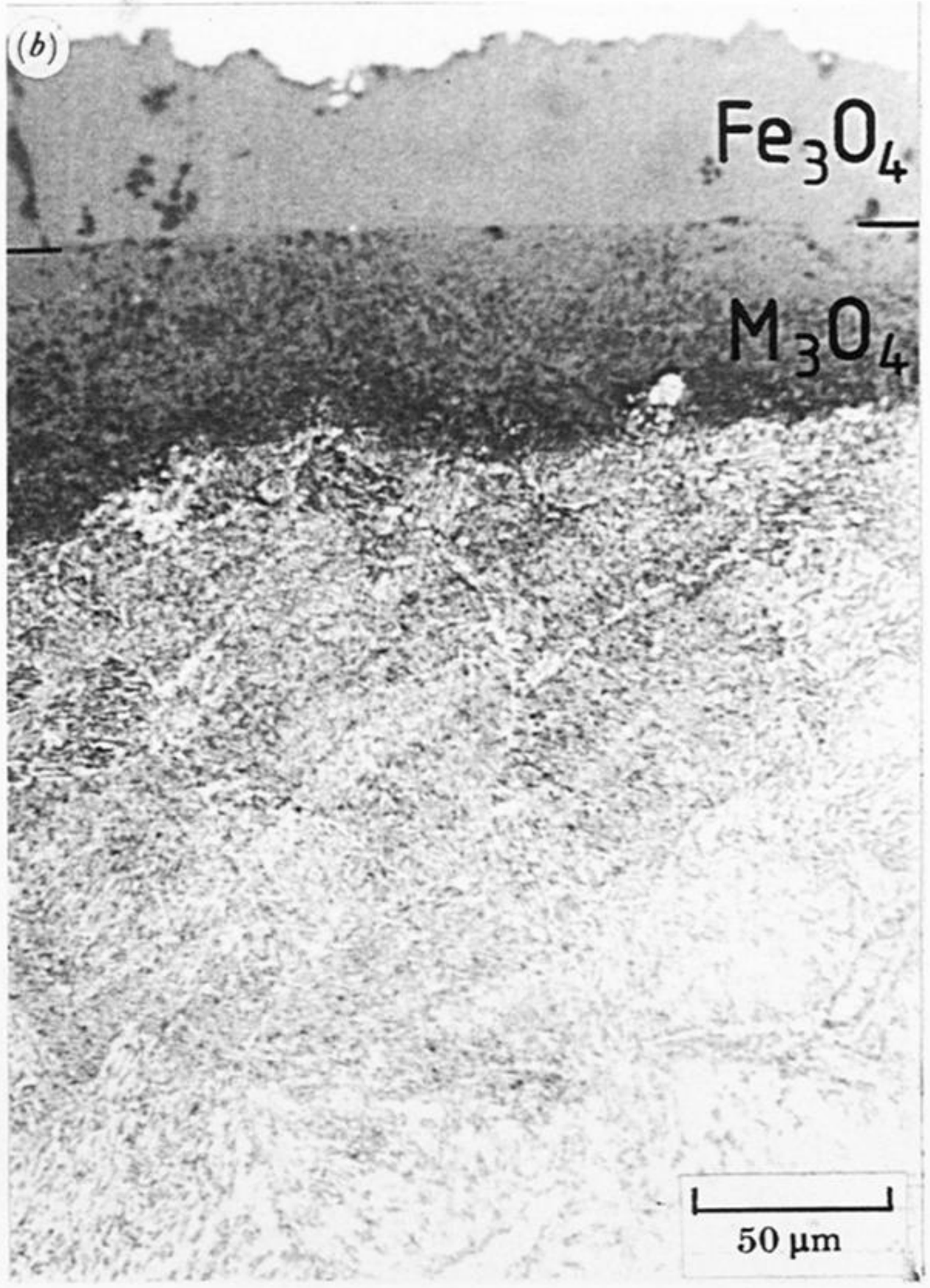

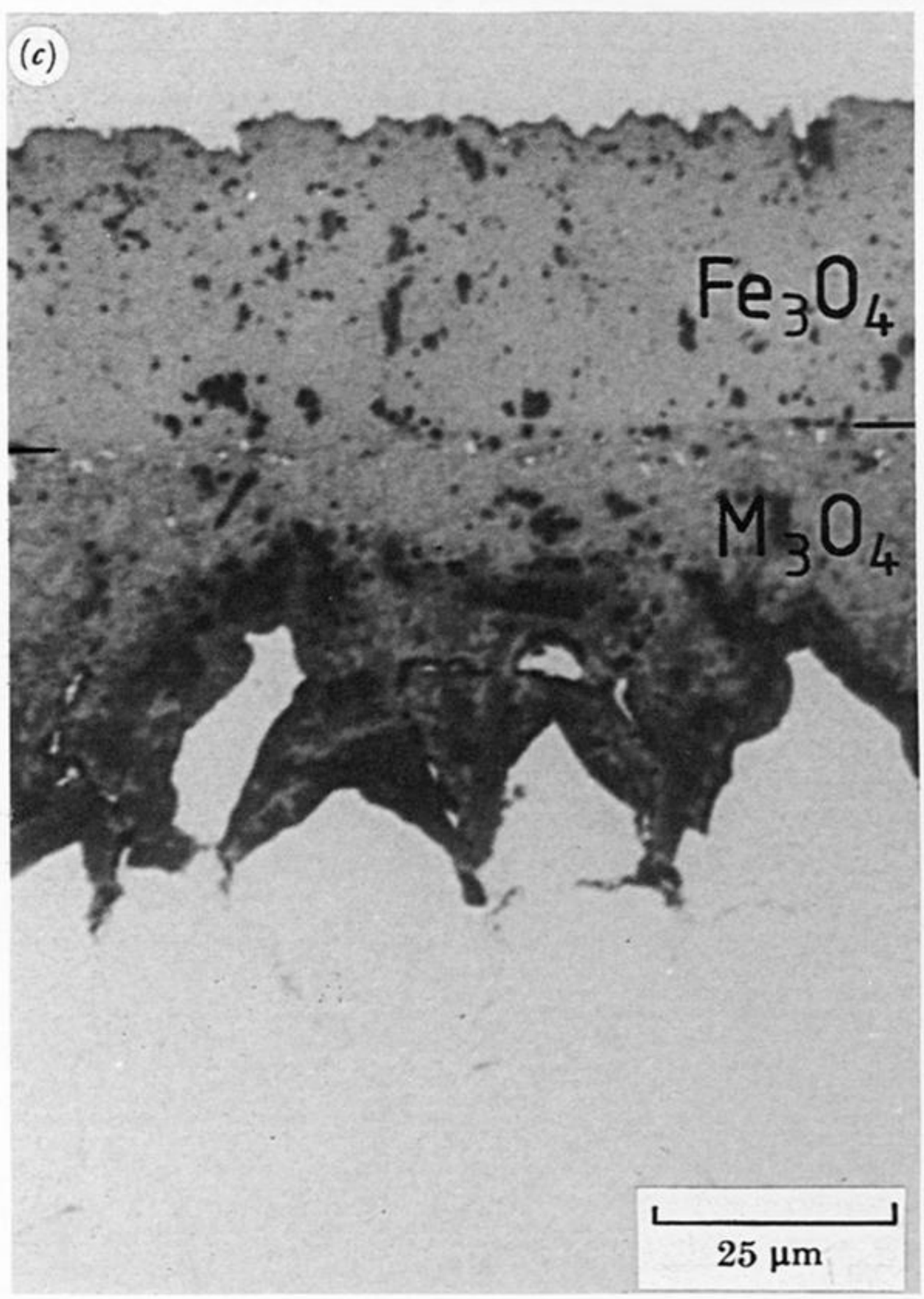

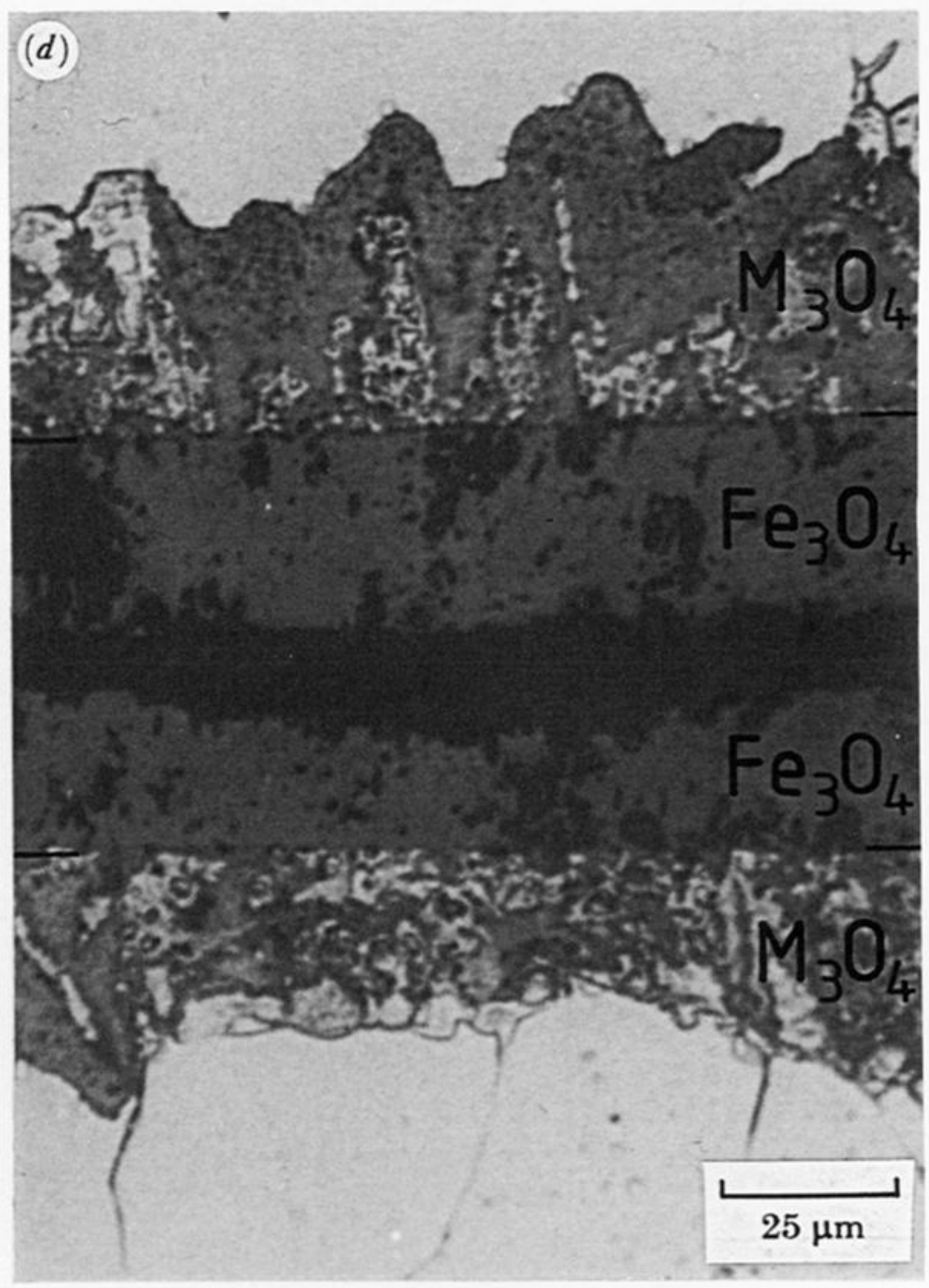

FIGURE 6. Optical micrographs of the scales formed on the Fe–9Cr and Fe–10Cr–Ni alloys after 1000 h oxidation in 1 % CO–CO_2 at 600 °C. (*a*) Fe–9Cr–1Mo; (*b*) Fe–10Cr–10Ni; (*c*) Fe–10Cr–20Ni; (*d*) Fe–10Cr–34Ni; (note that this is a micrograph of two scales lying face to face). It should be noted that carbide precipitation has occurred in both the 9Cr–1Mo and 10Cr–10Ni alloys to a depth of *ca.* 100–150 μm beneath the scales by comparison with the austenitic 10Cr–20Ni and 10Cr–34Ni alloys where precipitation is not observed.

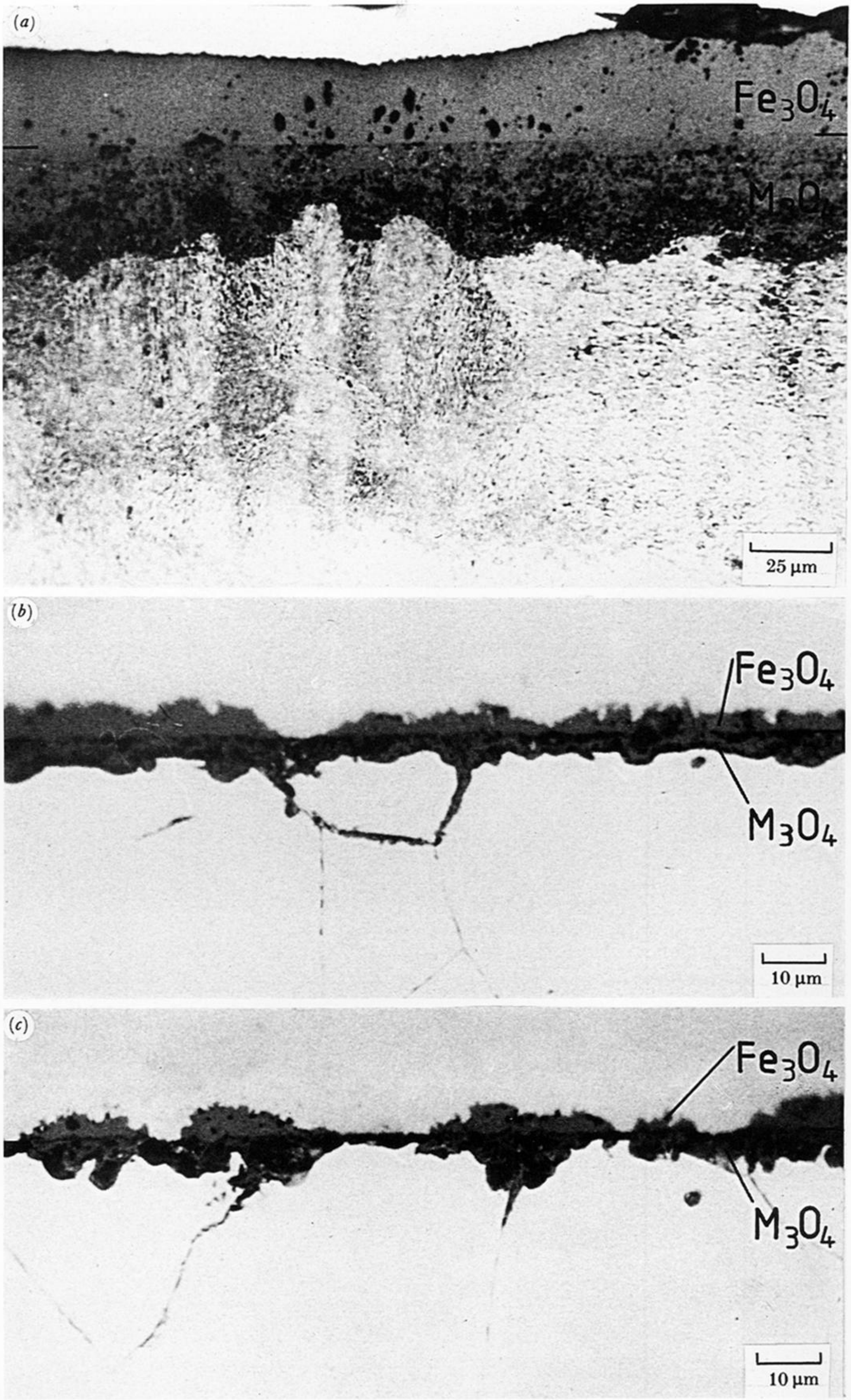

FIGURE 7. Optical micrographs of the scales formed on the Fe–10Cr–Ni alloys after 125 h oxidation in 1 % CO–CO_2 at 600 °C. (*a*) Fe–10Cr–10Ni; (*b*) Fe–10Cr–20Ni; (*c*) Fe–10Cr–34Ni.

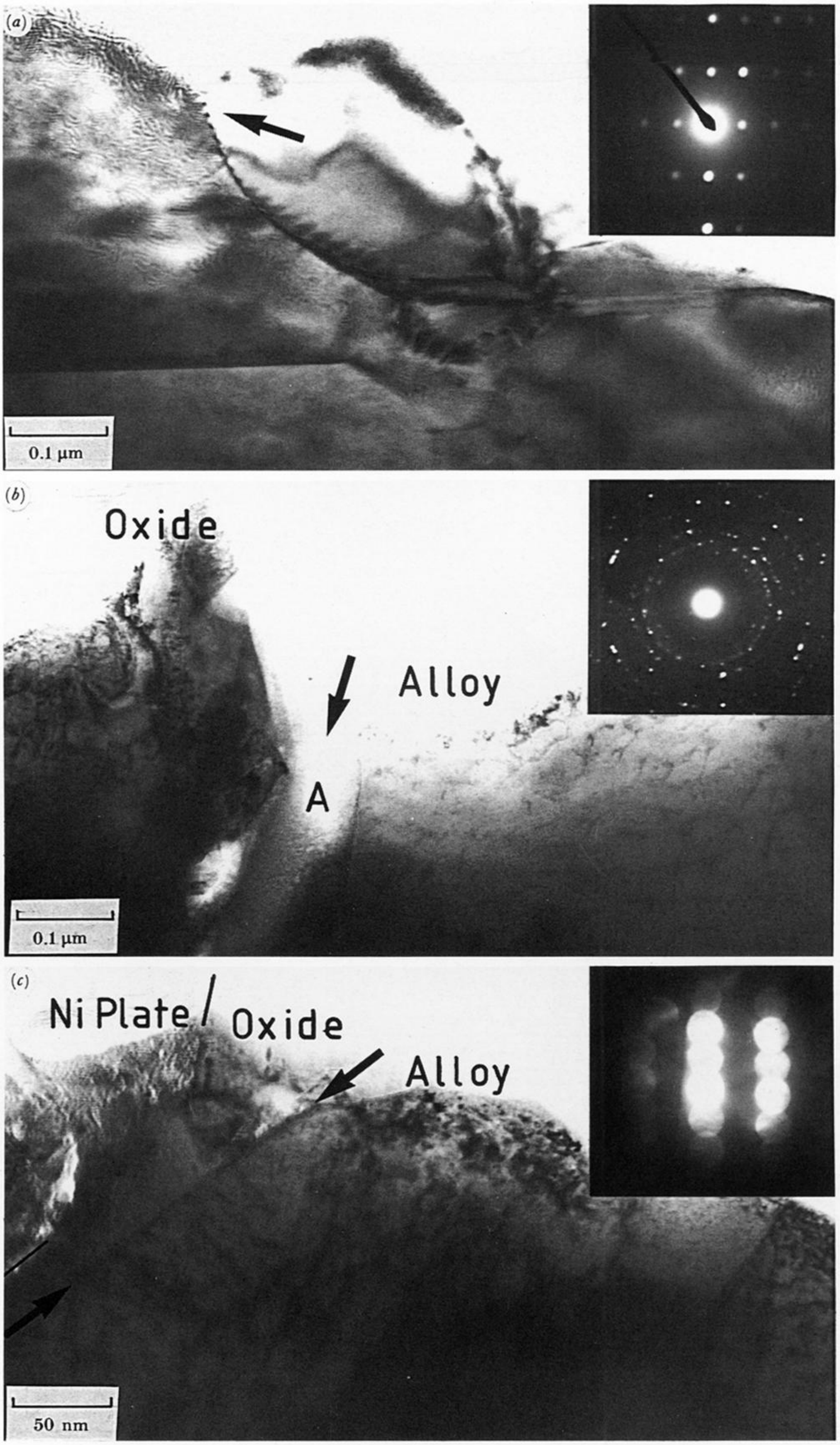

FIGURE 8. Bright field 'edge on' TEM micrographs showing the microstructures of the 'non-protective' and 'protective' scales formed on Fe–9Cr–1Mo in air at 600 °C after 1000 h. (*a*) Columnar grained and outward growing magnetite and inset $(112)_{Fe_3O_4}$ diffraction pattern. The arrow is normal to and approximately 1.5 μm from the Fe_3O_4–Fe_2O_3 interface. (*b*) The metal–oxide interface in the 'non-protective' scale, where the inward grown M_3O_4 is fine grained and non-equiaxed (see inset diffraction pattern). Partial separation of the two phases has occurred at the alloy–oxide interface, as at A, a region which has been infilled with sputter contamination. (*c*) Thin 'protective' M_2O_3 overlying ferrite. Note the flat alloy–oxide interface (arrowed). The inset diffraction pattern is a $(1211)_{M_2O_3}$ normal.

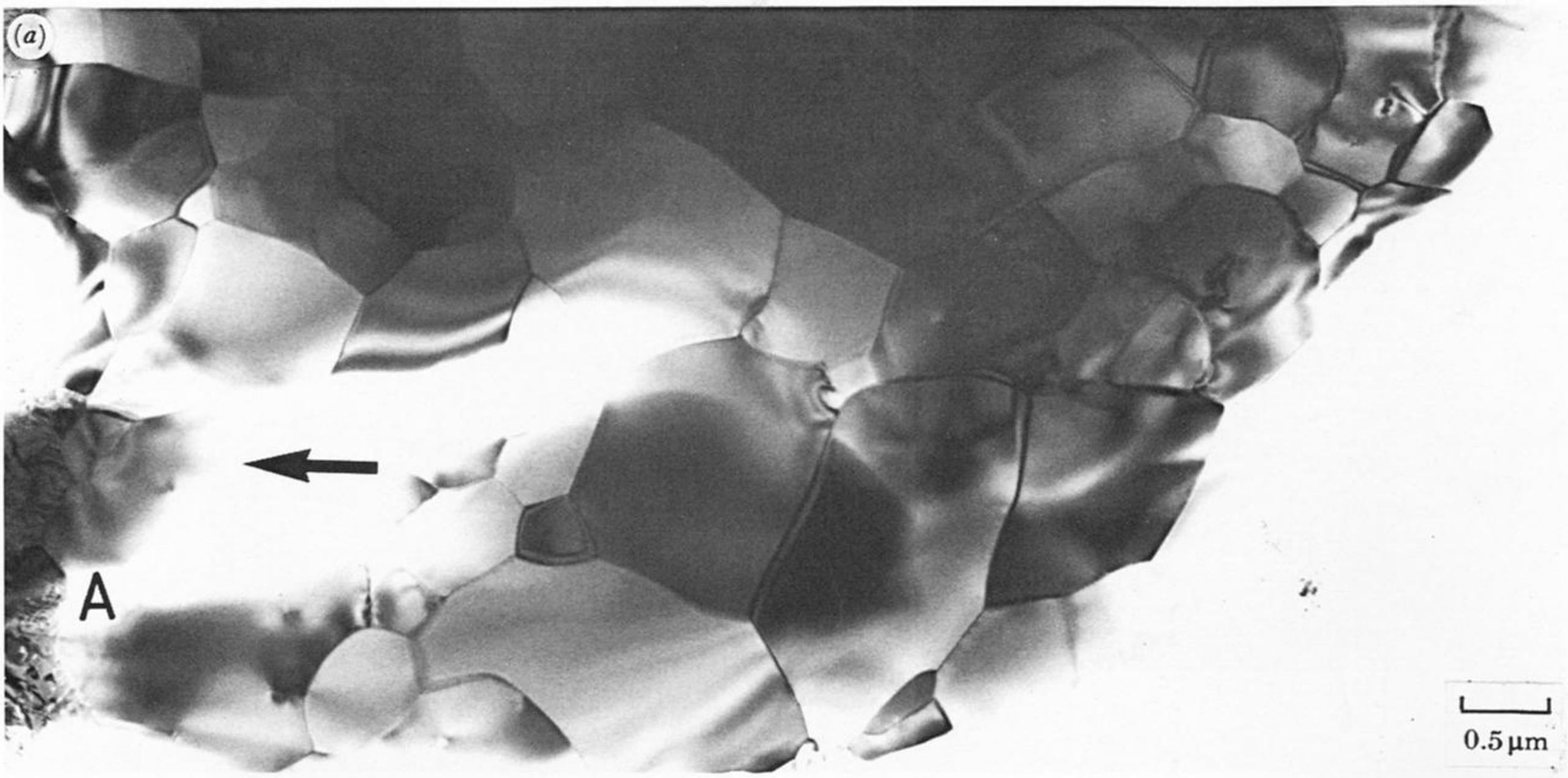

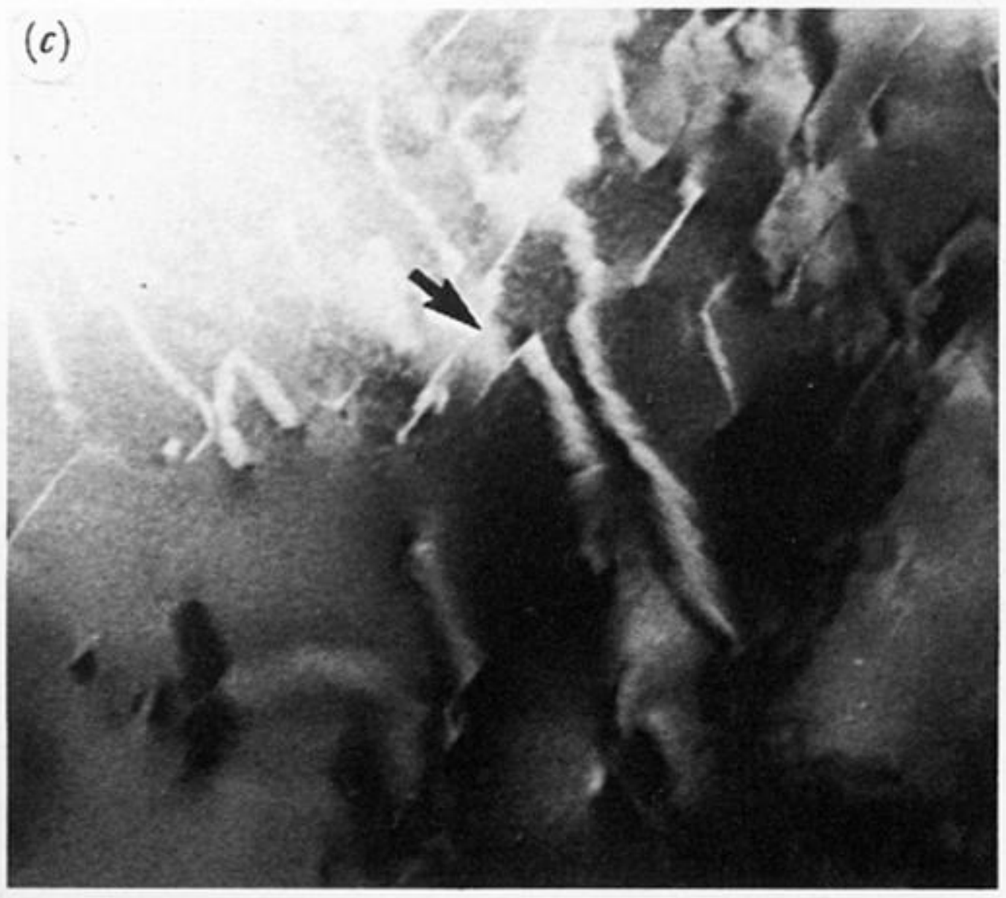

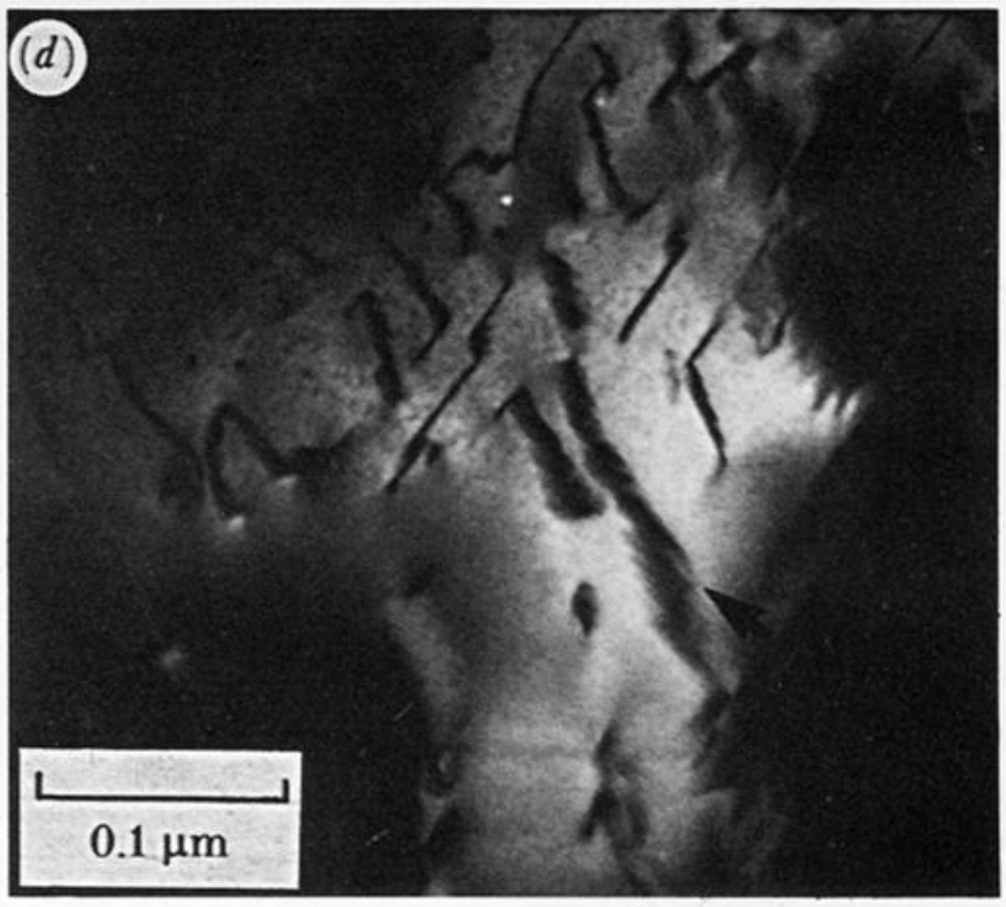

FIGURE 10. Microstructure of the magnetite formed on Fe–10Cr–10Ni in air after 1000 h at 600 °C showing the coarse grained morphology. (*a*) Approximately 10 μm from the original metal surface. The arrow gives the direction of the outer layer of haematite, bright-field. (*b*) A region from A in (*a*) approximately 5 μm from the Fe_3O_4–Fe_2O_3 interface, where defects may be observed, as arrowed, bright-field. (*c*) Bright-field and (*d*) dark-field images showing the defects in the magnetite at a higher magnification.

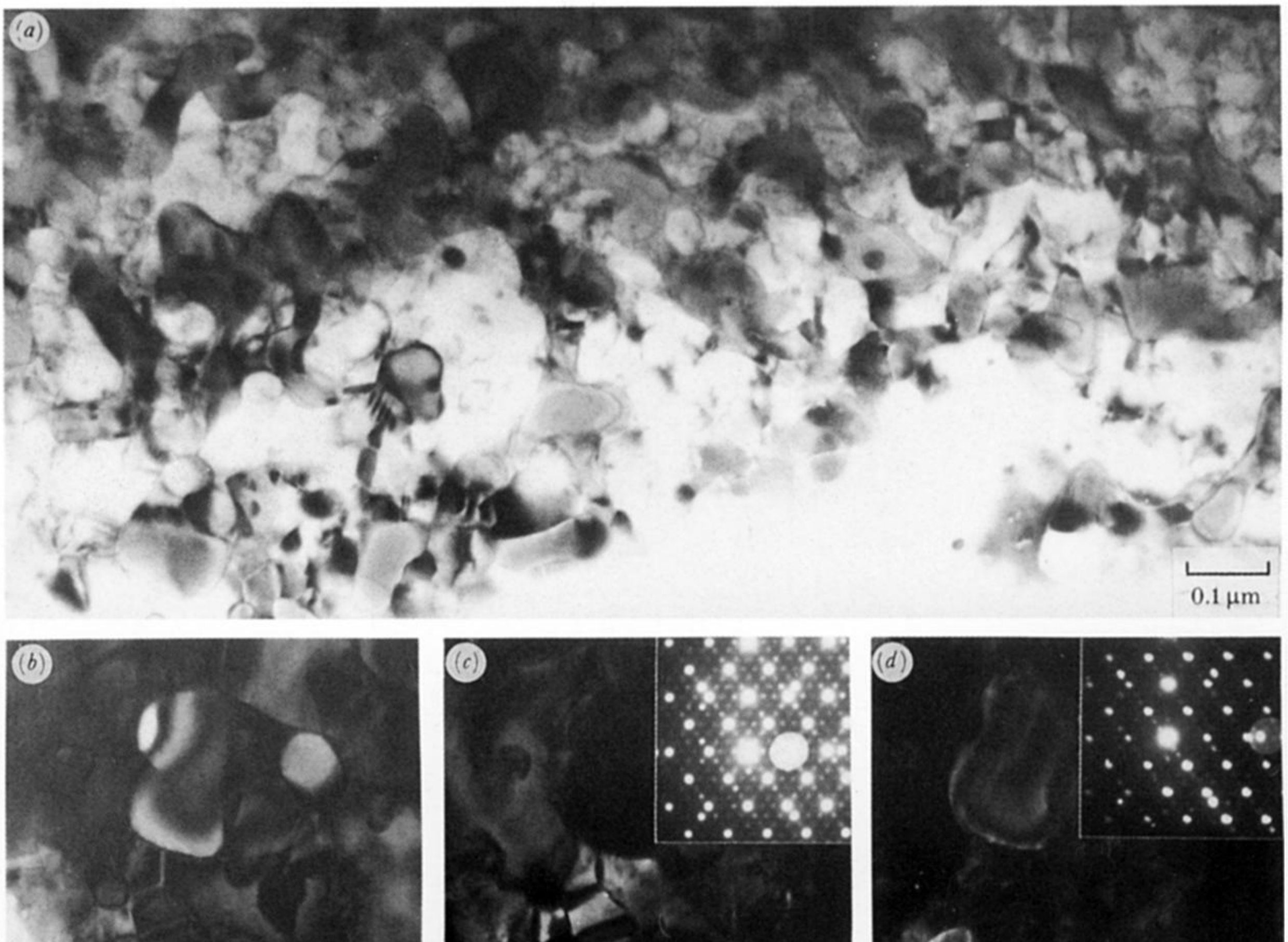

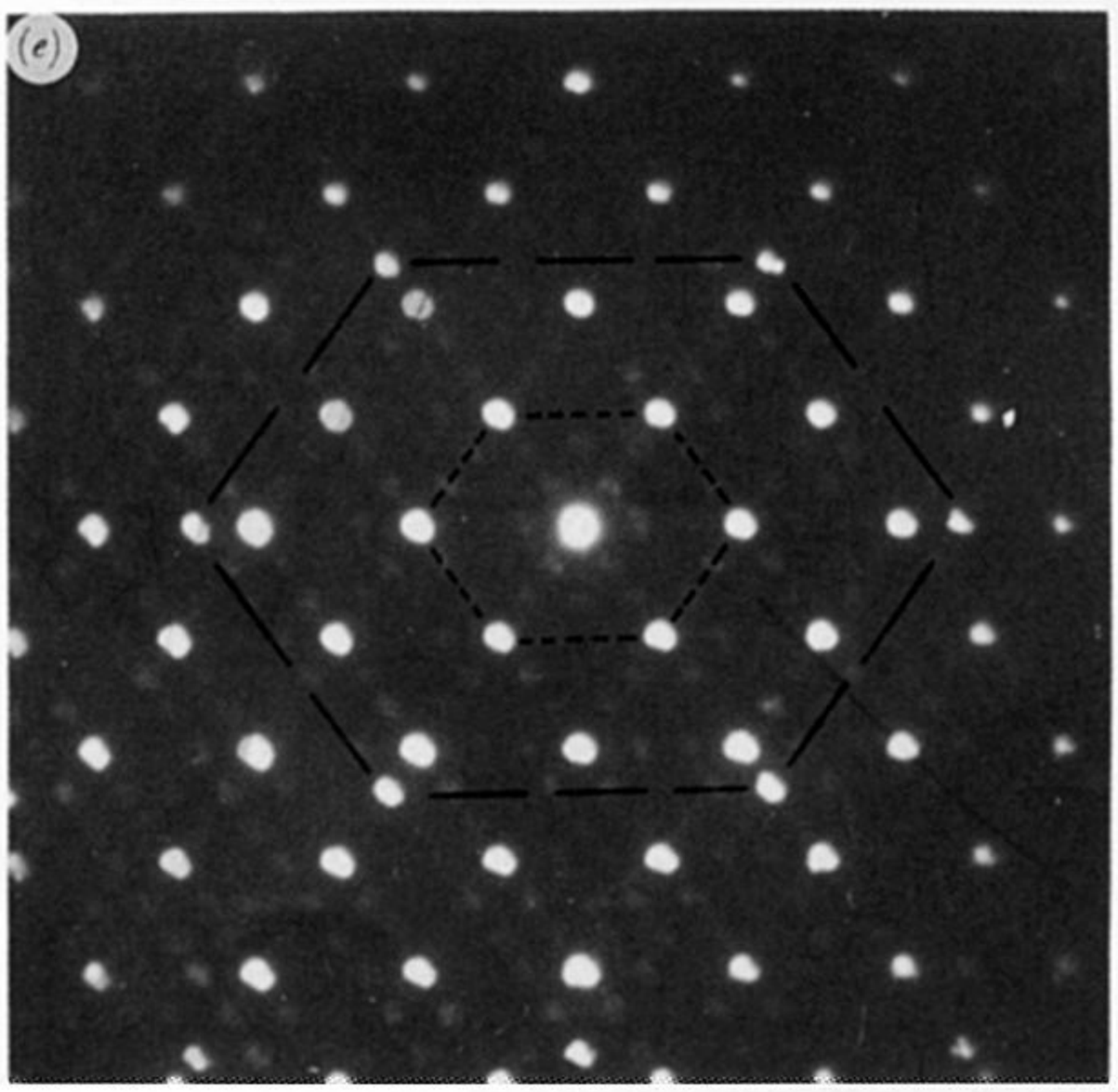

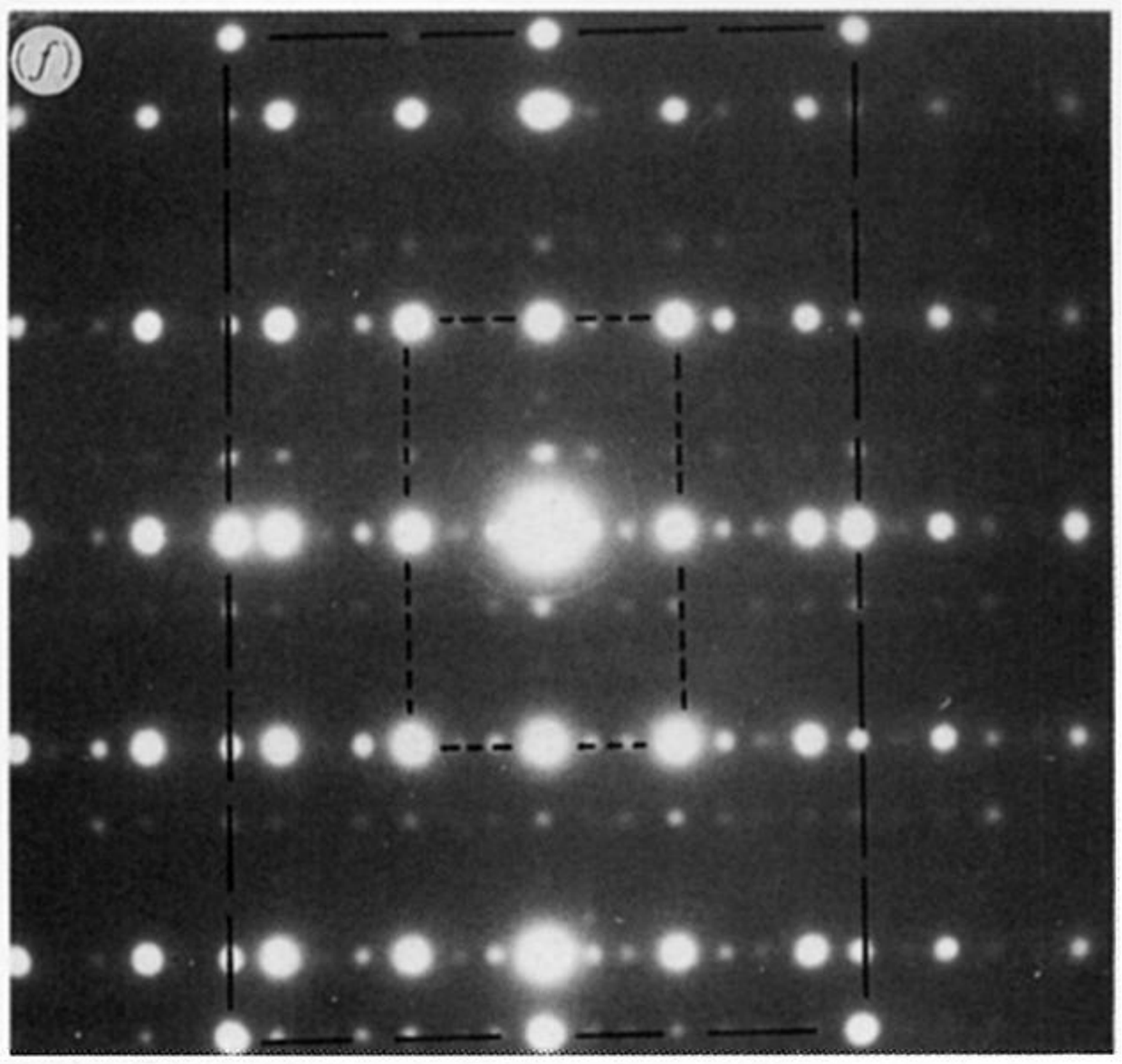

FIGURE 11. Microstructure of the 'internal' scale formed on Fe–10Cr–10Ni in air at 600 °C after 1000 h. (*a*) Low magnification bright field image of an area approximately 15 μm from the metal–oxide interface, (*b*) higher magnification bright-field, (*c*) dark-field (imaged with a (200) spinel reflection), (*d*) dark-field (imaged with a (200) austenite reflection). Diffraction patterns demonstrating the epitaxial relationship between austenite and the larger lattice parameter oxide are shown in (*e*) $(011)_{\gamma}//(011)_{M_3O_4}$ and (*f*) $(112)_{\gamma}//(112)_{M_3O_4}$.

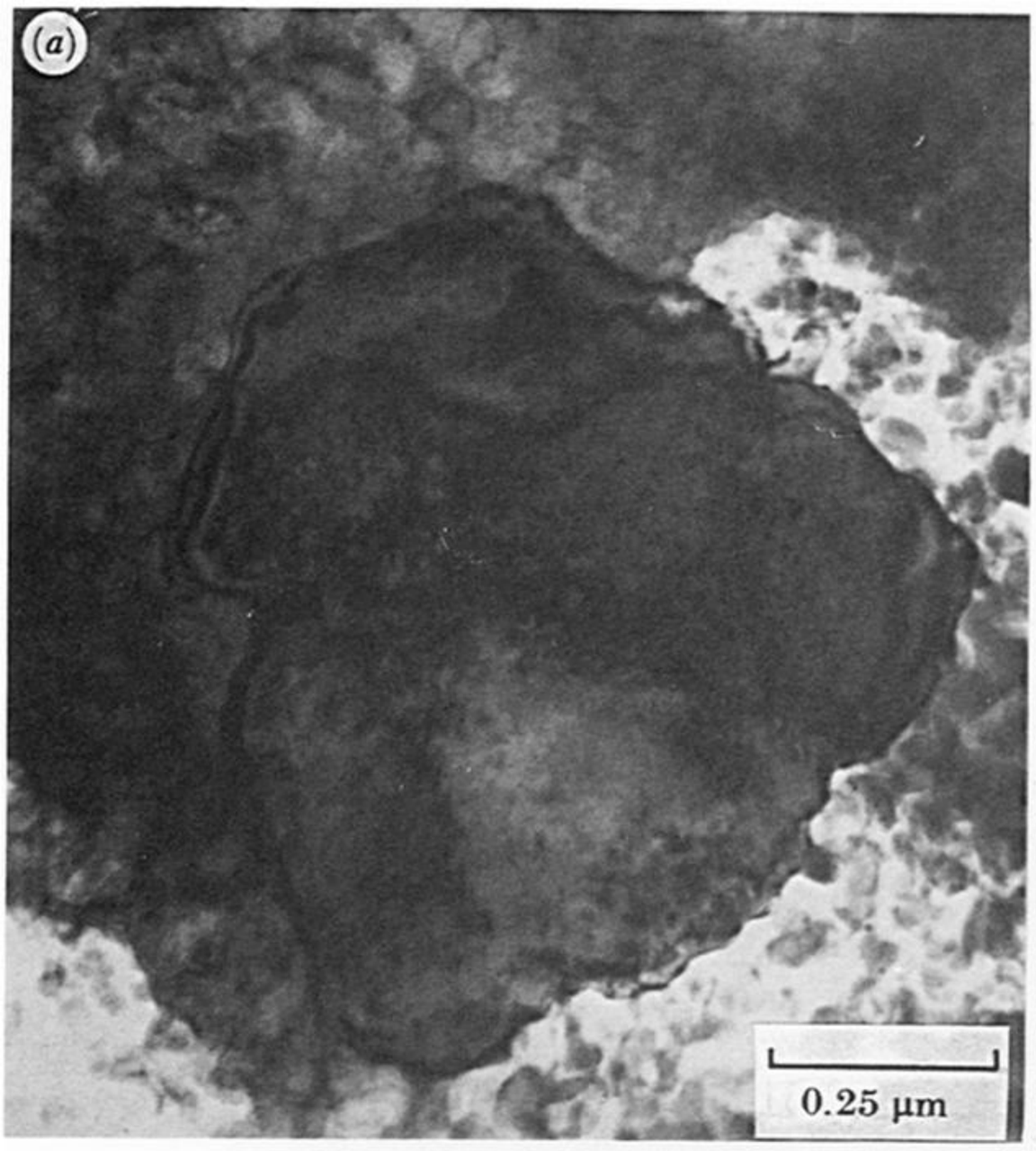

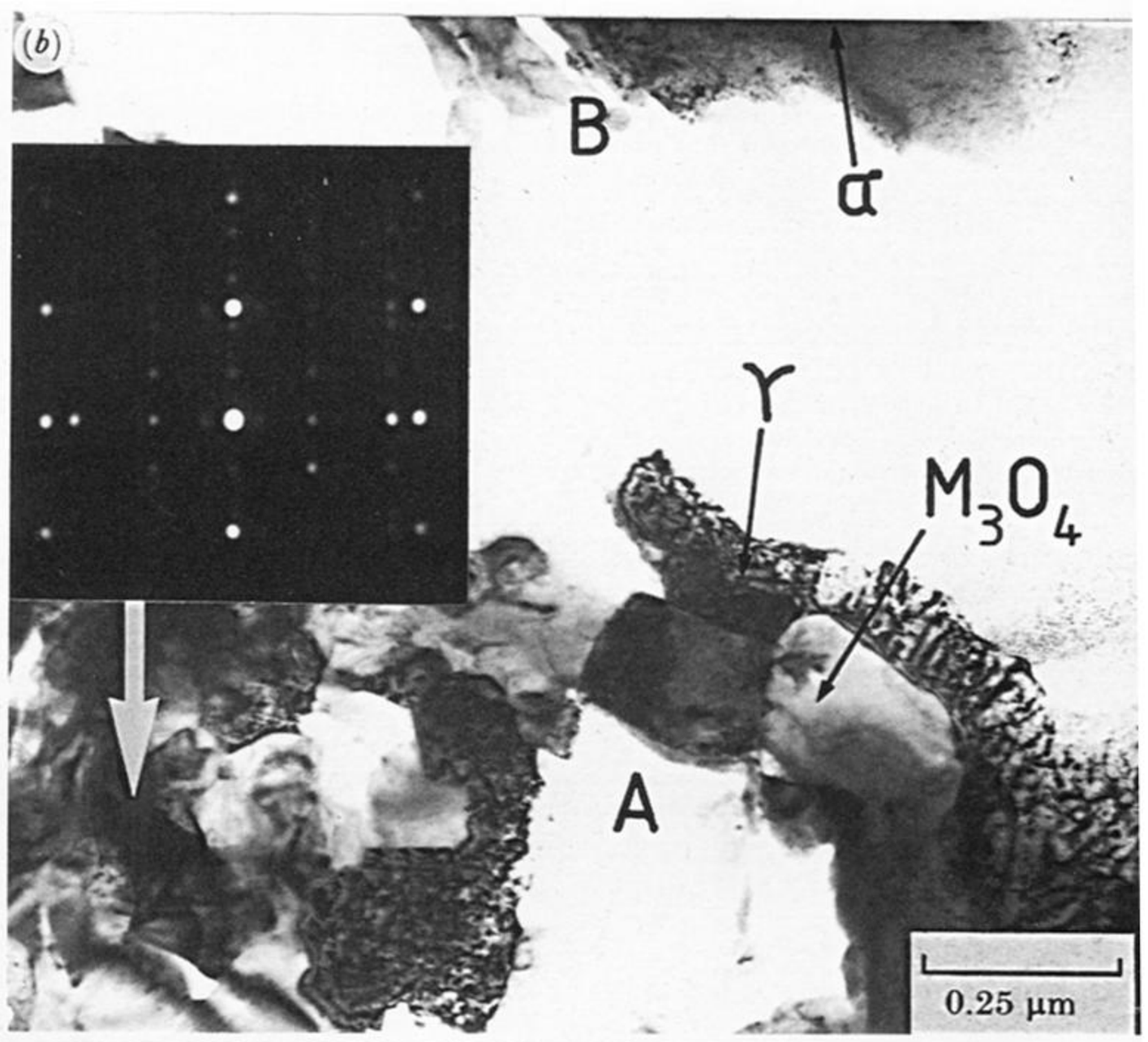

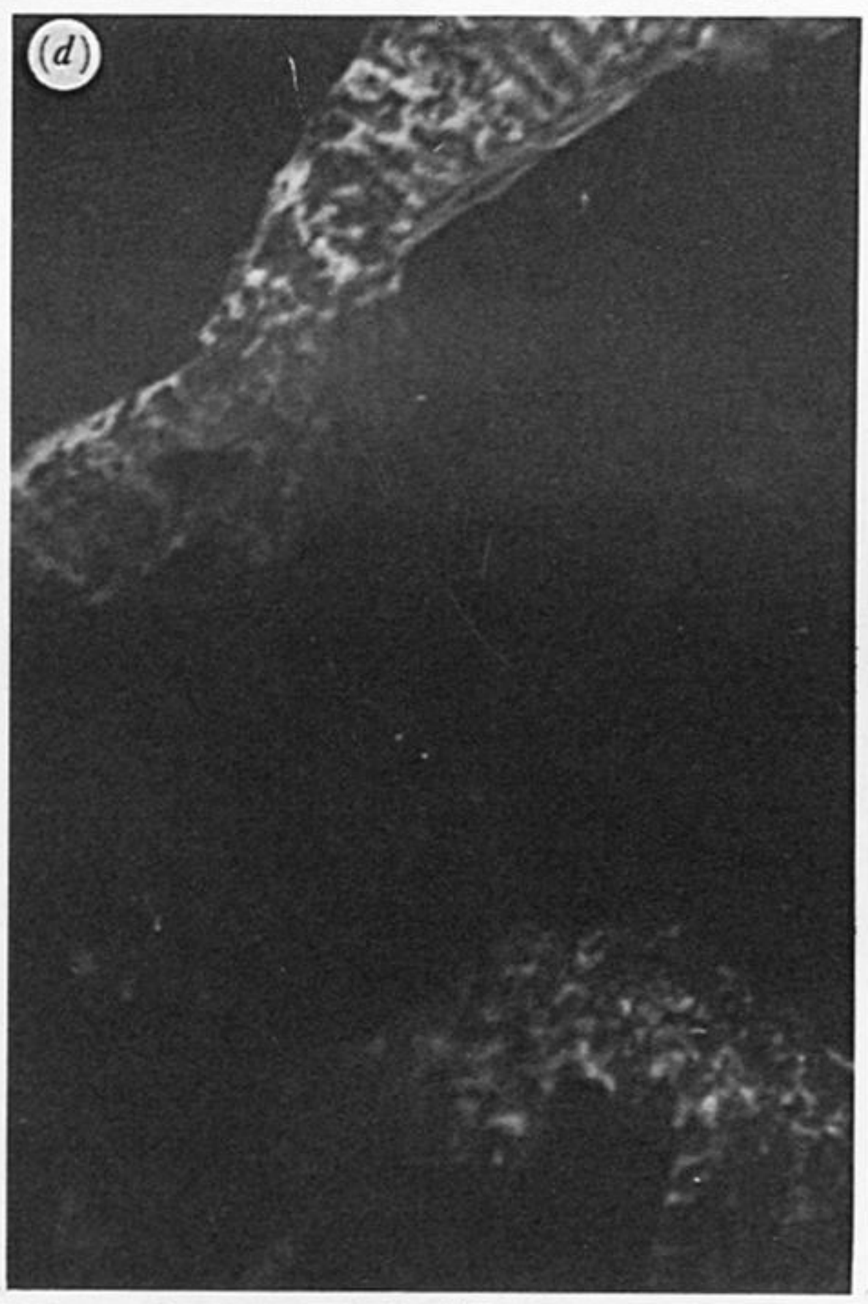

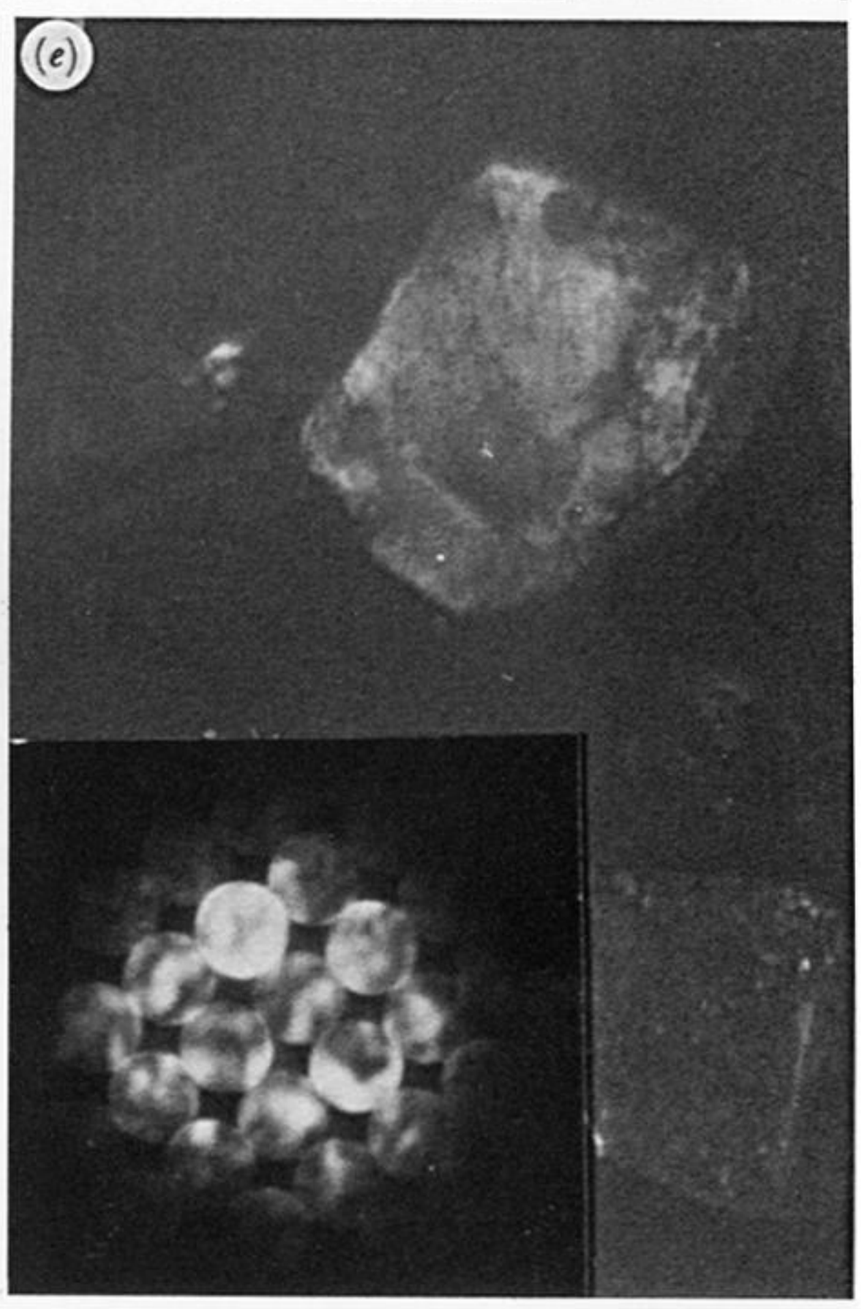

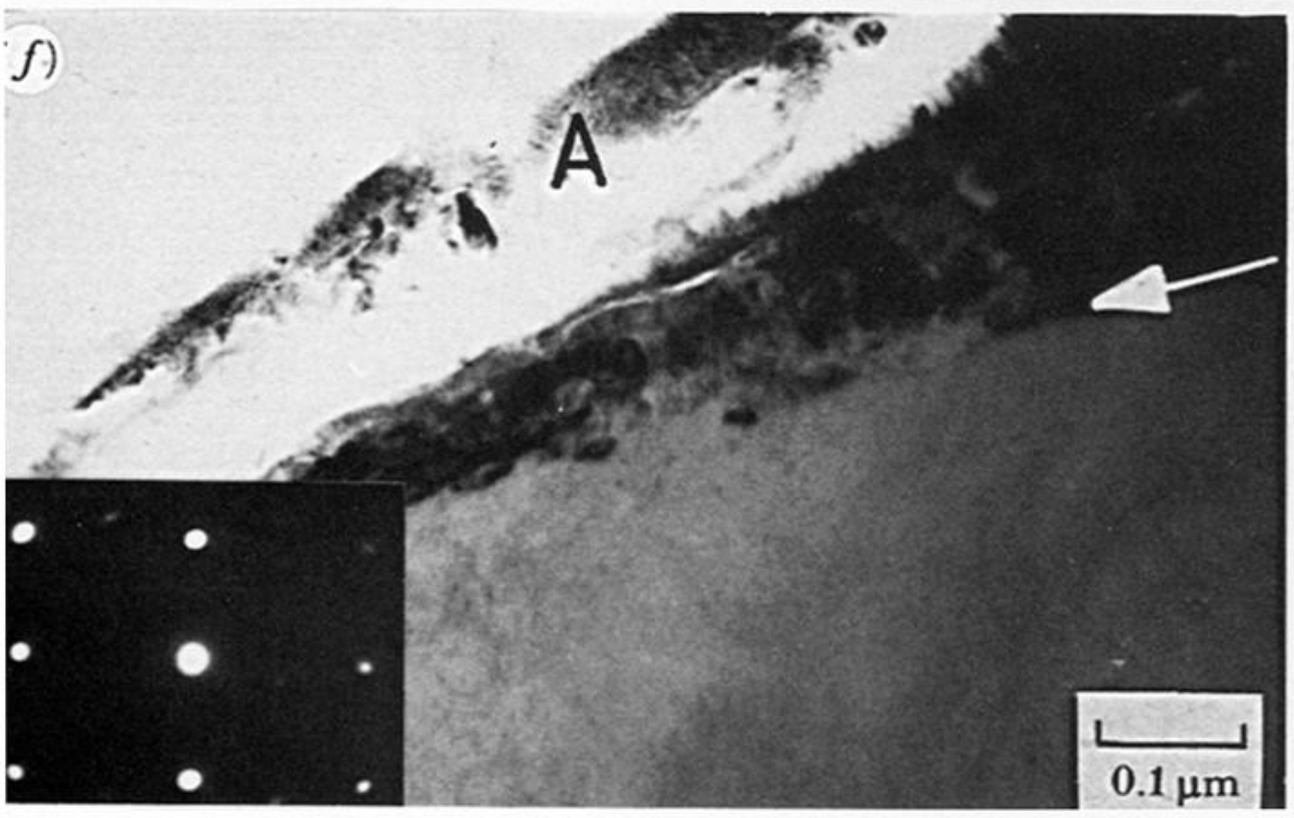

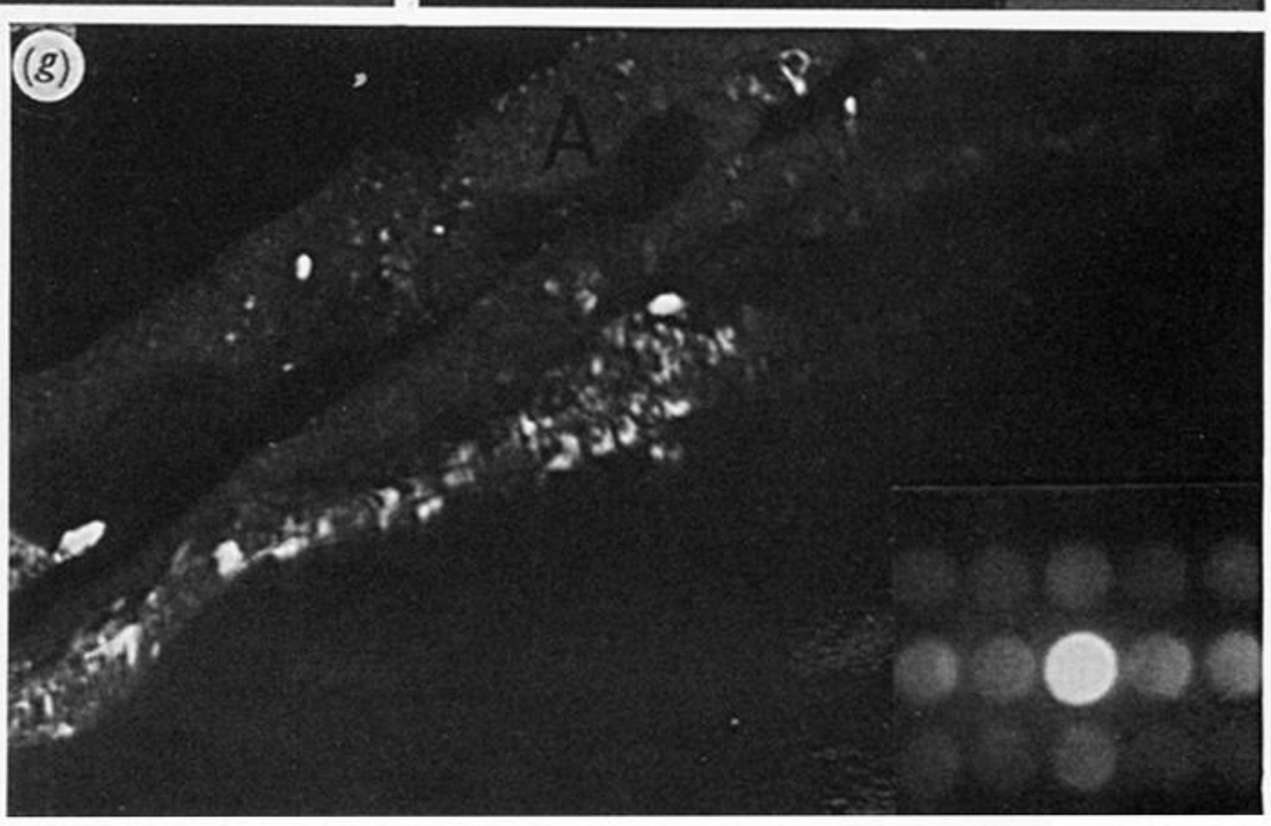

FIGURE 12. Fe–10Cr–10Ni oxidized in air for 1000 h at 600 °C in air showing the scale microstructure in the metal–oxide interface region, 'edge-on' TEM. (*a*) Coarse grained RI M_3O_4 surrounded by epitaxial, and finer grained, $\gamma//M_3O_4$ scale, situated approximately 2.5 μm from the alloy–oxide interface and approximately 10 μm beneath the region shown in figure 11. (*b*) Low magnification bright-field micrograph of the diffuse alloy–oxide interface. A region of OI oxide is arrowed (see inset diffraction pattern) which is approximately 1 μm beneath the alloy–oxide interface, while the ferritic alloy is also marked as at B. A region of RI oxide and transformed alloy as at A is shown enlarged in (*c*), (*d*) and (*e*). (*c*) Bright-field micrograph from A in (*b*), (*d*) dark-field, imaged with an austenite reflection, and (*e*) dark-field, imaged with a spinel reflection. The inset shows a $(233)_{M_3O_4}$ diffraction pattern. (*f*) Grain boundary oxide formation (arrowed) in the ferritic 10Cr–10Ni alloy, as at B in (*b*). Note the microcrystalline sputter contamination at A, some of which is imaged in (*g*) and the surface oxide formation in the ferrite (see inset diffraction pattern). (*g*) Dark-field, imaged with a spinel reflection. The inset shows a $(100)_{M_3O_4}$ diffraction pattern.

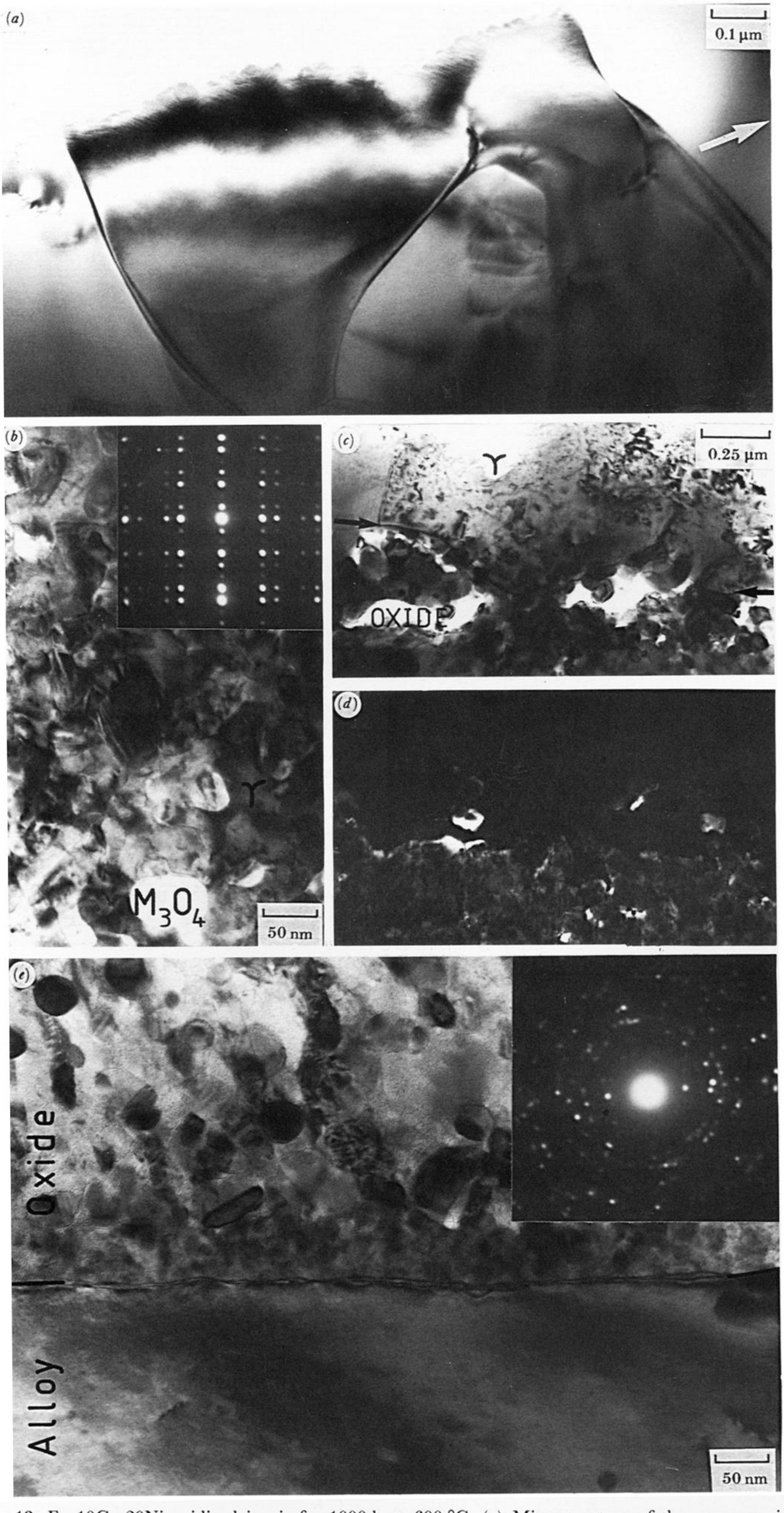

FIGURE 13. Fe–10Cr–20Ni oxidized in air for 1000 h at 600 °C. (*a*) Microstructure of the coarse grained and columnar magnetite layer. The arrow is normal to and approximately 5 μm from the original metal surface. Here the oxide is characteristically defect free. (*b*) A region of OI scale approximately 10 μm from the original metal surface. The epitaxial relationship between the two phases is shown in the inset diffraction pattern. (*c*) A *ca.* 1 μm grain of unoxidized (and nickel enriched) austenite encapsulated by RI fine grained spinel oxide. Bright-field and (*d*) dark-field, as imaged with a spinel reflection. The arrows in (*c*) and (*d*) delineate the interface between the RI oxide and the austenite. (*e*) The metal–oxide interface, where the scale consists of fine grained M_3O_4 and does not contain austenite (see inset diffraction pattern).

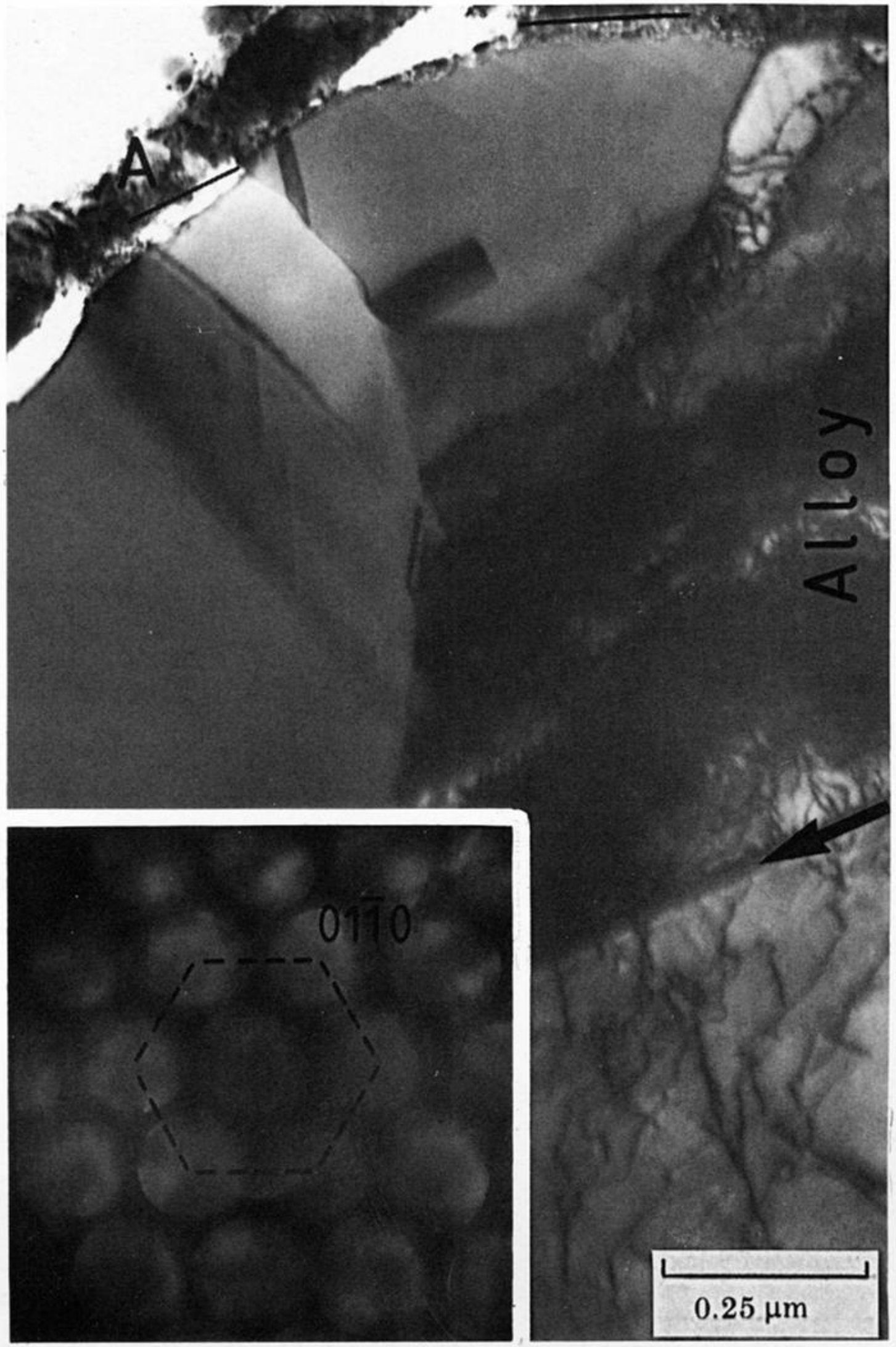

FIGURE 14. Fe–10Cr–34Ni oxidized in air for 1000 h at 600 °C showing a thin layer of 'protective' oxide sandwiched between the alloy and supportive nickel plate, as at A. Note that the alloy shows partial recrystallization to a depth approximately 1 μm beneath the scale, as arrowed.

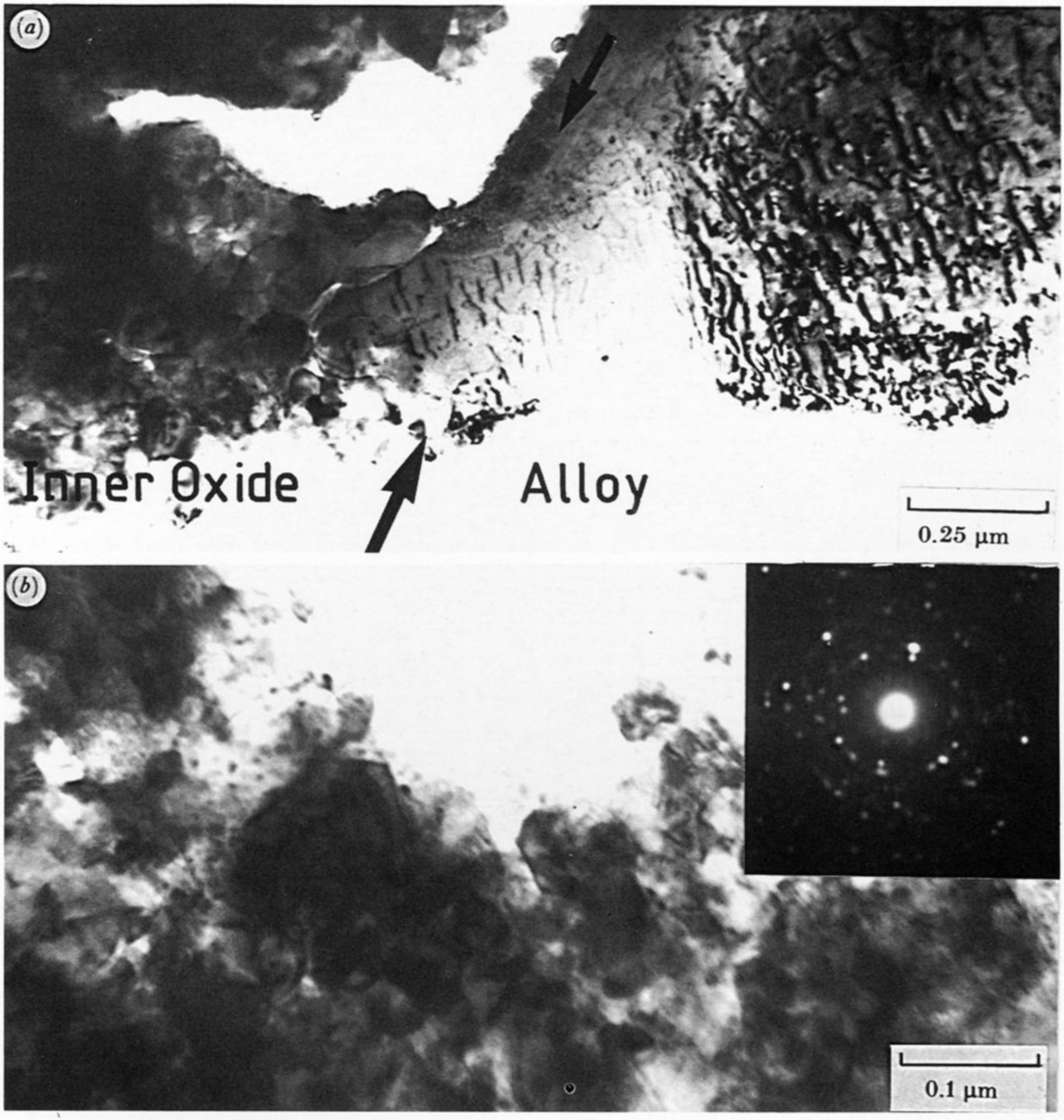

FIGURE 15. Fe–10Cr–34Ni oxidized in air for 1000 h at 600 °C showing 'non-protective' and RI oxide (*a*) at the metal–oxide interface, which is arrowed. A region which has preferentially ion-beam milled to form a large hole may be seen in the oxide. (*b*) The fine grained RI oxide approximately 1 μm from the metal–oxide interface. The M_3O_4 oxide is untextured, as demonstrated by the inset diffraction pattern.

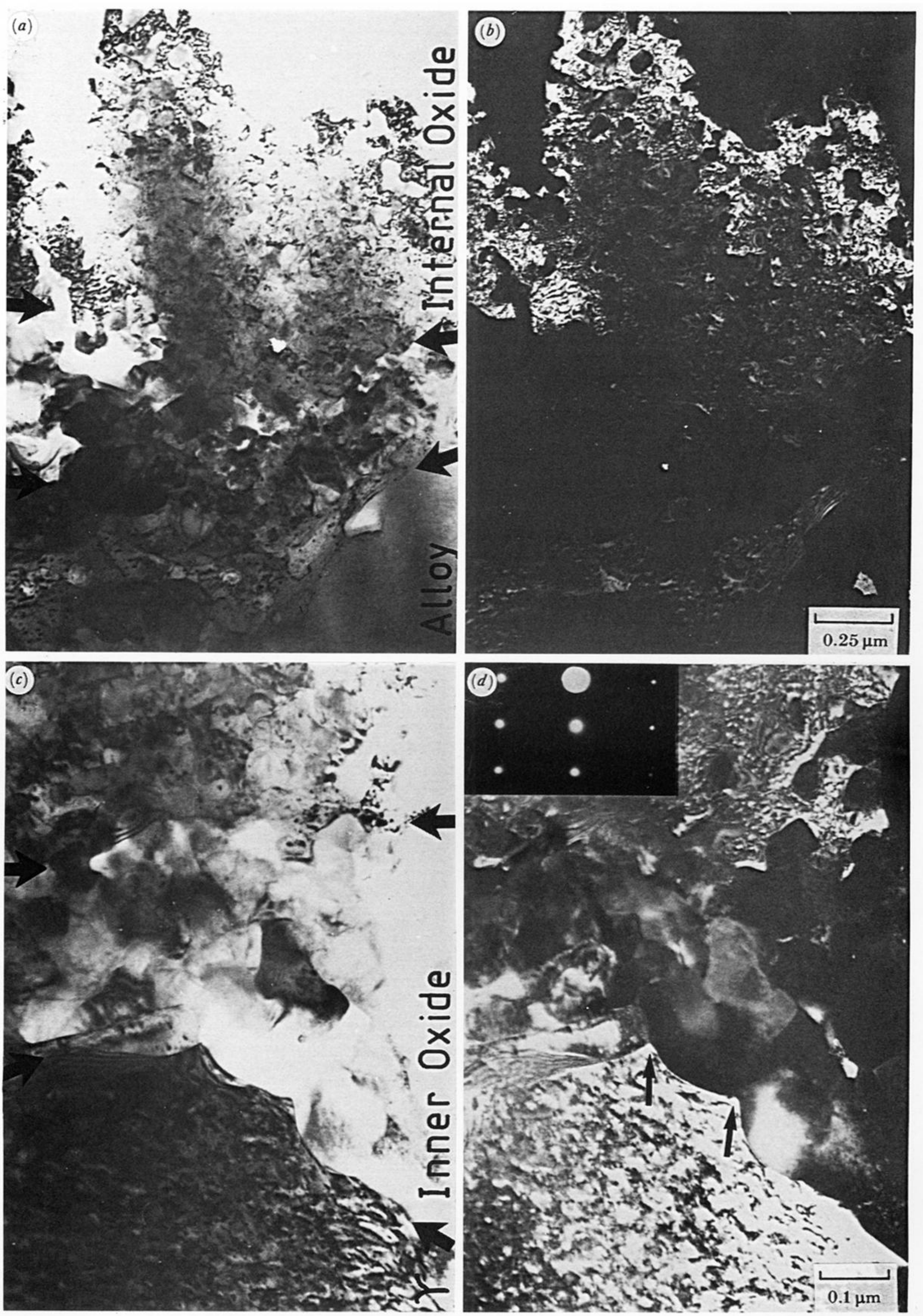

FIGURE 16. Fe–10Cr–34Ni oxidized for 1000 h in air at 600 °C showing the 'non-protective' scale in the region of the metal–oxide interface. (*a*) A band (*ca.* 250 nm) of RI oxide is sandwiched between the alloy and OI oxide above it, as delineated by the arrows. Bright-field and (*b*) dark-field (imaged with a spinel reflection), which shows the oxide in the region of the OI scale (cf. figure 11*c*). (*c*) RI oxide at the metal–oxide interface showing the cusped morphology of the scale growth. Bright-field and (*d*) dark-field (imaged with an austenite reflection) showing that the austenite in the OI oxide above the 'inner' spinel has an identical orientation as in the alloy.

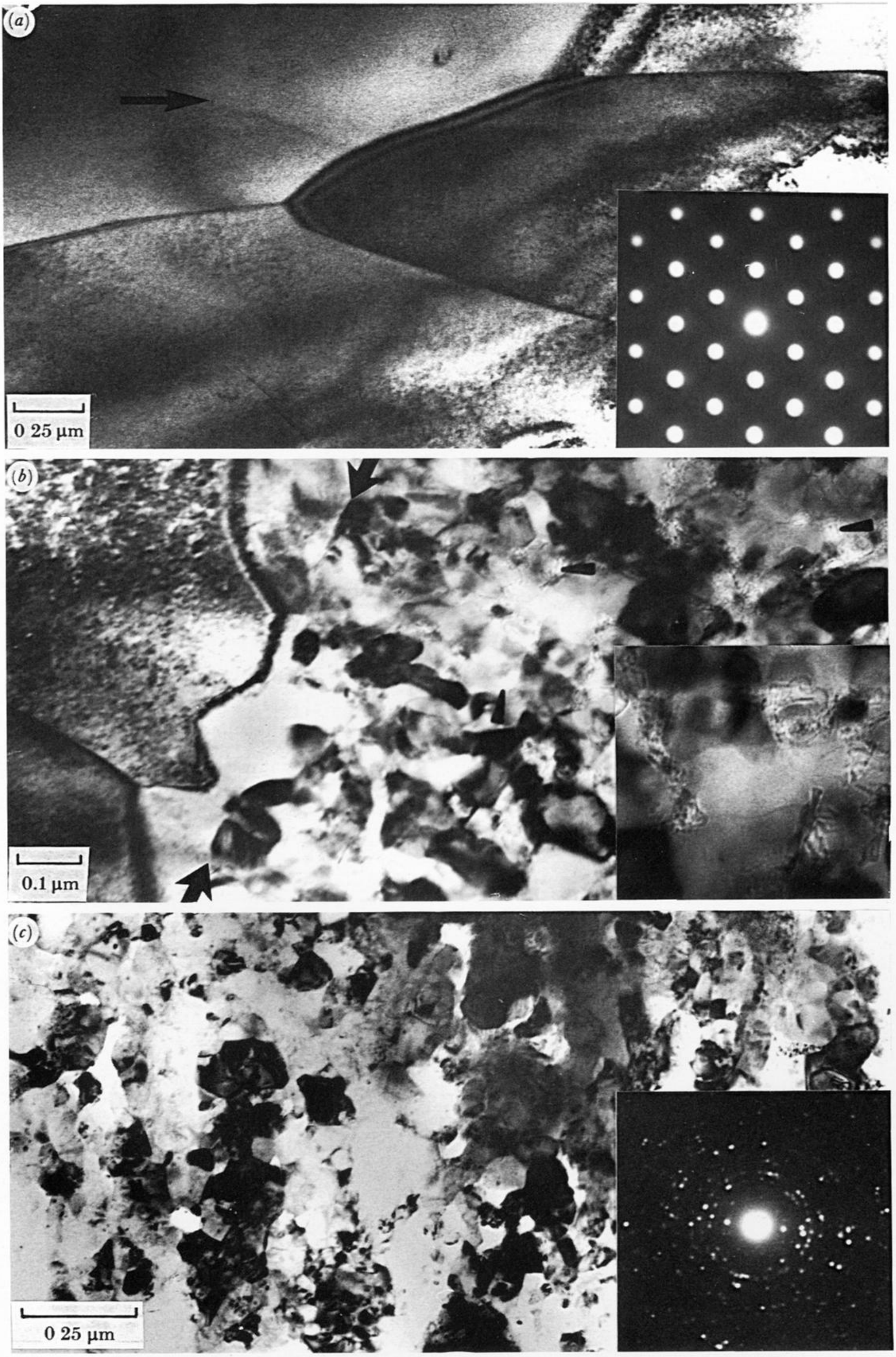

FIGURE 17. Fe–9Cr–1Mo oxidized in 1% CO–CO_2 for 1000 h at 600 °C. 'Edge-on' TEM. (*a*) Columnar grained magnetite. The arrow is normal to and approximately 3 μm from the duplex oxide interface. The inset shows a $(110)_{Fe_3O_4}$ diffraction pattern. (*b*) The duplex oxide interface where the position of the original metal surface is arrowed. Pores in the underlying fine grained oxide are also marked and are shown enlarged in the inset. The contrast of the pores has been Fresnel enhanced. (*c*) A typical region of fine grained inner oxide approximately 20 μm from the duplex oxide interface, which is untextured as shown by the inset diffraction pattern.

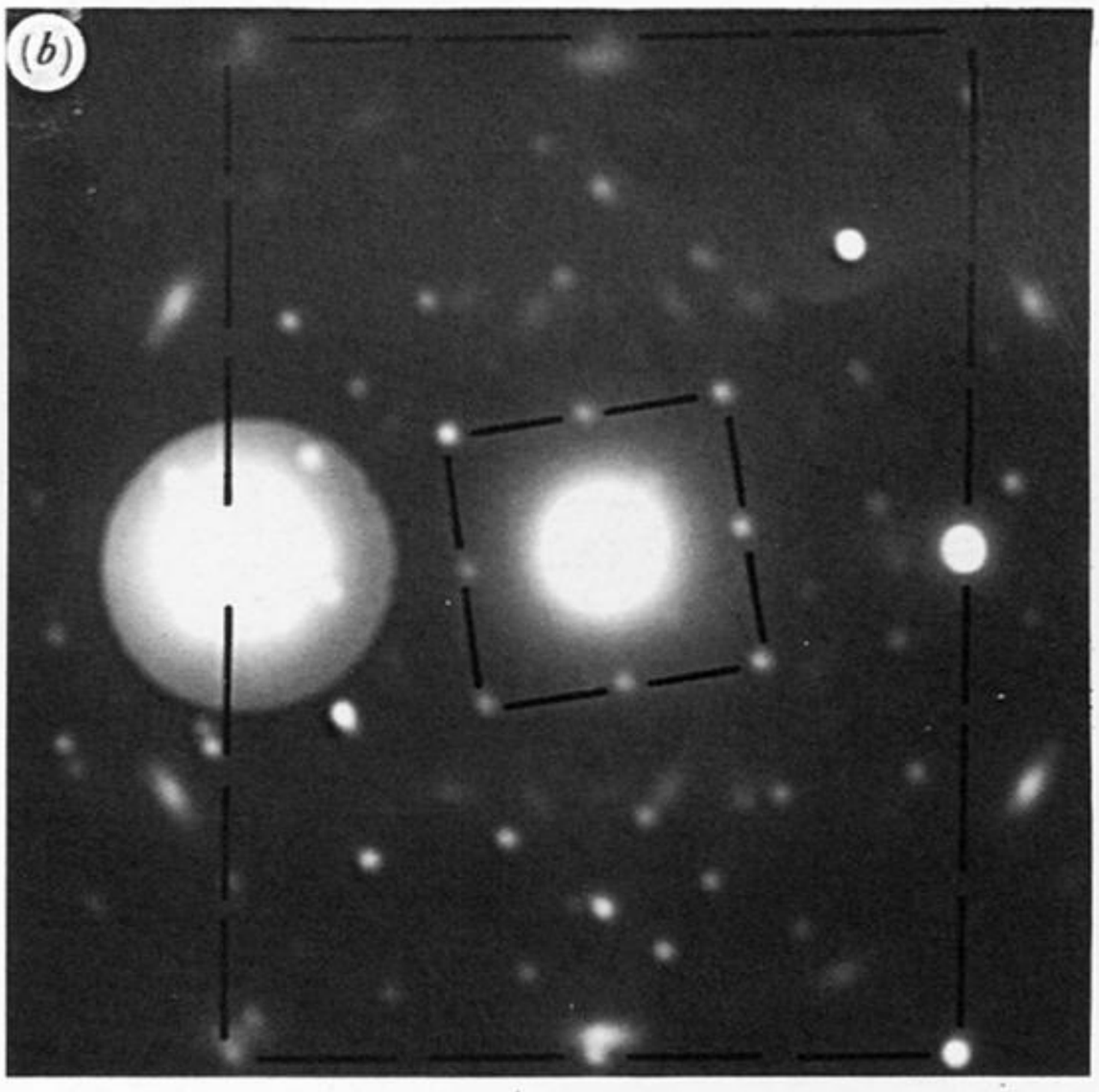

FIGURE 18. Fe–9Cr–1Mo oxidized in 1% CO–CO_2 for 1000 h at 600 °C showing the morphology and structure of the ferrite beneath the scale. (*a*) Bright-field micrograph showing carbide precipitates in the ferrite in the region of the alloy–oxide interface (arrowed). (*b*) $(011)_\gamma//(001)_{M_{23}C_6}$ diffraction pattern, the orientation relationship being as marked.

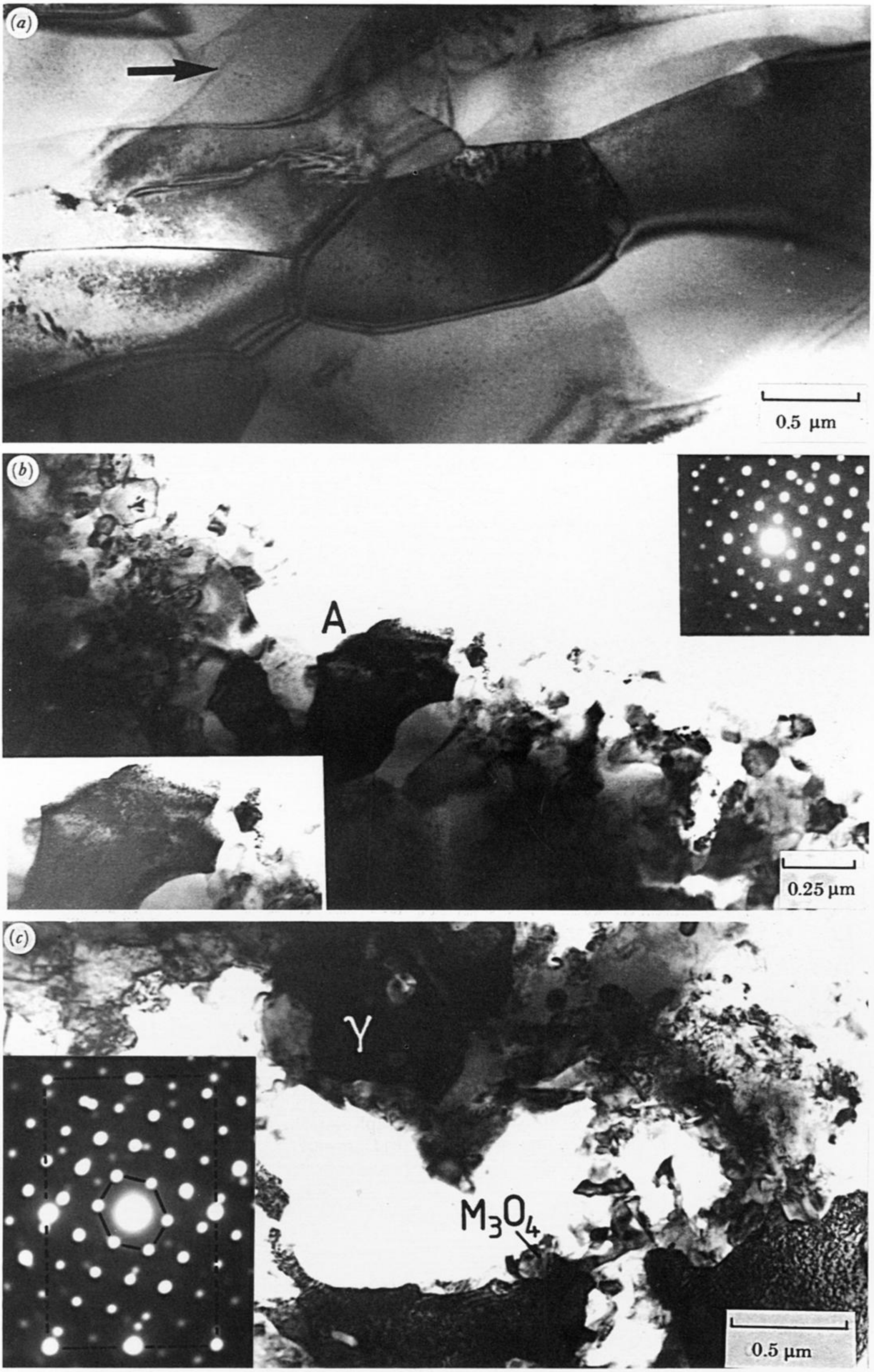

FIGURE 19. Fe–10Cr–10Ni oxidized in 1 % CO–CO_2 for 125 h at 600 °C showing: (*a*) columnar magnetite grains; the arrow is normal to and approximately 5 μm from the duplex oxide interface; (*b*) fine grained inner spinel oxide approximately 5 μm beneath the duplex oxide interface; a large spinel grain (see inset $(110)_{M_3O_4}$ diffraction pattern) may be observed at A and is shown enlarged in the inset micrograph; (*c*) a region of austenite and M_3O_4; here the two phases are orientated $(112)_\gamma // (011)_{M_3O_4}$ as shown in the inset diffraction pattern.

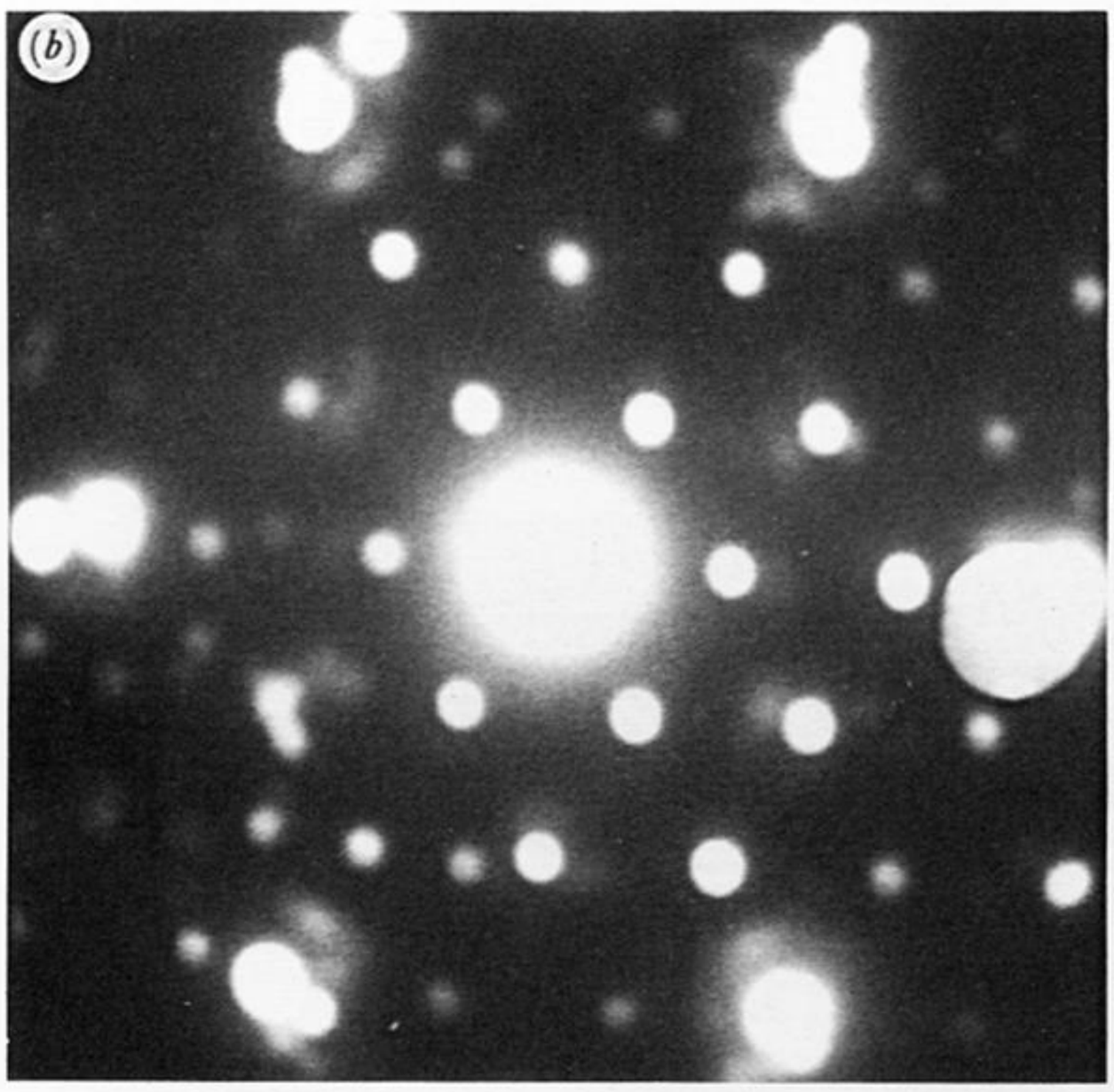

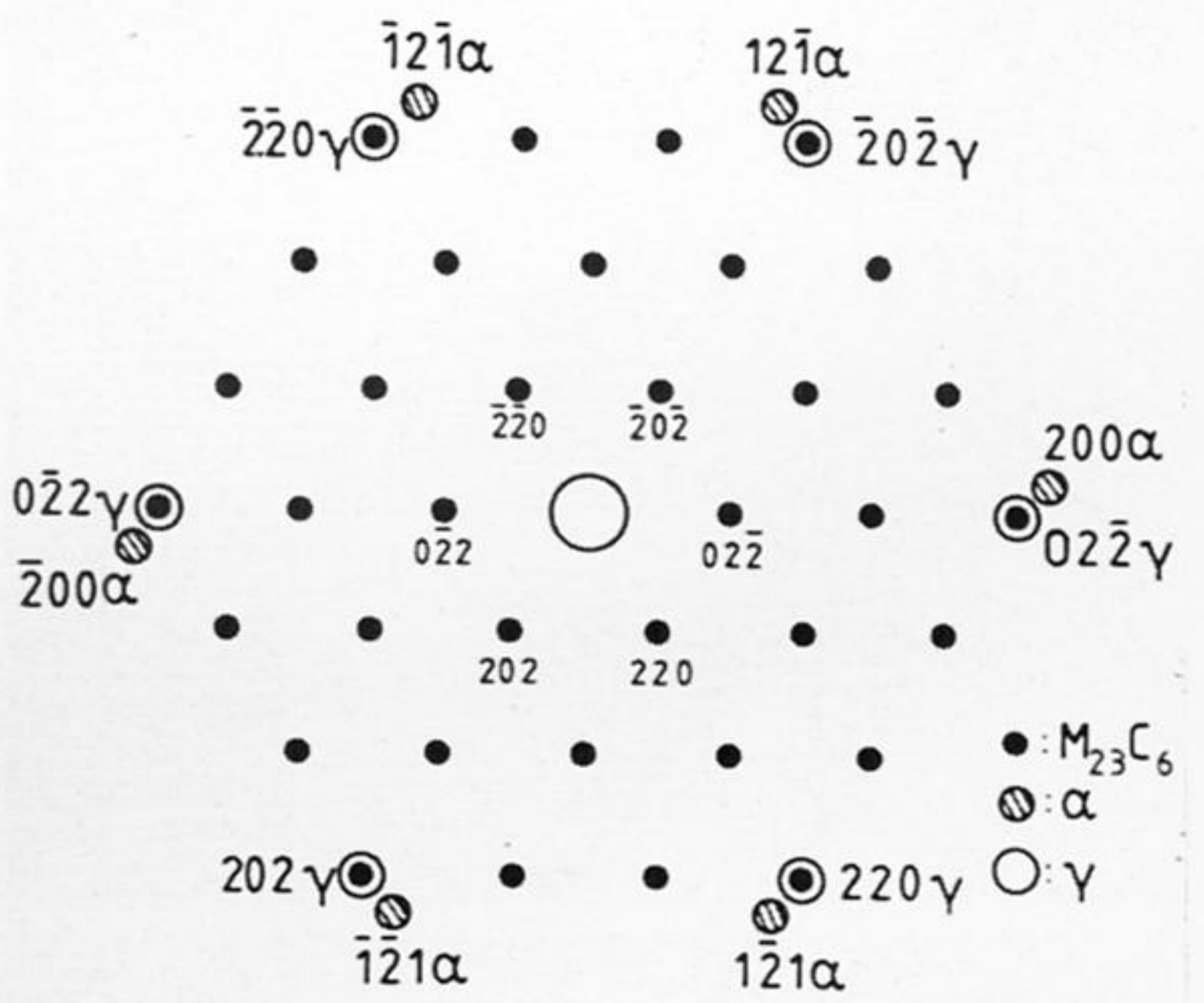

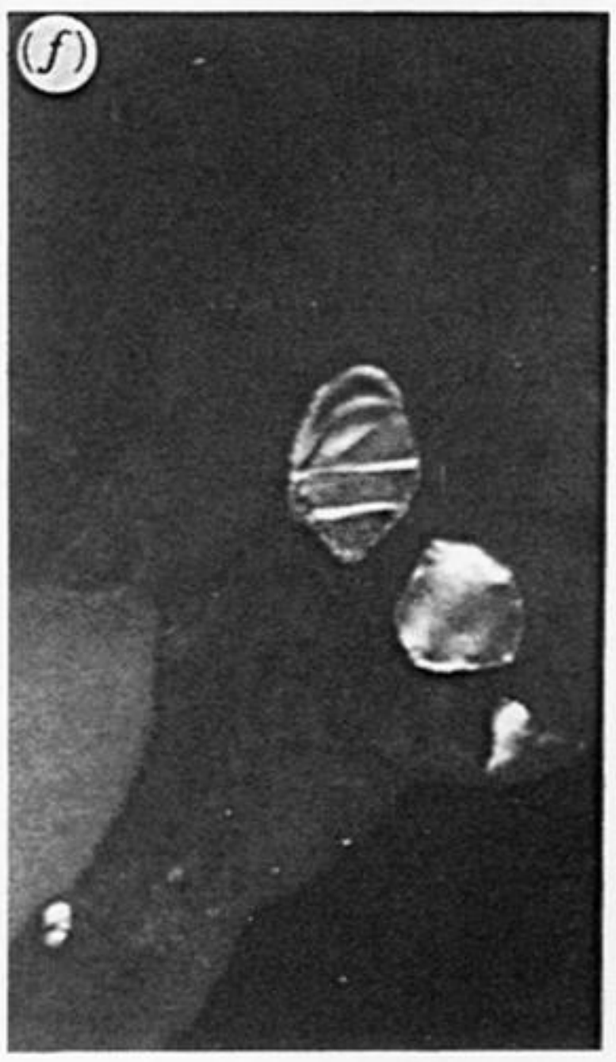

FIGURE 20. Fe–10Cr–10Ni oxidized in 1 % $CO–CO_2$ for 125 h at 600 °C. 'Edge-on' TEM showing the microstructure of the OI oxide approximately 100 μm beneath the duplex oxide interface. (*a*) Bright-field micrograph showing ferrite, austenite and $M_{23}C_6$ carbides, as marked; (*b*) $(012)_\alpha//(111)_\gamma//(111)_{M_{23}C_6}$ diffraction pattern; (*c*) Bright-field and (*d*) dark-field (imaged with a (200) ferrite reflection); (*e*) dark-field (imaged with a (220) austenite reflection); (*f*) dark-field (imaged with a (220) carbide reflection).

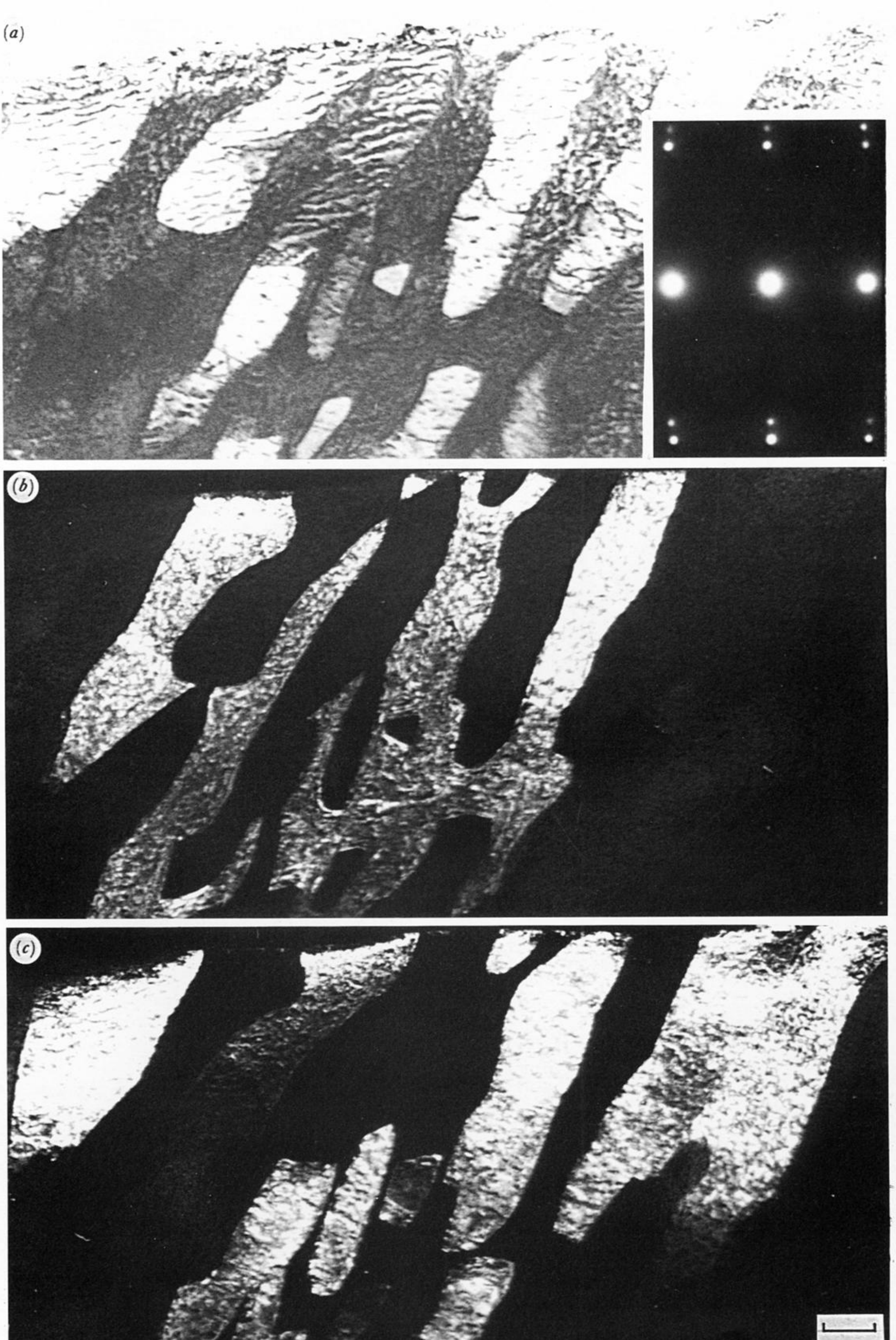

FIGURE 21. Microstructure of the Fe–10Cr–10Ni alloy after oxidation in 1 % CO–CO_2 for 125 h at 600 °C showing: (*a*) the duplex alloy microstructure; the inset shows a $(011)_\alpha // (112)_\gamma$ diffraction pattern; (*b*) dark-field (ferrite); (*c*) dark-field (austenite).

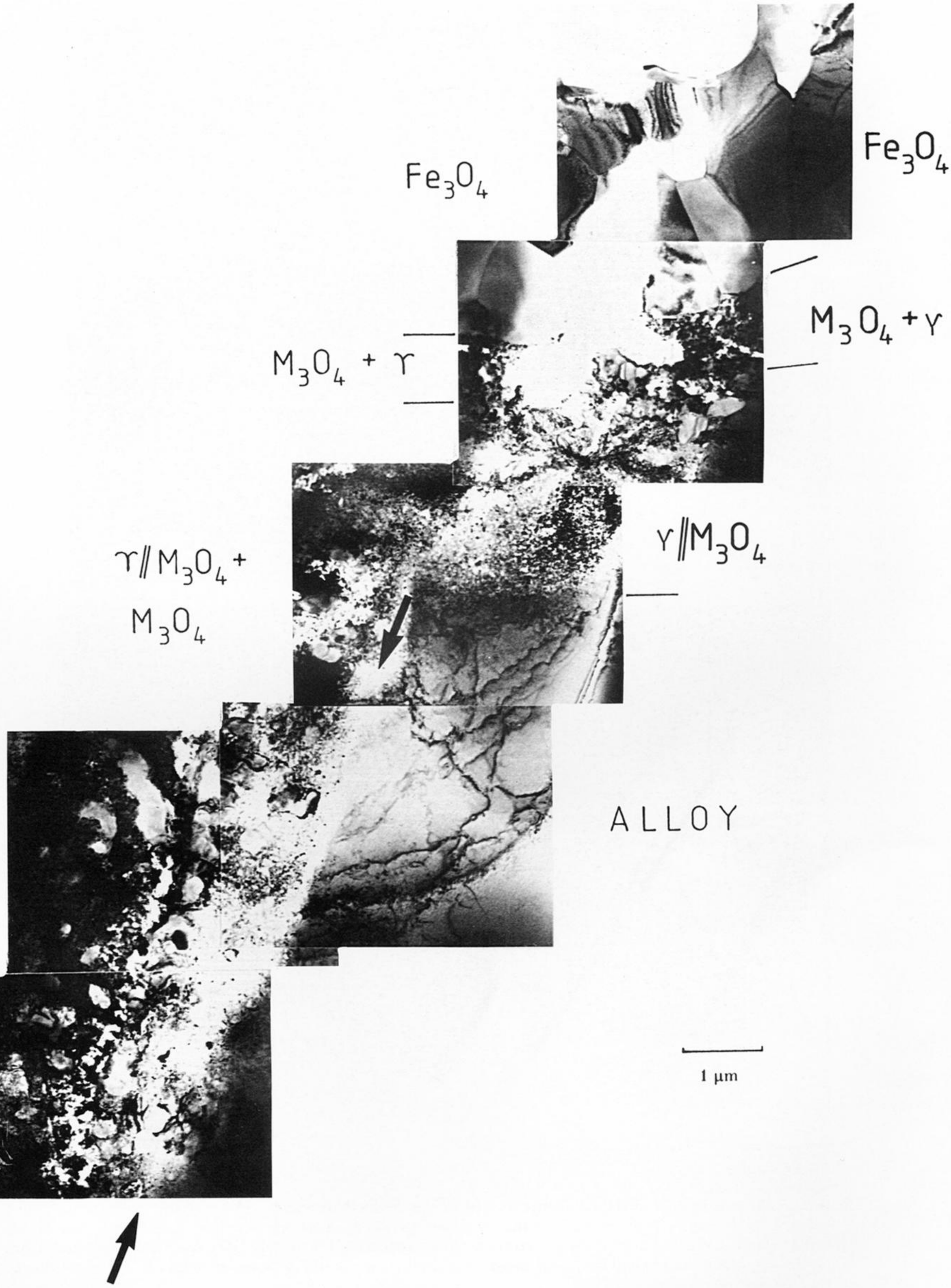

FIGURE 22. Bright-field TEM montage of the duplex scale formed on Fe–10Cr–20Ni in 1 % CO_2 after 125 h at 600 °C showing a region of preferential oxide growth at an alloy grain boundary (arrowed). The discreet layer of RI scale at the duplex oxide interface below which there is OI oxide should be noted.

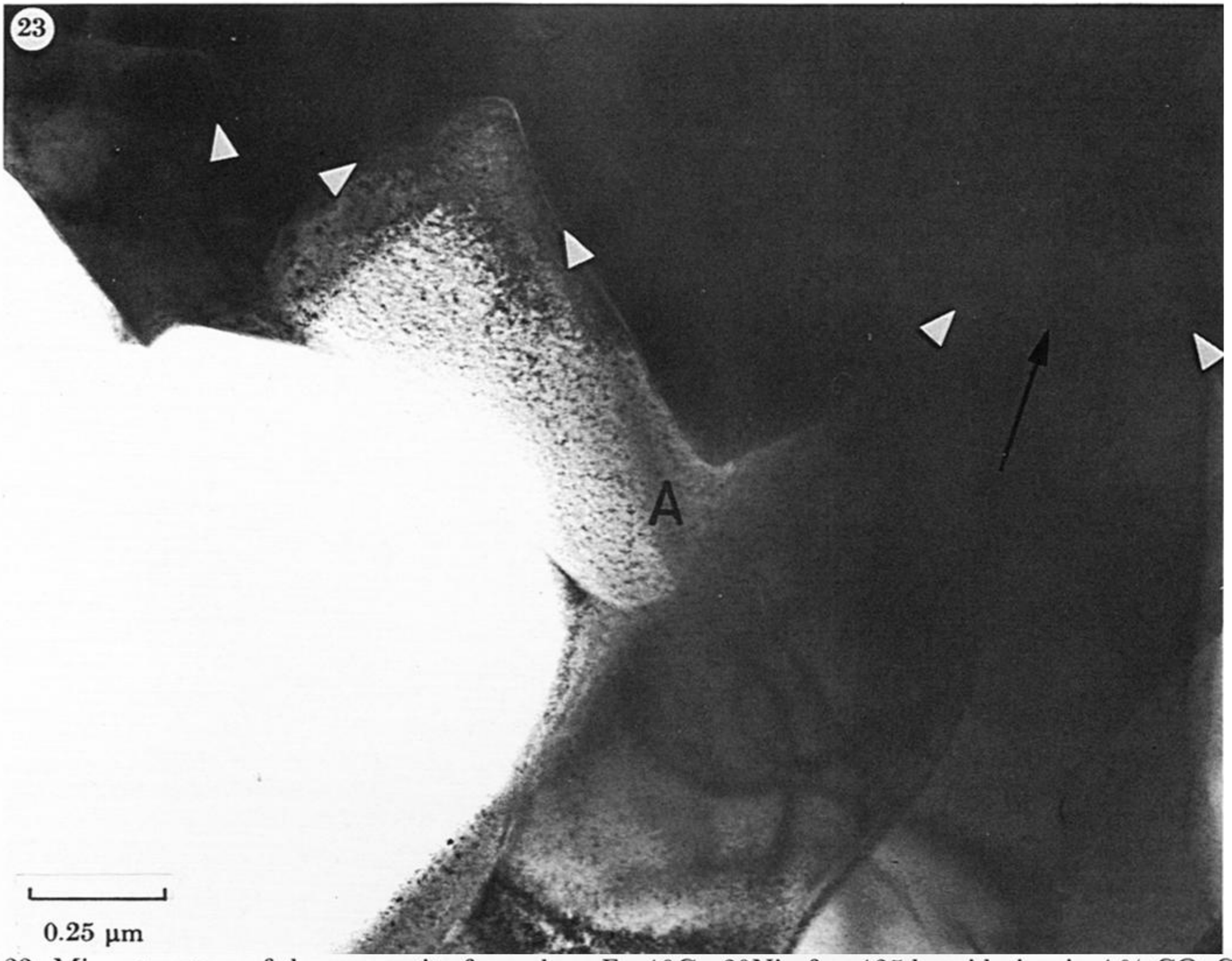

FIGURE 23. Microstructure of the magnetite formed on Fe–10Cr–20Ni after 125 h oxidation in 1 % CO–CO_2 at 600 °C. The image shows the scale at the oxide–gas interface, where the magnetite–nickel plate interface is marked. (The plate is used in the preparation of the 'edge-on' foils.) Grain boundaries in the magnetite are arrowed, which are regions where enhanced oxide growth has occurred, leaving cavities in the surface of the scale, as at A.

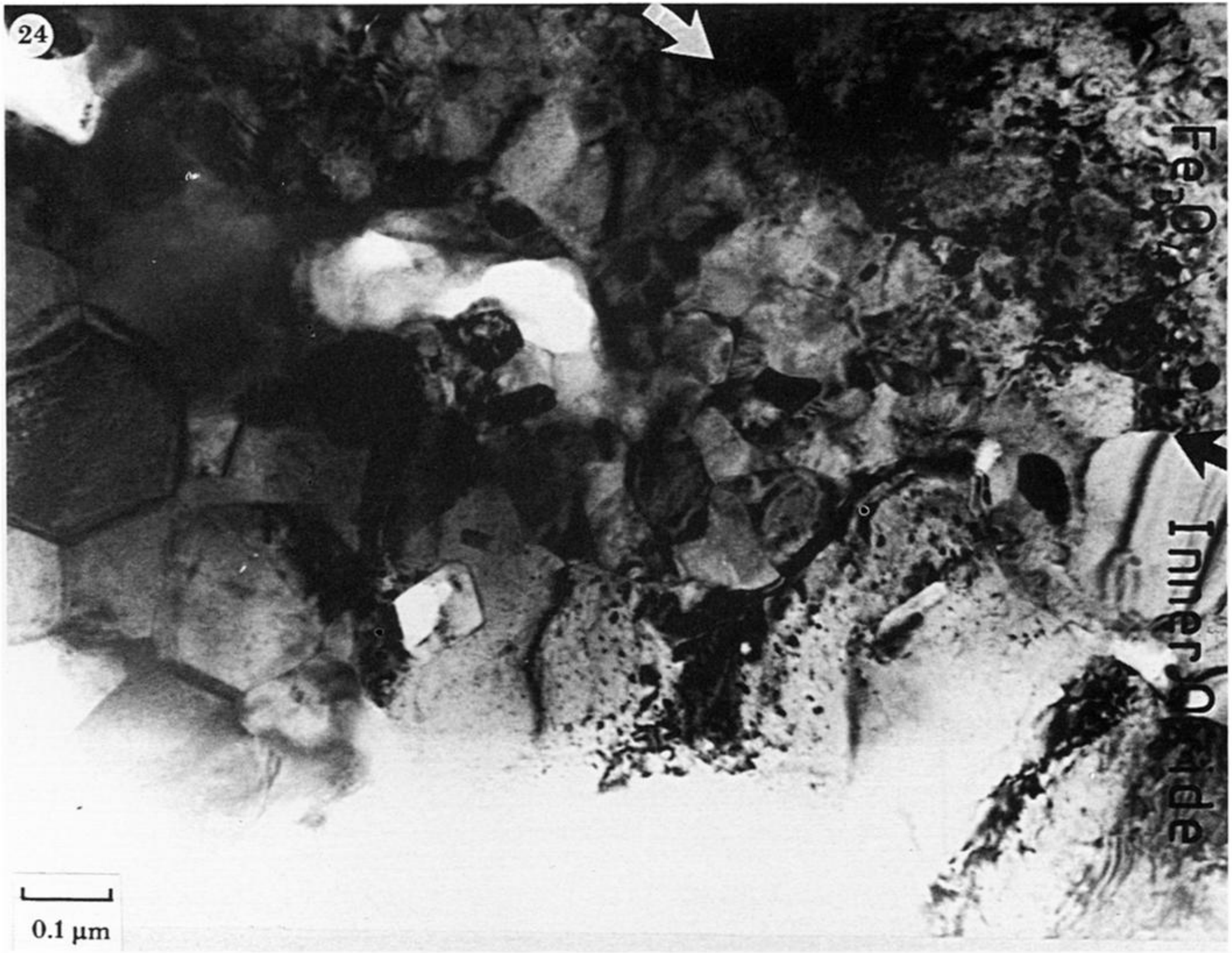

FIGURE 24. The duplex oxide interface in the scale formed on Fe–10Cr–20Ni after 125 h in 1 % $CO–CO_2$ at 600 °C. The interface is arrowed. Note the fine grained morphology of the RI oxide which exhibited an iron and chromium concentration gradient.

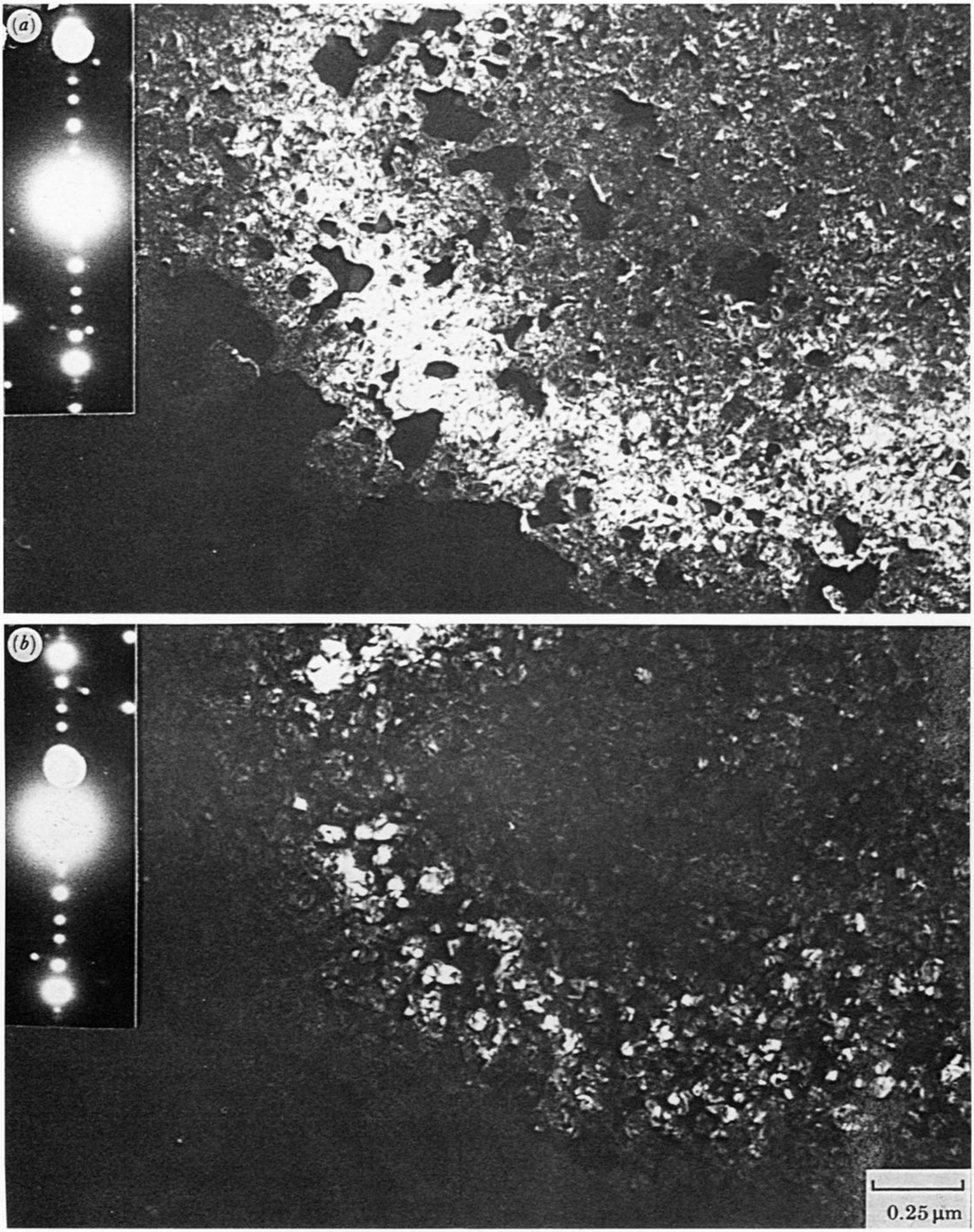

FIGURE 25. Microstructure of the inner scale formed at a grain boundary in Fe–10Cr–20Ni after 125 h in 1 % CO–CO_2 at 600 °C: (*a*) Dark-field micrograph, imaged with an (020) austenite reflection; (*b*) dark-field micrograph, imaged with an (020) spinel reflection. There are no indications that this RI oxide is porous.

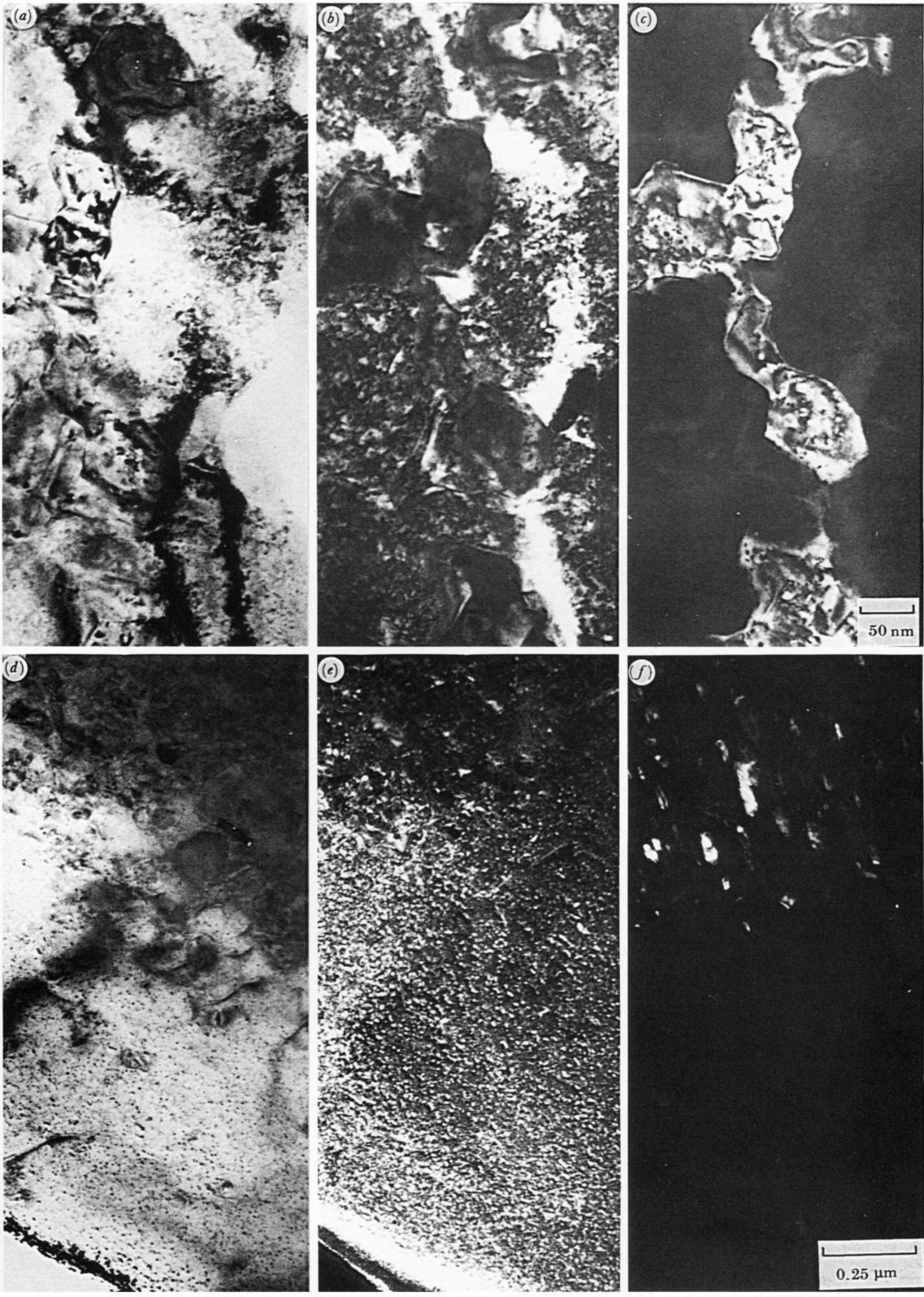

FIGURE 26. Fe–10Cr–20Ni oxidized in 1 % CO–CO_2 for 1000 h at 600 °C: (*a*) showing regions of cube–cube orientated austenite and spinel approximately 20 μm beneath the Fe_3O_4–M_3O_4 interface; (*b*) dark-field (austenite); (*c*) dark-field (spinel); (*d*) showing the diffuse metal–oxide interface approximately 50 μm beneath the Fe_3O_4–M_3O_4 interface; (*e*) dark-field (austenite); (*f*) dark-field (spinel).

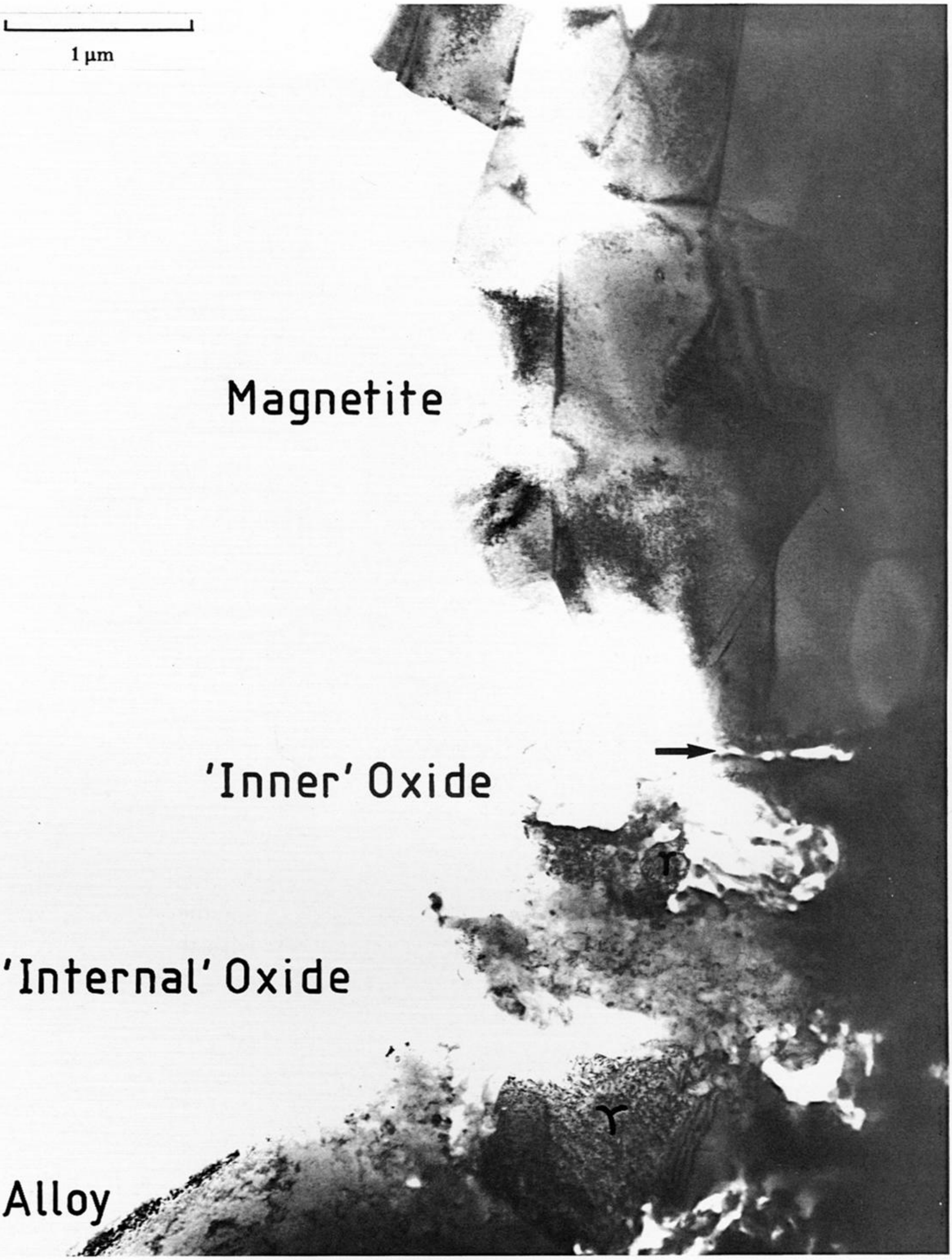

FIGURE 27. 'Edge-on' bright-field micrograph of the duplex scale formed on Fe–10Cr–34Ni in 1 % CO–CO_2 after 125 h at 600 °C. The microstructure of the inner oxide layer is complex and contains austenite. Note the partial spallation at the duplex oxide interface (arrowed) and that the OI oxide contains some large holes formed by 'etching' during ion beam thinning.